**Characterization of Proton Exchange Membrane Materials for Fuel Cells by Solid State Nuclear Magnetic Resonance**

by

**Xueqian Kong**

A dissertation submitted to the graduate faculty

in partial fulfillment of the requirements for the degree of

DOCTOR OF PHILOSOPHY

Major:  Chemistry

Program of Study Committee:
Klaus Schmidt-Rohr, Major Professor
Mei Hong
John G. Verkade
Marek Pruski
Steve W. Martin

Iowa State University

Ames, Iowa

2010

# Table of Contents

## Acknowledgements

First of all, I owe my greatest gratefulness to my parents Lili Chen and Qingjian Kong for their unconditional support, love and understanding. Though being apart for years, they kept encouraging and caring of me through emails and phones. Nothing I earned is without their help.

Second, I would like to thank my Ph.D. advisor Professor Klaus Schmidt-Rohr, who has been guiding my research work during these years. From him, I have learned not only the knowledge of physics and chemistry, but also the most stringent attitude and critical thinking towards scientific research. I am also grateful for his understanding of my flexible working time.

I deeply appreciate the help and advice offered by my POS committee members: Professor Mei Hong, Professor John Verkade, Professor Marek Pruski, and Professor Steve Martin. They not only have assisted me with my research projects, but also provided generous support during my job hunting.

I also acknowledge the current and former group members in Klaus and Mei's groups, in particular Dr. Eugene Levin, Yanyan Hu, Adu Rawal, Xiaowen Fang, Yongchao Su, Yuan Zhang, Dr. Sarah Cady, Dr. Wenbin Luo, and Dr. Shenhui Li, for their countless help and inspiring ideas. Here I would like to thank Dr. Jingdong Mao as well for our collaboration that benefits my vision of scientific research.

I am very grateful to my formal advisors Dr. Guoxing Lin and Dr. Alan Jones in Clark University. It was them who led me into the field of magnetic resonance and sparked my interest.

Thanks to all my friends and relatives in United States and in China for all the joys that they have brought to me.

In the end, I want to give special thanks to my girlfriend Yan Yan, who has accompanied, delighted, and motivated my life. Even since I met her, my Ph.D. life has been fulfilled with beautiful and unforgettable stories.

## Abstract

Solid-state nuclear magnetic resonance (NMR) has been used to explore the nanometer-scale structure of Nafion, the widely used fuel cell membrane, and its composites. We have shown that solid-state NMR can characterize chemical structure and composition, domain size and morphology, internuclear distances, molecular dynamics, etc. The newly-developed water channel model of Nafion has been confirmed, and important characteristic length-scales established. Nafion-based organic and inorganic composites with special properties have also been characterized and their structures elucidated.

The morphology of Nafion varies with hydration level, and is reflected in the changes in surface-to-volume (S/V) ratio of the polymer obtained by small-angle X-ray scattering (SAXS). The S/V ratios of different Nafion models have been evaluated numerically. It has been found that only the water channel model gives the measured S/V ratios in the normal hydration range of a working fuel cell, while dispersed water molecules and polymer ribbons account for the structures at low and high hydration levels, respectively.

Although the cross-section morphology of Nafion has been derived from SAXS data, the structure in the third dimension, which is channel straightness, was not clear. With $^2$H NMR, $D_2O$ can be used as a probe to study channel straightness (persistence length). In drawn Nafion with straight channels, the exchange between bound and free $D_2O$ results in a residual quadrupolar splitting of 1-2 kHz; while in normal Nafion with coiled channels, the $^2$H quadrupolar splitting of $D_2O$ is ~ 10-fold smaller. It is explained by the motional averaging of the $^2$H coupling frequencies in the NMR timescale when $D_2O$ diffuses through differently-oriented segments. The simulations of line narrowing and $T_2$ relaxation times of $D_2O$ revealed a persistence length within 30 to 80 nm for normal Nafion.

The Nafion phosphatranium composite developed by Verkade and Wadhwa, which is a potential candidate for anion exchange membranes, has been characterized by solid-state NMR. The synthesized membrane has two major components, in which phosphatranium

cations are bonded to Nafion side-groups via either P or N with a mole ratio of 2:1. Degradation of the phosphatranium cations has not been found in the composite membrane, which implies a good stability of the material.

Nafion-silica (NafSil) and Nafion-zirconium phosphate (NafZrP) composites prepared by the in-situ growth of inorganic particles in the channels of Nafion membrane have been characterized. Under typical situations with an inorganic volume fraction of around 15%, elongated nanoparticles are formed inside the water channels. The inorganic particles have cylindrical shapes with a cross-section area of ~ 6 $nm^2$ and surrounded by water layers with a thickness of ~ 0.8 nm.

Zirconium phosphates (ZrP) synthesized in and outside Nafion have been characterized in detail by solid-state NMR and X-ray diffraction (XRD). It has been found that typical $\alpha$-ZrP with water of crystallization transforms to anhydrous $\alpha$-ZrP and condensed pyrophosphates after drying at $150^o$C. When grown in Nafion, ZrP favors a structure with two disordered layers and a majority of $(HO)P(OZr)_3$ sites, different from regular $\alpha$-ZrP, particularly after drying.

# Chapter 1

# Proton Exchange Membranes for Fuel Cells

## 1.1 Introduction

The world's energy demand is rapidly increasing and will continue to grow in the future. It has brought two profound challenges to the human society around the globe: the imminent depletion of fossil fuels (e.g. petroleum and coal) and the negative environmental impacts (e.g. pollution and global warming). These issues have to be addressed in two aspects: to capture "new" energy sources (e.g. hydropower, solar power, wind power, and etc.), and to increase the efficiency of energy use (e.g. better house insulation, fuel cells, and etc.).

Fuel cells represent a fundamental breakthrough in increasing the efficiency of energy conversion from chemical fuels [1]. Unlike traditional electrical generators that burn fossil fuels, fuel cells directly convert chemical energy into electricity. The removal of intermediate processes makes fuel cells free of the Carnot limit for heat engines, and in turn results in less chemical emission [2]. Fuel cells first came out as onboard power supplies for US spaceships. After evolving for several decades, fuel cells have already made their appearance in the commercial market. Fuel-cell-powered vehicles and power stations are now available in many places [3-5]. Fuel cells are categorized by their electrolyte materials as listed in Table 1.1.

Compared to other potential energy innovations e.g. full-electric vehicles, fuel-cell-powered systems have their indispensible advantages such as the high energy density of fuels, the all-weather working capability, and the independence from the electric grid [2,6,7]. Various fuels, e.g. hydrogen or methanol, can be utilized. They can be obtained from traditional fossil fuels and natural gas, or from reformed biomass, or from stored energy of solar and wind power [1]. Along with renewable energy sources, fuel cells will contribute to resolving the energy shortage and global warming issues.

| Fuel cells | Electrolyte (working temp.) | Fuels | Applications |
|---|---|---|---|
| Proton exchange membrane fuel cell | Polymer membranes ($60 \sim 100^{\circ}$C) | Hydrogen, methanol | Automobiles, portable devices |
| Solid oxide fuel cell | Ion conducting ceramics ($600 \sim 1000^{\circ}$C) | Reformed gasoline, bio-fuels | Stationary power supplies |
| Phosphoric acid fuel cell | Liquid $H_3PO_4$ ($175 \sim 200\ ^{\circ}$C) | Hydrogen | Stationary power supplies |
| Alkaline fuel cell | Aqueous KOH ($< 100^{\circ}$C) | Hydrogen | Spaceships |
| Molten carbonate fuel cell | Metal carbonates ($600 \sim 1000\ ^{\circ}$C) | Natural gas, coal | Power plants |

**Table 1.1.** List of different types of fuel cells [2,8].


## 1.2 Principles of proton exchange membrane fuel cells

Proton exchange membrane (PEM) fuel cells have demonstrated the most promising applications in automobiles and portable devices compared to other types of fuel cells. Theoretically, PEM fuel cells can reach at least twice the efficiency of internal combustion engines and possibly with much less emission [9]. And the high energy density of fuels makes them more appealing than the conventional batteries [4]. Practically, PEM fuel cells are suitable for the auto industry due to the flexible manufacture with polymer membrane and its moderate working temperature, normally below or around 100 $^{\circ}$C [10,11].
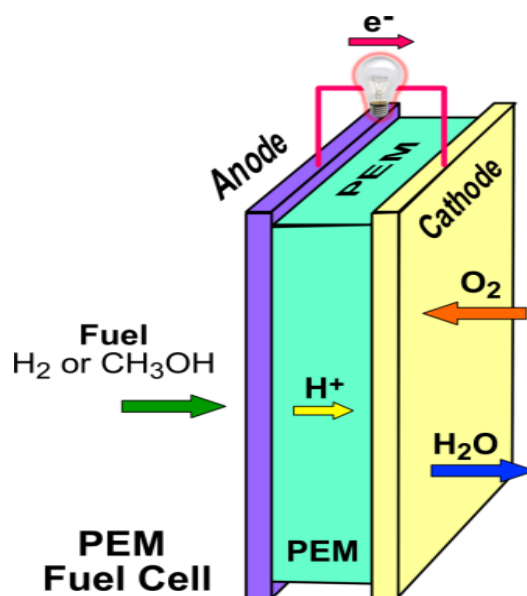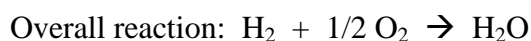
**Figure 1.1.** The configuration of a proton exchange membrane fuel cell.

The above diagram (Figure 1.1) shows the basic configuration of a proton exchange membrane (PEM) fuel cell. As we can see, the core of the fuel cell consists of an anode, a cathode, and a polymer electrolyte. During the operation, the fuels (i.e. hydrogen or methanol) are supplied at the anode while the oxidant (i.e. oxygen or air) is supplied at the cathode. Hydrogen atoms at the anode are then split into protons and electrons with the help of a catalyst (usually platinum). The electrons pass though the outer circuit and power the electric load; while protons pass through the electrolyte and react with oxygen at the cathode also with the help of a catalyst. The chemical equations of the electrolyte reactions are shown below for a PEM fuel cell [2].

When hydrogen gas is used as a fuel:

Anode: $H_2 \rightarrow 2\,H^+ + 2\,e^-$

Cathode: $1/2\,O_2 + 2\,H^+ + 2\,e^- \rightarrow H_2O$

Overall reaction: $H_2 + 1/2\,O_2 \rightarrow H_2O$
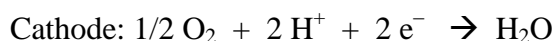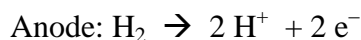
When methanol is used as a fuel (direct methanol fuel cells):

Anode: $CH_3OH + H_2O \rightarrow CO_2 + 6\,H^+ + 6\,e^-$

Cathode: $3/2\,O_2 + 6\,H^+ + 6\,e^- \rightarrow 3\,H_2O$

Overall reaction:  $CH_3OH + 3/2\ O_2 \rightarrow CO_2 + 2\ H_2O$
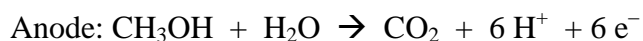
Despite the variety of fuel cell technologies, their underlying configurations are much alike. In alkaline fuel cells and solid oxide fuel cells, hydroxide and oxygen anions rather than protons act as the conducting ions respectively [2]. The key requirement of a fuel cell is that pathways of ions and electrons have to be separated so that electric current can be generated.

## 1.3 Technical challenges of PEM fuel cells

Though the PEM fuel cell is a very promising technology, it faces a number of technical challenges, among which the hydrogen storage, water management, the cost of catalyst, and durability of the polymer membrane are probably the most crucial [6,9,12,13].

Up to date, most PEM fuel cell systems use hydrogen as the fuel. Therefore a large-scale hydrogen production and distribution infrastructure has to be built to accommodate the need of hydrogen. There are difficult engineering issues concerning the hydrogen storage in the production lines or for onboard usage. Hydrogen stored in pure form, either liquefied or pressurized, is usually unfavorable due to the additional energy for liquefying gas or the low volumetric density of gas cylinders [10]. Several metal hydrides have shown promising properties that are close to the targets of the Department of Energy (see Figure 1.2). However many of the hydride materials are hampered by the slow kinetics for releasing hydrogen gas [14,15].
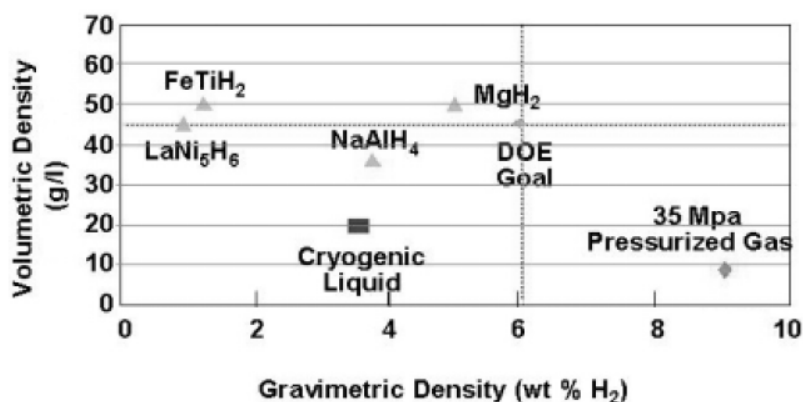
**Figure 1.2.** System energy densities for different hydrogen storage methods [10].

Water management involves the control of water and gas flow in the fuel cell systems, in particular the gas diffusion layers (GDL) which are attached to the electrodes (Figure 1.3). Multiple channels are carved into the GDL to ensure sufficient distribution of fuel and oxygen (or air) to the reaction centers on the electrodes, and to facilitate the flow of product water. The water accumulated at the cathode has to be removed quickly; otherwise it will block the path of oxygen, which is called "flooding" [16]. On the other hand, humidified inlet gases are usually required for the polymer electrolyte which needs a considerable amount of water to function properly [17,18]. As a result, the installations of additional humidifier and flow control components complicate the design of fuel cells. The self-humidifying and humidifier-free systems are still under development [4,19].
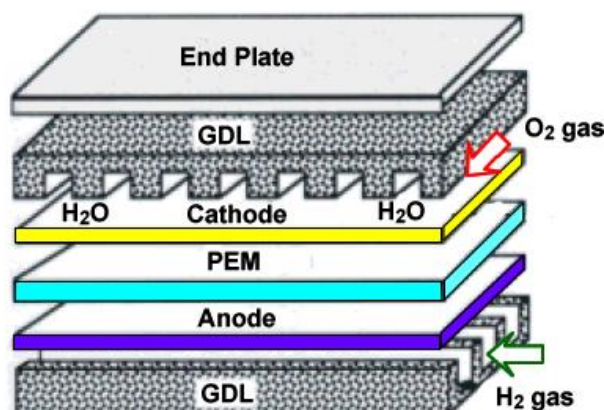
**Figure 1.3.** Illustration of the gas diffusion layers in a PEM fuel cell.

To be commercially competitive, the cost of fuel cell vehicles should be comparable to traditional vehicles. However, the estimated cost of a 100 kW fuel cell propulsion system is around 30,000 US dollars [20], which is far more expensive than the internal combustion engines or even battery-powered engines. The main cost issue arises from the large amount of Pt used for catalytic reactions in PEM fuel cells [12]. It is difficult to substantially reduce the loading of Pt. In addition, the performance of Pt suffers from contaminants in the hydrogen fuels such as CO, $H_2S$, and $NH_3$. Currently, most of the hydrogen gas is produced from reformed natural gas. These contaminant gases are present in the product hydrogen if no extensive cleanup technologies are applied. Even a small amount of contaminants could be detrimental to the catalyst layer [21]. Other issues such as corrosion of the catalyst carbon support and sintering of Pt particles also affect the durability of the catalyst layers [18,22].

The proton exchange membrane (PEM) is the heart of a fuel cell. It requires a high conductivity and selectivity for proton transport and good chemical and thermal stability to endure the harsh acidic environment and repeated thermal cycles. The most widely used PEM is Nafion, a perfluorinated sulfonic acid (PFSA) ionomer manufactured by DuPont. Though it exhibits a better stability than many hydrocarbon materials, Nafion shows gradual degradation over a period of operation [6,17,23].

In Nafion and in most of the potential PEM membranes, sufficient water content is necessary to maintain proton conductivity [24-27]. The requirement of water brings difficulties in the water management as well as temperature limitations. The normal working temperature of PEM fuel cells is usually maintained at 80 to 90 $^{\circ}$C. At higher temperatures, the PEM will dehydrate and lose proton conductivity, and may result in irreversible mechanical damage [28]. However, higher working temperatures are favorable for the kinetics of Pt catalyst and may improve its tolerance to contaminants. The efforts to increase membrane working temperature are currently conducted on the laboratory scale, one of which is to incorporate nanoparticles as described in the section 1.6 [29-31]. Low temperature startup of a fuel cell vehicle may also be a non-negligible problem. Though water does not freeze inside the membrane [32], the GDL and other parts may be affected by water freezing.

## 1.4 Transport mechanisms of protons in PEMs

In order to design a PEM with high conductivity and selectivity, the understanding of proton transport mechanisms is a prerequisite. The transport mechanisms of proton are rather complex and they could be affected by various factors in the heterogeneous environment of a PEM [33].

In bulk water, proton may transport via two different mechanisms: the "vehicle mechanism" and "structure diffusion" [34]. For the vehicle mechanism, classical hydronium ions ($H_3O^+$) are the carriers of protons, and both water and protons diffuse at a similar rate. For the structure diffusion, protons migrate via a highly concerted process involving breaking and forming of hydrogen bonds and proton translocation within the "Zundel" and "Eigen" ions [33]. A Zundel ion ($H_5O_2^+$) is a complex that has two water molecules centered at a proton; while an Eigen ion ($H_9O_4^+$) has three water molecules in coordination with a center hydronium ion (Figure 1.4). Structure diffusion explains the exceptionally higher diffusion rate of protons compared to other small cations such as $Li^+$ and $K^+$. These two mechanisms compete against each other under different conditions: the increase of temperature, the

decrease of pressure, and the increase of acid concentration will lead to the attenuation of structure diffusion [33,35].
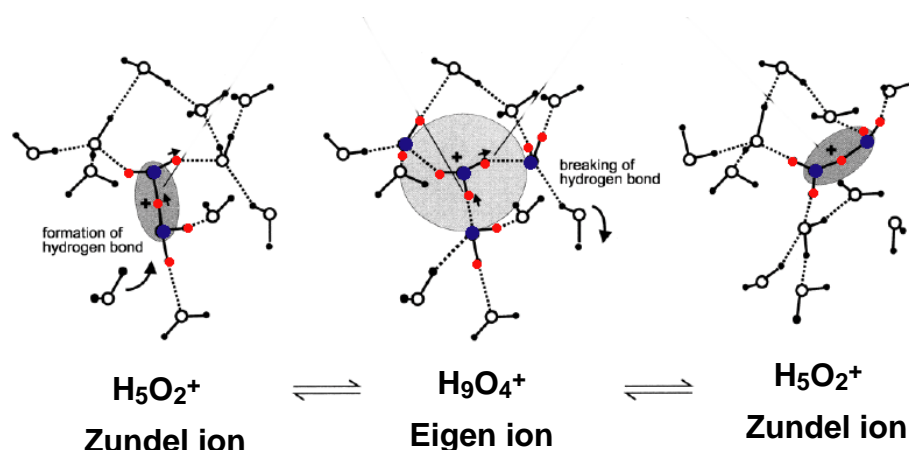


**Figure 1.4.** Proton transport by "Zundel" and "Eigen" ions.

In perfluorinated sulfonic acid (PFSA) PEMs, the proton transport and conductivity are strongly correlated to the water content [24,26,36,37]. Conventionally, the water content in PEMs is specified by the quantity $\lambda$, which indicates number of water molecules per sulfonate group. At high hydration level ($\lambda > 13$), structure diffusion dominates at the center of hydrophilic domains [38] and it results in a high diffusion coefficient of protons that approaches bulk water. At intermediate and lower hydration levels, the increased acid concentration favors the vehicle mechanism. The presence of sulfonate groups will also retard the diffusion of $H_3O^+$ ions by electrostatic interactions. A threshold is found at around $\lambda = 6$, where the dissociation energy of the sulfonate groups significantly decreases [39,40]. Moreover, the microscale structure, in particular the connectivity of hydrophilic domains, is affected by the water content. At very low water content (probably $\lambda < 2$) the hydrophilic domain will change from percolated continuous network to dispersed clusters [41] and therefore lead to very low proton conductivity. The review of the nanoscale structure of Nafion is elaborated in section 1.5.

Melting point depression of water has been observed in PFSA membranes as expected for water in confined geometries [42-46]. The presence of non-freezable water is also indicated by the continuous proton conductivity measured by NMR relaxation and diffusion measurements [47-51]. Partial freezing of water inside membrane at 0 to -20 $^{\circ}$C was initially suggested by differential scanning calorimetry [39], but later a microbean X-ray diffraction study proved that water actually freezes outside the membrane [32].

## 1.5 The structure of the PFSA ionomer membrane

The macroscopically observed proton conductivity and water permeability of a PFSA membrane are strongly correlated to its microscale structure, e.g. pore size, connectivity, and tortuosity. In order to improve the transport properties of Nafion and design novel membrane materials, it is important to understand the morphology of Nafion at the molecular and nanometer level. The structure of Nafion has been studied extensively by various techniques, e.g. X-ray and neutron scattering [41,52-55], NMR [56-58], electron microscopy [59], differential scanning calorimetry [39], and electron spin resonance spectroscopy [60]. The nanoscale structure of Nafion has a direct correlation with the scattering pattern in the small-angle X-ray scattering (SAXS). The SAXS intensity curve (Figure 1.5a) of hydrated Nafion shows a characteristic ionomer peak at $q \sim 1.1$ nm$^{-1}$. At smaller $q$ values, the intensity varies as $q^{-1}$; while at larger values, the intensity varies as $q^{-4}$.

The original and most widely referenced model is the cluster-network model proposed by Gierke et al. [61,62]. In the cluster-network model, ionic clusters with 3-5 nm in diameter and connected by 1-nm channels disperse in the fluoropolymer matrix. However, this model is inconsistent with the $q^{-1}$ dependence at small $q$ values in SAXS and inconsistent with anisotropic diffusion properties observed in $^2$H NMR [63]. Several other structure models have been proposed, such as the sandwich-like model by Haubold et al. [54] and the polymer-bundle model by Rubatat et al. [53,64]. However, few of these models can be fully fitted to the SAXS pattern reconstructed from the Fourier transform of scattering density distribution [65,66].

As a result, the water channel model was proposed for a hydration level of 11 wt% of $H_2O$ (typical condition in a working fuel cell) [66]. It is the only known model that can fit the SAXS data  (Figure 1.5a) and also explains solid state NMR results [58] in this hydration range.

In the water channel model (Figure 1.5b), randomly-packed locally-parallel hydrophilic channels surrounded by sulfonic acid side groups percolate through the membrane. The channels have an averaged diameter of 2.5 nm providing the transport pathway for protons and water. The crystallites formed in the hydrophobic fluoropolymer backbone provide the materials with mechanical strength. According to our $^2H$ NMR study and the simulation described in the Chapter 3, the persistence length of the water channel in normal Nafion is around 30 to 80 nm. The diffusion anisotropy in commercial Nafion membrane and drawn Nafion can be explained by its natural channel orientation preference and the stretching of the water channels, respectively.
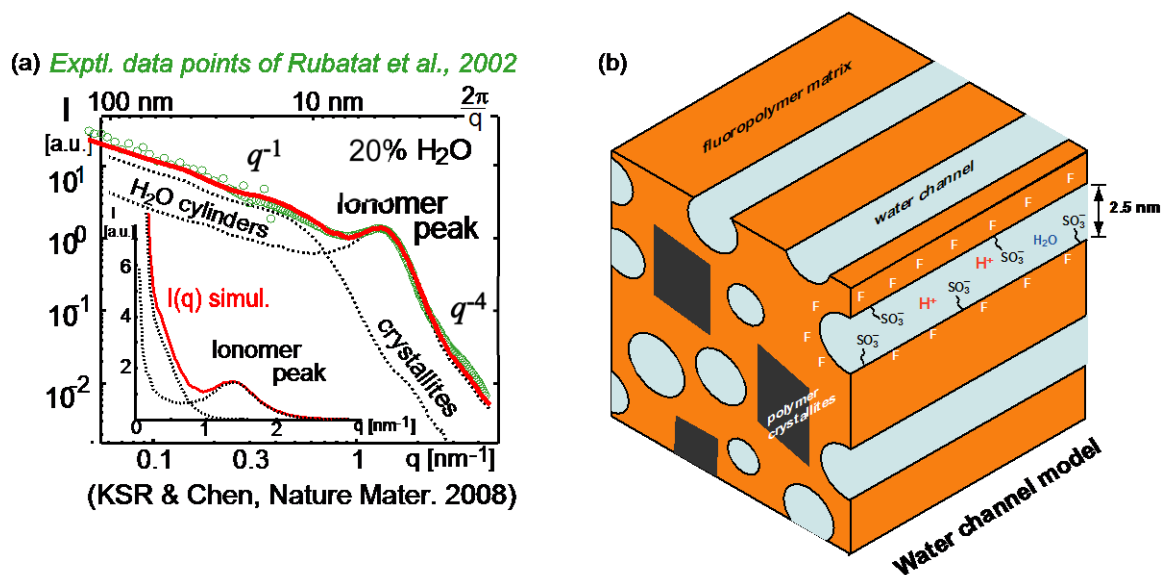


**Figure 1.5.** (a) Simulated SAXS curve of water channel model (red solid line) [66] and experimental SAXS data [64] (green circles). (b) Schematic illustration of the water channel model.

Nevertheless, the structure of Nafion could vary significantly depending on the hydration level. A simple structure model can hardly account for the whole scheme similarly. As

suggested by Gebel et al. [41], our evaluation of surface-to-volume ratios of the fluoropolymer (described in Chapter 3) shows that the morphology of Nafion evolves from a matrix with dispersed water molecules at low hydration level, to the water channel model at medium hydration level, and to polymer aggregates dispersed in water at high hydration level (Figure 1.6).
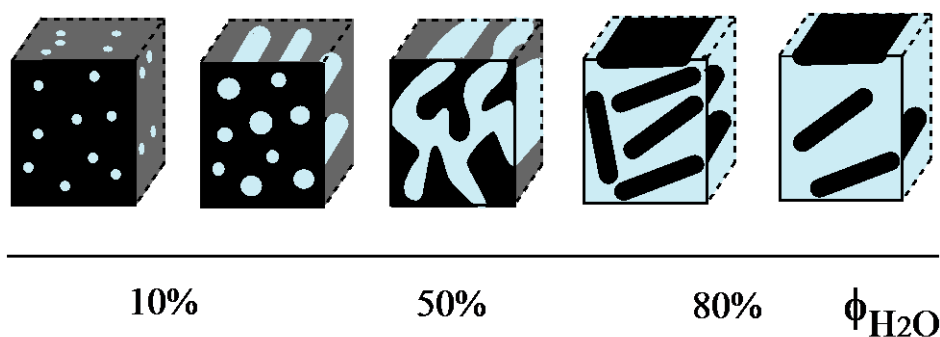


**Figure 1.6.** Morphologies of Nafion at different volume fraction of $H_2O$ ($\phi_{H2O}$).

## 1.6 Improved PEM with inorganic nanoparticles

As mentioned in section 1.3, the working temperature of normal PFSA membranes is limited at around $80 \sim 90$ $^{o}$C, which constrains the tolerance of Pt catalysts to contaminants. Furthermore, poor proton conductivity at low hydration levels complicates the design of water management systems. Materials based on e.g. sulfonated poly-arylene ethers [67], poly-sulfones [68,69], and poly-benzimidazoles [70,71] have been developed as possible alternatives, but most of them have either lower proton conductivity or insufficient stability.

Another promising approach is to modify PEMs with inorganic oxides and solid acids [30,31,72,73]. In general, the oxides, including $SiO_2$, $TiO_2$, $ZrO_2$ and $Al_2O_3$, have hygroscopic properties and are prepared with high surface areas [74,75]. Abundant hydroxyl groups on the oxide surface can strongly retain water molecules and mitigate membrane dehydration at temperatures above 100 $^{o}$C. Solid acid nanoparticles, e.g. zirconium phosphate (ZrP) [76],

silicotungstic acid (STA), and phosphotungstic acid (PTA) [77,78], provide extra proton sources in addition to their PFSA matrix. The resultant composite membranes can greatly increase proton conductivity and current density in particular at low hydration levels [31]. These oxides and solid acids can also be surface functionalized with strong acid groups [79] or mixed together [80] to increase proton conductivity. Other advantages of these PFSA/inorganic composites may include reduced swelling, enhanced tensile strength (better mechanical properties) and reduced methanol crossover for direct methanol fuel cells [30]. Working temperatures at around 140 $^{\circ}$C have been achieved by some of the composite membranes in tests of the membrane electrode assembly (MEA) [81].

The composite membrane can be prepared via recasting polymer solution with inorganic particles [82] or via in-situ growth of inorganic solids in the preformed PFSA membrane [74,83,84]. The former approach tends to give an inhomogeneous distribution of particle size, which is less favorable for fuel cell applications; while the latter takes advantage of the pre-existing nano-scale structure of PFSA membrane and gives more homogeneous distribution of inorganic particles. However, with careful engineering of preparation conditions, both methods may achieve similar proton conductivity [30].

The enhanced water retention capability and the sustained proton conductivity of composite membranes have not been fully understood on the molecular level, despite characterizations by X-ray diffraction and scattering [85-88], electron microscopy [88,89], and NMR [57,73]. Yang et al. claimed that the inorganic particle may act as rigid scaffolds that provide the membrane with dimension stability against swelling [90], while Ye et al. [57] suggested that high density of hydroxyl groups on the particle surface are essential to facilitate proton transport. We have performed solid-state NMR investigations of the Nafion-silica and Nafion-zirconium phosphate composite membranes as detailed in Chapter 6 and 7. It has been found that the inorganic particles with an cylindrical shape are located at the center of the water channels. Water and protons are transported through the ~ 0.8-nm-thick water layer surrounding the inorganic particles.

**1.7 Organization of the dissertation**

In this dissertation, Chapter 1 introduces the fuel cell technology in terms of its principles, current challenges, and possible solutions. Chapter 2 reviews some basic NMR concepts and some solid-state techniques that are commonly used in this research. Chapter 3 presents a numerical evaluation of the surface-to-volume ratio of different models of Nafion as a function of hydration level, which supports the water channel model. Chapter 4 utilizes deuterated water to probe the persistence length of water channels in Nafion via $^2$H NMR and corresponding simulations. In Chapter 5, the structure and composition of a novel Nafion phosphatranium composite, which is a promising candidate for anion exchange membrane, have been characterized. Chapter 6 elucidates the nanometer-scale structure of Nafion-silica and Nafion-zirconium composite membranes. In Chapter 7, solid-state NMR and X-ray diffraction (XRD) have been employed to study the zirconium phosphates grown in and outside Nafion and under different preparation conditions.

**1.8 Copyright permissions**

Chapter 5 is a reprint of the paper published on "*Macromolecules*", for which the copyright permission is granted by American Chemical Society.

Chapters 3, 4, 6, and 7 are original research papers to be published.

## 1.9 References

(1)     U. Winter, H. W. *Fuel Cells* **2003**, *3*, 76-83.

(2)     L. Carrette, K. A. F., and U. Stimming *Fuel Cells* **2001**, *1*, 5-39.

(3)     G. Friedlmeier, J. F., and F. Panik *Fuel Cells* **2001**, *1*, 92-96.

(4)     Wieser, C. *Fuel Cells* **2004**, *4*, 245-250.

(5)     Cropper, M. *Fuel Cells* **2004**, *4*, 236-240.

(6)     de Bruijn, F. A.; Dam, V. A. T.; Janssen, G. J. M. *Fuel Cells* **2008**, *8*, 3-22.

(7)     EG&G Technical Services, I. *U.S. Department of Energy* **2004**.

(8)     O. Okada, K. Y. *Fuel Cells* **2001**, *1*, 72-77.

(9)     Mehta, V.; Cooper, J. S. *J. Power Sources* **2003**, *114*, 32-53.

(10)    Preli, F. *Fuel Cells* **2002**, *2*, 5-9.

(11)    Williams, M. C. *Fuel Cells* **2001**, *1*, 87-91.

(12)    Arita, M. *Fuel Cells* **2002**, *2*, 10-14.

(13)    Barbir, F.; Yazici, S. *Int. J. Energy Res.* **2008**, *32*, 369-378.

(14)    Corey, R. L.; Ivancic, T. M.; Shane, D. T.; Carl, E. A.; Bowman, R. C.; von Colbe, J. M. B.; Dornheim, M.; Bormann, R.; Huot, J.; Zidan, R.; Stowe, A. C.; Conradi, M. S. *J. Phys. Chem. C* **2008**, *112*, 19784-19790.

(15)    Corey, R. L.; Shane, D. T.; Bowman, R. C.; Conradi, M. S. *J. Phys. Chem. C* **2008**, *112*, 18706-18710.

(16)    Bazylak, A. *Int. J. Hydrogen Energy* **2009**, *34*, 3845-3857.

(17)    Tang, H. L.; Shen, P. K.; Jiang, S. P.; Fang, W.; Mu, P. *J. Power Sources* **2007**, *170*, 85-92.

(18)    Wu, J. F.; Yuan, X. Z.; Martin, J. J.; Wang, H. J.; Zhang, J. J.; Shen, J.; Wu, S. H.; Merida, W. *J. Power Sources* **2008**, *184*, 104-119.

(19)    Buchi, F. N.; Srinivasan, S. *J. Electrochem. Soc.* **1997**, *144*, 2767-2772.

(20)    Eaves, S.; Eaves, J. *J. Power Sources* **2004**, *130*, 208-212.

(21)    Cheng, X.; Shi, Z.; Glass, N.; Zhang, L.; Zhang, J. J.; Song, D. T.; Liu, Z. S.; Wang, H. J.; Shen, J. *J. Power Sources* **2007**, *165*, 739-756.

(22)    Peron, J.; Nedellec, Y.; Jones, D. J.; Roziere, J. *J. Power Sources* **2008**, *185*, 1209-1217.

(23)    Healy, J.; Hayden, C.; Xie, T.; Olson, K.; Waldo, R.; Brundage, A.; Gasteiger, H.; Abbott, J. *Fuel Cells* **2005**, *5*, 302-308.

(24)    P. Commer, A. G. C., E. Spohr, and A. A. Kornyshev *Fuel Cells* **2002**, *2*, 127-136.

(25)    Saito, M.; Arimura, N.; Hayamizu, K.; Okada, T. *J. Phys. Chem. B* **2004**, *108*, 16064-16070.

(26)    Zawodzinski, T. A.; Derouin, C.; Radzinski, S.; Sherman, R. J.; Smith, V. T.; Springer, T. E.; Gottesfeld, S. *J. Electrochem. Soc.* **1993**, *140*, 1041-1047.

(27)    Zawodzinski, T. A.; Springer, T. E.; Davey, J.; Jestel, R.; Lopez, C.; Valerio, J.; Gottesfeld, S. *J. Electrochem. Soc.* **1993**, *140*, 1981-1985.

(28)    Devanathan, R. *Energy Environ. Sci.* **2008**, *1*, 101-119.

(29)    Arico, A. S.; Baglio, V.; Di Blasi, A.; Antonucci, V. *Solid State Ionics* **2005**, *835*, 223-234

375.

(30)    Jones, D. J.; Roziere, J. *Fuel Cells I* **2008**, *215*, 219-264.

(31)    Savadogo, O. *J. Power Sources* **2004**, *127*, 135-161.

(32)    Pineri, M.; Gebel, G.; Davies, R. J.; Diat, O. *J. Power Sources* **2007**, *172*, 587-596.

(33)    Kreuer, K. D.; Paddison, S. J.; Spohr, E.; Schuster, M. *Chem. Rev.* **2004**, *104*, 4637-4678.

(34)    Kornyshev, A. A.; Kuznetsov, A. M.; Spohr, E.; Ulstrup, J. *J. Phys. Chem. B* **2003**, *107*, 3351-3366.

(35)    Dippel, T.; Kreuer, K. D. *Solid State Ionics* **1991**, *46*, 3-9.

(36)    Cui, S. T.; Liu, J. W.; Selvan, M. E.; Keffer, D. J.; Edwards, B. J.; Steele, W. V. *J. Phys. Chem. B* **2007**, *111*, 2208-2218.

(37)    Cappadonia, M.; Erning, J. W.; Niaki, S. M. S.; Stimming, U. *Solid State Ionics* **1995**, *77*, 65-69.

(38)    Paddison, S. J.; Paul, R. *PCCP* **2002**, *4*, 1158-1163.

(39)    Thompson, E. L.; Capehart, T. W.; Fuller, T. J.; Jorne, J. *J. Electrochem. Soc.* **2006**, *153*, A2351-A2362.

(40)    Paddison, S. J. *Annu. Rev. Mater. Sci.* **2003**, *33*, 289-319.

(41)    Gebel, G. *Polymer* **2000**, *41*, 5829-5838.

(42)   Hansen, E. W.; Schmidt, R.; Stocker, M. *J. Phys. Chem.* **1996**, *100*, 11396-11401.

(43)   Mishima, O.; Stanley, H. E. *Nature* **1998**, *396*, 329-335.

(44)   Mallamace, F.; Corsaro, C.; Broccio, M.; Branca, C.; Gonzalez-Segredo, N.; Spooren, J.; Chen, S. H.; Stanley, H. E. *PNAS* **2008**, *105*, 12725-12729.

(45)   Mallamace, F.; Branca, C.; Broccio, M.; Corsaro, C.; Gonzalez-Segredo, N.; Spooren, J.; Stanley, H. E.; Chen, S. H. *Eur. Phys. J. Spec. Top.* **2008**, *161*, 19-33.

(46)   Alba-Simionesco, C.; Coasne, B.; Dosseh, G.; Dudziak, G.; Gubbins, K. E.; Radhakrishnan, R.; Sliwinska-Bartkowiak, M. *J. Phys. Condens. Matter* **2006**, *18*, R15-R68.

(47)   MacMillan, B.; Sharp, A. R.; Armstrong, R. L. *Polymer* **1999**, *40*, 2481-2485.

(48)   Saito, M.; Hayamizu, K.; Okada, T. *J. Phys. Chem. B* **2005**, *109*, 3112-3119.

(49)   MacMillan, B.; Sharp, A. R.; Armstrong, R. L. *Polymer* **1999**, *40*, 2471-2480.

(50)   Boyle, N. G.; Coey, J. M. D.; Mcbrierty, V. J. *Chem. Phys. Lett.* **1982**, *86*, 16-19.

(51)   Boyle, N. G.; Mcbrierty, V. J.; Douglass, D. C. *Macromolecules* **1983**, *16*, 75-80.

(52)   Gebel, G.; Diat, O. *Fuel Cells* **2005**, *5*, 261-276.

(53)   Rubatat, L.; Rollet, A. L.; Gebel, G.; Diat, O. *Macromolecules* **2002**, *35*, 4050-4055.

(54)   Haubold, H. G.; Vad, T.; Jungbluth, H.; Hiller, P. *Electrochim. Acta* **2001**, *46*, 1559-1563.

(55)   Elliott, J. A.; Hanna, S.; Elliott, A. M. S.; Cooley, G. E. *Macromolecules* **2000**, *33*, 4161-4171.

(56)   Zawodzinski, T. A.; Neeman, M.; Sillerud, L. O.; Gottesfeld, S. *J. Phys. Chem.* **1991**, *95*, 6040-6044.

(57)   Ye, G.; Hayden, C. A.; Goward, G. R. *Macromolecules* **2007**, *40*, 1529-1537.

(58)   Chen, Q.; Schmidt-Rohr, K. *Macromolecules* **2004**, *37*, 5995-6003.

(59)   Kim, Y. S.; Wang, F.; Hickner, M.; McCartney, S.; Hong, Y. T.; Harrison, W.; Zawodzinski, T. A.; McGrath, J. E. *J. Polym. Sci., Part B: Polym. Phys.* **2003**, *41*, 2816-2828.

(60)   Bosnjakovic, A.; Schlick, S. *J. Phys. Chem. B* **2004**, *108*, 4332-4337.

(61)   Gierke, T. D.; Munn, G. E.; Wilson, F. C. *J. Polym. Sci., Part B: Polym. Phys.* **1981**, *19*, 1687-1704.

(62)    Kumar, S.; Pineri, M. *J. Polym. Sci., Part B: Polym. Phys.* **1986**, *24*, 1767-1782.

(63)    Li, J.; Wilmsmeyer, K. G.; Madsen, L. A. *Macromolecules* **2009**, *42*, 255-262.

(64)    Rubatat, L.; Gebel, G.; Diat, O. *Macromolecules* **2004**, *37*, 7772-7783.

(65)    Schmidt-Rohr, K. *J. Appl. Crystallogr.* **2007**, *40*, 16-25.

(66)    Schmidt-Rohr, K.; Chen, Q. *Nat. Mater.* **2008**, *7*, 75-83.

(67)    Hickner, M. A.; Ghassemi, H.; Kim, Y. S.; Einsla, B. R.; McGrath, J. E. *Chem. Rev.* **2004**, *104*, 4587-4611.

(68)    Schuster, M.; de Araujo, C. C.; Atanasov, V.; Andersen, H. T.; Kreuer, K. D.; Maier, J. *Macromolecules* **2009**, *42*, 3129-3137.

(69)    de Araujo, C. C.; Kreuer, K. D.; Schuster, M.; Portale, G.; Mendil-Jakani, H.; Gebel, G.; Maier, J. *PCCP* **2009**, *11*, 3305-3312.

(70)    Glipa, X.; ElHaddad, M.; Jones, D. J.; Roziere, J. *Solid State Ionics* **1997**, *97*, 323-331.

(71)    Ariza, M. J.; Jones, D. J.; Roziere, J. *Desalination* **2002**, *147*, 183-189.

(72)    Alberti, G.; Casciola, M. *Annu. Rev. Mater. Sci.* **2003**, *33*, 129-154.

(73)    Nicotera, I.; Zhang, T.; Bocarsly, A.; Greenbaum, S. *J. Electrochem. Soc.* **2007**, *154*, B466-B473.

(74)    Shao, P. L.; Mauritz, K. A.; Moore, R. B. *Chem. Mater.* **1995**, *7*, 192-200.

(75)    Shao, P. L.; Mauritz, K. A.; Moore, R. B. *Abstr. Pap. Am. Chem. Soc.* **1995**, *210*, 233-PMSE.

(76)    Costamagna, P.; Yang, C.; Bocarsly, A. B.; Srinivasan, S. *Electrochim. Acta* **2002**, *47*, 1023-1033.

(77)    Tazi, B.; Savadogo, O. *J. New Mater. Electrochem. Syst.* **2001**, *4*, 187-196.

(78)    Tazi, B.; Savadogo, O. *Electrochim. Acta* **2000**, *45*, 4329-4339.

(79)    Alberti, G.; Casciola, M.; Costantino, U.; Peraio, A.; Montoneri, E. *Solid State Ionics* **1992**, *50*, 315-322.

(80)    Glipa, X.; Leloup, J. M.; Jones, D. J.; Roziere, J. *Solid State Ionics* **1997**, *97*, 227-232.

(81)    Adjemian, K. T.; Lee, S. J.; Srinivasan, S.; Benziger, J.; Bocarsly, A. B. *J. Electrochem. Soc.* **2002**, *149*, A256-a261.

(82)  Watanabe, M.; Uchida, H.; Seki, Y.; Emori, M.; Stonehart, P. *J. Electrochem. Soc.* **1996**, *143*, 3847-3852.

(83)  Alberti, G.; Casciola, M.; Pica, M.; Tarpanelli, T.; Sganappa, M. *Fuel Cells* **2005**, *5*, 366-374.

(84)  Mauritz, K. A.; Payne, J. T. *J. Membr. Sci.* **2000**, *168*, 39-51.

(85)  Casciola, M.; Capitani, D.; Comite, A.; Donnadio, A.; Frittella, V.; Pica, M.; Sganappa, M.; Varzi, A. *Fuel Cells* **2008**, *8*, 217-224.

(86)  Young, S. K.; Jarrett, W. L.; Mauritz, K. A. *Polymer* **2002**, *43*, 2311-2320.

(87)  Deng, Q.; Cable, K. M.; Moore, R. B.; Mauritz, K. A. *J. Polym. Sci., Part B: Polym. Phys.* **1996**, *34*, 1917-1923.

(88)  Truffier-Boutry, D.; De Geyer, A.; Guetaz, L.; Diat, O.; Gebel, G. *Macromolecules* **2007**, *40*, 8259-8264.

(89)  Rodgers, M. P.; Shi, Z.; Holdcroft, S. *Fuel Cells* **2009**, *9*, 534-546.

(90)  Yang, C.; Srinivasan, S.; Bocarsly, A. B.; Tulyani, S.; Benziger, J. B. *J. Membr. Sci.* **2004**, *237*, 145-161.

# Chapter 2

# Solid State NMR for Material Characterization

## 2.1 Introduction

Understanding the relations between macroscopic properties and microscopic structure is important for the science and engineering of high-performance materials, in particular, synthetic polymers. Scattering and electron microscopy techniques have been widely applied to the structure characterizations of amorphous or semi-crystalline polymers. Though very powerful, these techniques are lack of site-specific resolution and dynamics information. Solid-state NMR is able to probe the structure and dynamics information, which are often inaccessible by other techniques, with the advantages of high resolution and non-invasive nature. The structure information is usually obtained from $^1$H, $^{13}$C, $^{15}$N, $^{19}$F, $^{29}$Si or $^{31}$P spectra under magic angle spinning. Spatial distance of two types of spins and domain sized of a heterogeneous system can be extracted from dipolar coupling strength and spin diffusion, respectively. The dynamics of a polymer can be investigated segment-by-segment through spin-lattice relaxation ($T_1$), spin-spin relaxation ($T_2$), or the exchange induced by segmental reorientations. In the following sections, some basic NMR concepts and a few solid state NMR techniques relevant to our research of fuel cell membrane are reviewed briefly.

## 2.2 Solid state NMR with magical angle spinning

In modern solid-state NMR spectroscopy, strong external magnetic field combined with carefully-sequenced radio-frequency (rf) pulses can extract a wealth of information from the tiny magnetic moments generated by nuclear spins. The success of solid state NMR lies on the well-established quantitative interpretation of local and macroscopic electromagnetic interactions through classic and quantum mechanics.

*Zeeman interaction*

In quantum mechanics, different types of electromagnetic interactions are treated as contributions to the Hamiltonian ($\hat{H}$) associated with different energy levels. The Zeeman interaction, which is the interaction between nuclear spin and external magnetic field, is the dominant part of the Hamiltonian; while other contributions with smaller energy shifts, such as quadrupolar, dipolar, electron-cloud couplings, can be calculated in terms of first-order perturbation theory.

The magnetic moment ($\vec{\mu}$) and angular momentum ($\hbar\boldsymbol{I}$) of a spin is correlated with a gyromagnetic ratio ($\gamma$):

$$\vec{\mu} = \gamma\hbar\boldsymbol{I}$$

When this magnetic moment is placed in a strong magnetic field ($\vec{\boldsymbol{B}}_0$) along z direction, the effect felt by the nuclear spin is called Zeeman interaction:

$$\hat{H}_0 = -\vec{\mu} \cdot \vec{\boldsymbol{B}}_0 = -\gamma\hbar\hat{I}_z B_0$$

where $I_z$ is the z component of $\boldsymbol{I}$ in the coordinate system.

In the lab frame, the nuclear spins under Zeeman interaction precess around $\vec{\boldsymbol{B}}_0$, and results in the characteristic Larmor frequency of each type of nuclei:

$$\omega_0 = -\gamma B_0$$

However, in a properly-chosen rotating frame, the effect of $\vec{\boldsymbol{B}}_0$ can be "minimized" and the magnetic moment can be considered static, which simplifies the mathematical treatment of the rf pulses and other local interactions.

*Chemical shift interaction*

Under the influence of the external $\vec{\boldsymbol{B}}_0$ field, the electron cloud generates a local magnetic field around the nuclear spins, whose strength scales with $\vec{\boldsymbol{B}}_0$ by a tensor-based factor $\boldsymbol{\sigma}$. The local field affects the precession frequency of the nuclear spins and it is called chemical shift interaction ($\hat{H}_{CS}$).

$$\hat{H}_{CS} = \gamma\vec{\boldsymbol{I}}\boldsymbol{\sigma}\vec{\boldsymbol{B}}_0$$

The chemical shift interaction is truncated by the $\vec{\boldsymbol{B}}_0$ field in the z direction.

$$\hat{H}_{CS} = \gamma\hat{I}_z\sigma_{zz}B_0$$

The precession frequency induced by chemical shift interaction is

$$\omega_{CS} = -\omega_0 \sigma_{zz}$$

Chemical shift is related to local chemical structure such as electron cloud density and chemical bond configuration, which is the basis for the structure elucidation of organic compounds. It customary to write chemical shift in parts per million (ppm) of the Larmor frequency and to calibrate it against a reference compound with frequency "$\omega_0$".

$$\delta = \frac{\omega - \omega_0}{\omega_0} \times 10^6 \text{ ppm}$$

The chemical shift frequency $\omega_{CS}$ contains an orientation-independent isotropic part "$\omega_{CS,iso}$", and an orientation-dependent anisotropic part "$\omega_{CS,aniso}$" which is called chemical shift anisotropy (CSA).

$$\omega_{CS} = \omega_{CS,iso} + \omega_{CS,aniso}$$

Quantitatively, CSA can be expressed as

$$\omega_{CS,aniso} = \delta \frac{1}{2} (3\cos^2\theta - 1 - \eta\sin^2\theta \cos 2\phi)$$

where $\delta$ is the anisotropy parameter and $\eta$ is the asymmetry parameter, which are related to chemical bond strength and configuration. The angle $\theta$ and $\phi$ denote the direction of $\vec{B}_0$ field in the principal axis system (PAS).
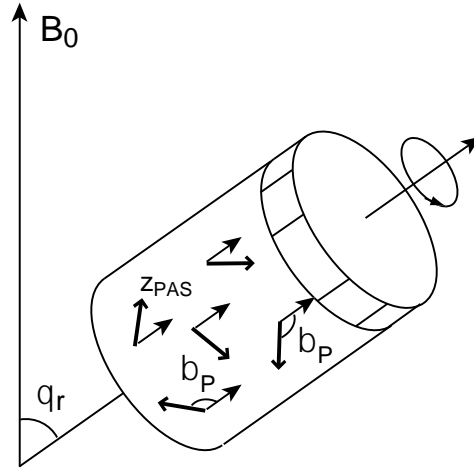
*Magic angle spinning*

In solution state, CSA effect is usually not significant because of the fast molecular tumbling. However, in amorphous solids, CSA is one of the major reasons that broaden the signal lineshapes, which might obscure useful information. As a result, magic angle spinning (MAS), which is used to eliminate or reduce the effect of CSA, is of great importance in solid-state NMR. In MAS experiments, solid samples undergo fast uniaxial rotation at the so-called "magic angle" with respect to the $\vec{B}_0$ field.

When a sample undergoes uniaxial rotation with a frequency exceeding the strength of chemical shift interaction, the expression of CSA changes to

$$\omega_{CS,aniso} = \delta \frac{1}{2} (3\cos^2\beta_P - 1 - \eta\sin^2\beta_P \cos 2\alpha_P) \frac{1}{2} (3\cos^2\theta_r - 1)$$

where $\theta_r$ is the angle between the rotation axis and the $\vec{B}_0$ field, while $(\alpha_P, \beta_P)$ denote the polar coordinates of the rotation axis in the principal axis system (PAS), see Figure 2.1. $\delta$ is the anisotropy parameter and $\eta$ is the asymmetry parameter of the chemical shift interaction.

**Figure 2.1.** Illustration of magic angle spinning.

When $\theta_r$ is set to 54.7° (magic angle), the $\omega_{CS,aniso}$ is effectively zero under fast rotation. Fast MAS can give narrow resonance lines that resemble solution state NMR. But in case MAS spinning speed is smaller than the frequency span of the CSA, significant spinning sidebands are generated, due to periodic modulations of the frequency given in the following equation [1]:

$$\omega(t) = C_1\cos(\gamma + \omega_r t) + S_1\sin(\gamma + \omega_r t) + C_2\cos(2\gamma + 2\omega_r t) + S_2\sin(2\gamma + 2\omega_r t)$$

where $C_1$, $S_1$, $C_2$, and $S_2$ depend on $\delta$, $\eta$ and the Euler angles $(\alpha, \beta, \gamma)$ which rotates PAS into the rotor axis frame. Sometimes, the TOSS (total suppression of spinning sidebands) pulse sequence is used to eliminate undesired spinning sidebands.

*Dipolar interaction*

Dipolar interaction, also called dipolar coupling, exists between nearby nuclear spins and it plays an important role in solid state NMR. First, it broadens the NMR spectra and affects the $T_1$ and $T_2$ relaxation times; second, it contains distance information that is exceptionally useful for structure determination. The Hamiltonian of dipolar coupling is:

$$\widehat{H}_D = \vec{\mathbf{I}}^i \cdot \mathbf{D}^{ij} \cdot \vec{\mathbf{I}}^j$$

where $\mathbf{D}^{ij}$ is the tensor of dipolar interaction.

Under the $\vec{\mathbf{B}}_0$ field, the dipolar coupling Hamiltonian is truncated to the components along z-axis in the lab frame.
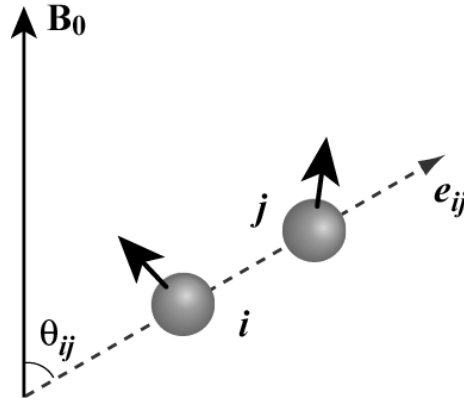
For homonuclear dipolar coupling

$$\widehat{H}_D = \hbar \frac{\mu_0}{4\pi} \frac{\gamma^2}{r_{ij}^3} \frac{1}{2} \left(3\cos^2\theta_{ij} - 1\right)[3\hat{I}_z^i \hat{I}_z^j - \vec{\mathbf{I}} \cdot \vec{\mathbf{I}}]$$

For heteronuclear dipolar coupling

$$\widehat{H}_D = \hbar \frac{\mu_0}{4\pi} \frac{\gamma^I \gamma^S}{r_{IS}^3} \left(3\cos^2\theta_{IS} - 1\right)\hat{I}_z \hat{S}_z$$

where $\mu_0$ is the magnetic permeability, $\gamma$ is the gyromagnetic ratio, $r$ is the internuclear distance, and $\theta$ is the angle between the $\vec{\mathbf{B}}_0$ field and the internuclear vector $e_{ij}$ (Figure 2.2). The prefactor $\hbar \frac{\mu_0}{4\pi} \frac{\gamma^I \gamma^S}{r_{IS}^3}$ is called the dipolar coupling constant



**Figure 2.2.** Illustration of the dipolar interaction between two nuclear spins.

As seen from the equations, the internuclear distance information can be extracted from the dipolar coupling constant, which contains the distance-dependent term of $1/r^3$. The rotational-echo double-resonance (REDOR) pulse sequence is widely used in solid state NMR to quantitatively measure internuclear distance between heteronuclear spins. A brief description of the REDOR sequence will be given in section 2.3.

Also, the dipolar coupling is orientation dependent, which lead to line broadening of the solid state NMR spectra. But unlike CSA, which can be averaged by MAS in many cases, the strength of the dipolar coupling, especially between high $\gamma$ nuclei such as $^1$H-$^1$H, $^1$H-$^{13}$C, and $^1$H-$^{31}$P, exceeds normal spinning speed of MAS. Decoupling pulse sequences have to be used to suppress the undesired effect of dipolar coupling. For homonuclear dipolar decoupling, WAHUHA [2], MREV-8 [3], and FSLG [4] pulse sequences are widely used to achieve high resolution $^1$H spectra. For heteronuclear dipolar decoupling, continuous rf irradiation or the TPPM pulse sequence [5] can be applied to the non-detected $^1$H channel to decouple $^{13}$C or $^{31}$P from surrounding proton spins.

Indirect dipolar coupling also called "J-coupling", which only exists through chemical bonds, is often negligible in solid-state NMR of unlabeled materials because its magnitude is usually much smaller than the CSA and direct dipolar interaction, and the heteronuclear J-coupling is removed by heteronuclear decoupling.

*Relaxation*

NMR relaxation describes a process that nuclear magnetization $M(t)$ returns to its equilibrium state after the application of rf pulses. This process can be expressed empirically through the Bloch equations:

$$\frac{dM_{xy}}{dt} = -\frac{1}{T_2} M_{xy}$$

$$\frac{dM_z}{dt} = -\frac{1}{T_1}(M_z - M_z^\infty)$$

where $M_z^\infty$ is the magnetization at equilibrium.

The relaxation rate can be decomposed into two: the longitudinal relaxation rate "$1/T_1$" and the transverse relaxation rate "$1/T_2$". The equations can be simplified as follow, assuming that the transverse component $M_{xy}^\infty = 0$ at equilibrium while the initial longitudinal component $M_z^0 = 0$ as for the saturation-recovery pulse sequence.

$$M_{xy}(t) = M_{xy}^0 e^{-\frac{t}{T_2}}$$

$$M_z(t) = M_z^\infty (1 - e^{-\frac{t}{T_1}})$$

With these equations, the relaxation time $T_2$ and $T_1$ can be easily extracted via simple Hahn-echo and saturation-recovery pulse sequences, respectively. However, the mechanisms that lead to relaxation are often complicated. Briefly, the $T_1$ relaxation time is affected by the fluctuation and the strength of local magnetic field. Since $T_1$ relaxation involves an energy exchange with surroundings, it is also called spin-lattice relaxation. $T_1$ has a minimum where molecular motion rate is close to Larmor frequency of nuclei.

The $T_2$ relaxation corresponds to the decoherence of transverse magnetization. $T_2$ relaxation is also affected by the random fluctuation of local field; but since it involves only the phases of nuclear spins, it is called spin-spin relaxation. The $T_2$ relaxation is generally less dependent on field strength. For pure substances, the well-known BPP theory [6] can quantitatively correlate $T_1$ and $T_2$ relaxation time to the rate of molecular motion.

## 2.3 Internuclear distance measurements

Internuclear distance is an important parameter for structural characterization. NMR offers reliable internuclear distance measurement especially for non-crystalline samples, which is usually not accessible by X-ray techniques. In NMR, the distance information is encoded in the dipolar coupling constant shown in Section 2.1. Under MAS conditions, the homonuclear dipolar coupling can be explored by the DRAMA pulse sequence [7] and the heteronuclear dipolar coupling between two spin-1/2 nuclei can be explored by the REDOR pulse sequence [8]. They both utilize rotor-synchronized pulses to recover dipolar coupling that is being averaged by MAS. The REDOR (rotational-echo double-resonance) pulse sequence has been used a lot in the characterizations of polymers and inorganic solids. A simple version of the REDOR pulse sequence is shown in Figure 2.3.
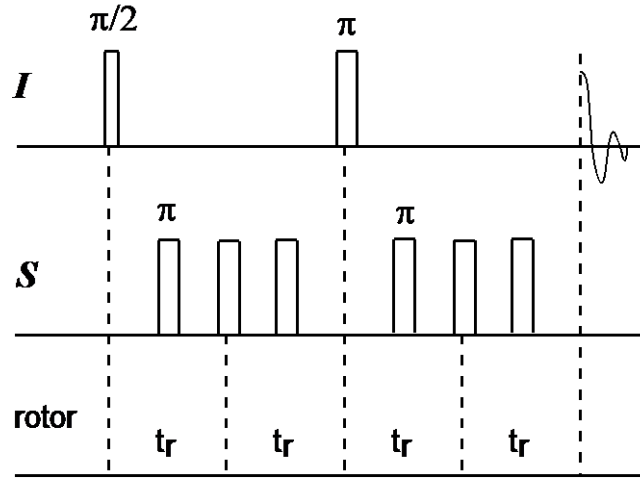
**Figure 2.3.** REDOR pulse sequence.

In this REDOR sequence (Figure 2.3), a $\pi$-pulse is applied to the detected $I$ spin to refocus chemical shift evolution in a Hahn echo and a series of $\pi$ pulses are applied to the $S$ spin at every half rotor period ($t_r/2$) except at the center. It has been shown that all the rotor periods have equivalent effects on recoupling dipolar coupling between $I$ and $S$ spins [9].

We first analyze the average spin-pair dipolar coupling Hamiltonian ($\bar{H}_D$) in a full rotor period without the application of $\pi$ pulses.

$$\bar{H}_D = \frac{1}{t_r} \int_0^{t_r} \hat{H}_D(t) \, dt$$

Here we need to consider the time-dependence of $\hat{H}_D(t)$ in the rotor-axis frame:

$$\bar{H}_D = \frac{1}{t_r} \int_0^{t_r} 2d_{IS} \left[ \frac{1}{\sqrt{2}} \sin 2\beta \cos(\omega_r t + \gamma) - \frac{1}{2} \sin^2 \beta \cos(2\omega_r t + 2\gamma) \right] \hat{I}_z \hat{S}_z \, dt$$

$$= 0$$

where $d_{IS} = \hbar \frac{\mu_0}{4\pi} \frac{\gamma^I \gamma^S}{r_{IS}^3}$ is the dipolar coupling constant, ($\beta$, $\gamma$) are the Euler angles that rotates dipolar PAS coordinates into rotor-axis frame. It is easily seen that the $\bar{H}_D$ after a full rotor period equals to zero, since $\omega_r t_r = 2\pi$. Without $\pi$ pulses on S channel and with fast MAS, the dipolar coupling experienced by $I$ is motional averaged and its magnetization is fully recovered.

However, when a $\pi$ pulse, which inverts the sign of $\hat{S}_z$, was added to the center of each rotor period:

$$\bar{H}_D = \frac{1}{t_r}\left[\int_0^{t_r/2} \hat{H}_D(t)\,\mathrm{d}t + \int_{t_r/2}^{t_r} -\hat{H}_D(t)\,\mathrm{d}t\right]$$

$$= \frac{1}{t_r}\left[2\int_0^{t_r/2} \hat{H}_D(t)\,\mathrm{d}t - \int_0^{t_r} \hat{H}_D(t)\,\mathrm{d}t\right]$$

$$= \frac{2}{t_r}\int_0^{t_r/2} \hat{H}_D(t)\,\mathrm{d}t$$

So

$$\bar{H}_D = \left(-\frac{2\sqrt{2}d_{IS}}{t_r}\sin 2\beta \sin\gamma\right)\hat{I}_z\hat{S}_z$$

This nonvanishing $\bar{H}_D$ contributes to a phase shift $\Delta\phi = -\frac{2\sqrt{2}d_{IS}}{t_r}\sin 2\beta \sin\gamma$ in the final $I$ magnetization and results in a reduced signal intensity $\mathbf{S}(t_r)$

$$\frac{\mathbf{S}(t_r)}{\mathbf{S_0}(t_r)} = \cos\Delta\phi$$

Here, $\mathbf{S}(t_r)$ is the signal intensity with recoupling $\pi$ pulses and $\mathbf{S_0}(t_r)$ is the reference signal intensity without $\pi$ pulses.

For a powder sample and with N rotor cycles:

$$\frac{\mathbf{S}(Nt_r)}{\mathbf{S_0}(Nt_r)} = \frac{1}{2\pi}\int_0^{\pi/2}\int_0^{2\pi} \cos[N\Delta\phi(\beta,\gamma)]\sin\beta\,\mathrm{d}\gamma\mathrm{d}\beta$$

Normally, the dephasing is plotted as $\mathbf{S}/\mathbf{S_0}$ against a series of $Nt_r$ and the curve can be fitted according to above equations. Therefore, the dipolar coupling constant $d_{IS}$ is determined and the internuclear distance is eventually obtained.

However, the derivation above only considers a spin pair. The situation is usually more complicated in polymer composites, where $I$ spin may be coupled to multiple $S$ spins e.g. $^{13}$C or $^{31}$P surrounded by abundant $^{1}$H or $^{19}$F spins. In this situation, the initial dephasing rate of the $\mathbf{S}/\mathbf{S_0}$ curve is expected to be exponential [10,11]:

$$\frac{\mathbf{S}(t_r)}{\mathbf{S_0}(t_r)} = \exp(-Wt)$$

Considering a space populated with $S$ spins, the dephasing rate $W \propto 1/r_{min}^3$, where $r_{min}$ is the smallest distance between $I$ and $S$ spins. This relation can be used in the complex systems such as Nafion inorganic nanocomposites to estimate internuclear distance based on a reference compound.

For distance measurements between spin-1/2 and quadrupolar nuclei, modified recoupling sequences such as TRAPDOR[12] and REAPDOR[8] may be used.

## 2.4 2D heteronuclear and homonuclear correlation spectroscopy

2D correlation spectroscopy has been widely used to explore the connectivity or spatial proximity of nuclear spins in different chemical environments. The correlations are usually based on the through-space dipolar coupling in solid state, and it may involve the same type of nuclei, termed "homonuclear", or different types of nuclei, termed "heteronuclear". For polymer and polymer composites, 2D correlation NMR enables the separation of locally heterogeneous environments and the study of dynamics.
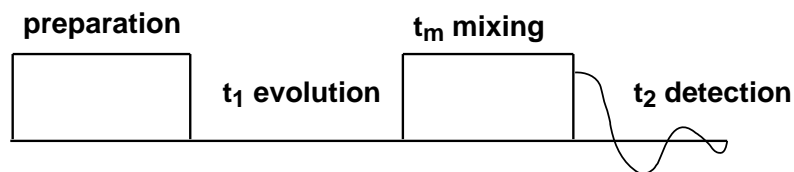


**Figure 2.4.** Building blocks of a typical 2D pulse sequence.

A typical 2D pulse sequence (Figure 2.4) can be divided into four periods: preparation – evolution ($t_1$) – mixing ($t_m$) – detection ($t_2$). The preparation period includes the time for recycle delay and the excitation by a single pulse or cross polarization. The $t_1$ evolution period is incremented with a dwell time in successive experiments. It contains the signals in the first dimension (F1), which are indirectly detected as modulations of the time-domain signal later observed during detection period $t_2$. The mixing period allows the spins to exchange magnetizations through dipolar coupling (so-called spin diffusion) or other exchange processes. The mixing time $t_m$ can be varied to identify short and long distances and to probe the rate of dynamics. The signal detected during the $t_2$ period for a single

experiment at a particular $t_1$ increment contributes to the signals in the second dimension ($\omega_2$), while the set of signal points collected for all $t_1$ increment contributes to the signals in the $\omega_1$ dimension. A simple illustration of the conversion process from time-domain signals to a 2D spectrum is shown in Figure 2.5. Mathematically, the translation is accomplished via 2D Fourier transform through either amplitude modulation or phase modulation [1].
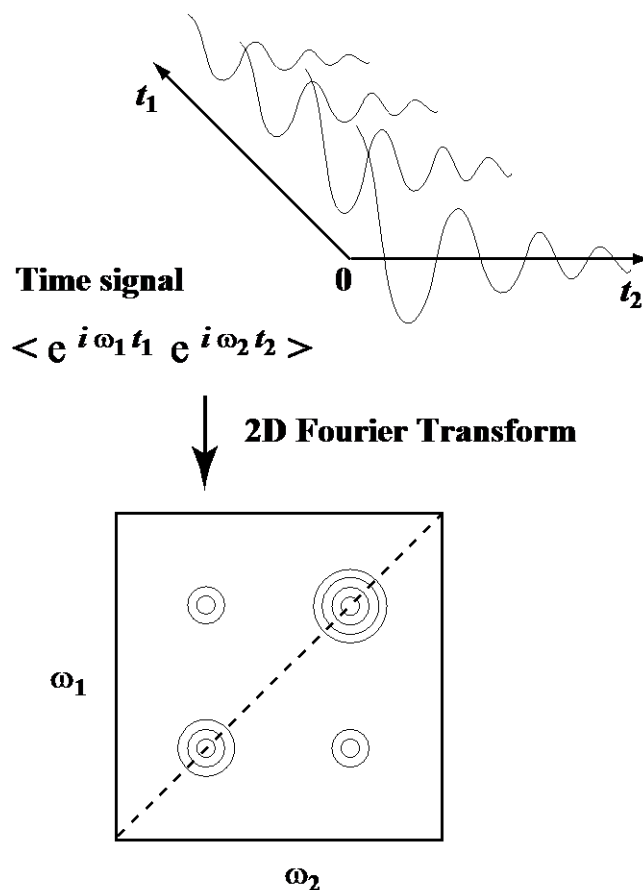


**Figure 2.5.** Conversion from a 2D time signal into a 2D NMR spectrum.

In a homonuclear correlation spectrum, the diagonal peaks represent a 1D spectrum that is governed by chemical shifts; the off-diagonal peaks indicate the correlations e.g. spatial proximity between each two spin sites. In a heteronuclear correlation spectrum, the peaks indicate the correlations between different nuclei e.g. $^{1}$H-$^{13}$C, $^{1}$H-$^{31}$P, $^{1}$H-$^{29}$Si. Figure 2.6 shows the pulse sequences that are commonly used in our research: 2D exchange, wide-line separation (WISE), and heteronuclear correlation (HetCor).
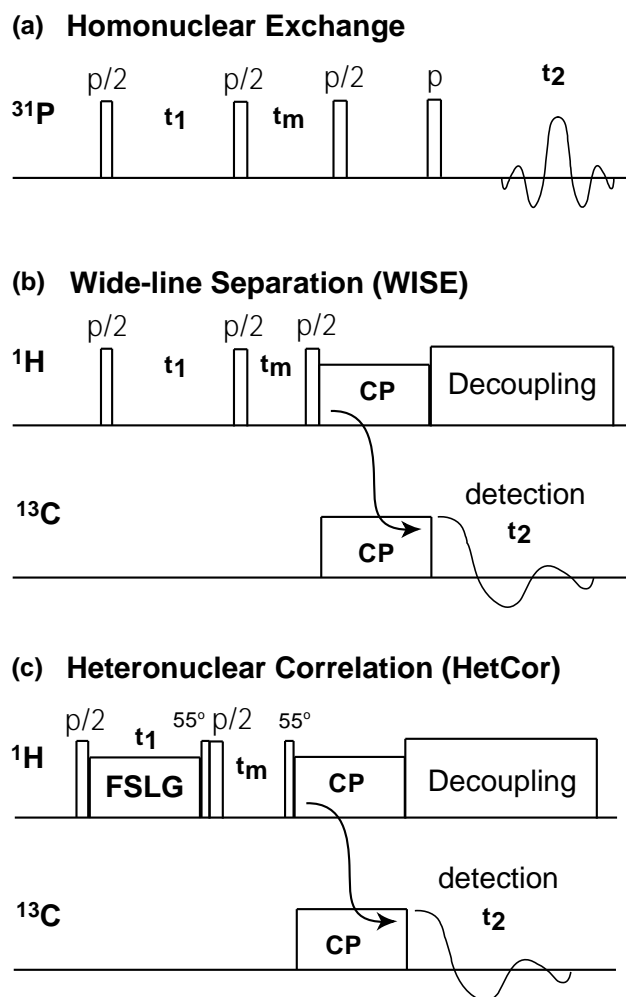
**Figure 2.6.** 2D correlation pulse sequences. (a) $^{31}$P 2D exchange. (b) $^{1}$H-$^{13}$C WISE. (c) $^{1}$H-$^{13}$C HetCor.

The WISE experiment was initially designed to separate signals of protons with different dynamics (reflected in the linewidth) for different carbon sites in heterogeneous polymers [13]. For systems with weak $^{1}$H-$^{1}$H dipolar couplings, it also correlates $^{1}$H and $^{13}$C chemical shifts. However, this can be achieved with higher resolution using the HetCor experiment has homonuclear decoupling pulses e.g. FSLG during the $t_1$ evolution period [14]. The FSLG pulse sequence used in HetCor introduces a scaling factor on the frequencies in the $\omega_1$ dimension [15], which is sometimes inconvenient for proton chemical shift assignment, while in WISE, this problem does not arise. In our research, WISE and HetCor experiments are often combined,

where WISE is used to help determine the chemical shifts in the $\omega_1$ dimension and HetCor is used to obtain higher resolution.

## 2.5 Dynamics and orientation studied by $^2$H NMR

$^2$H is a quadrupolar nucleus with spin $I = 1$. Unlike $I = 1/2$ nuclei such as $^1$H, $^{13}$C and $^{31}$P, which have a point charge distribution, the electric charge in a quadrupolar nucleus is unevenly distributed, which gives rise to a nuclear electric quadrupole moment "$Q$". This quadrupole moment interacts with any electric field gradient at the nuclei, and the strength of the interaction usually dominates over other interactions e.g. CSA and dipolar interaction. The Hamiltonian of the quadrupolar interaction is written as:

$$\widehat{H}_Q = \frac{eQ}{2I(2I-1)\hbar} \hat{\vec{\mathbf{I}}} \mathbf{V} \hat{\vec{\mathbf{I}}}$$

After truncation by the $\vec{\boldsymbol{B}}_0$ field:

$$\widehat{H}_Q = \frac{eQ}{2I(2I-1)\hbar} V_{zz}^{\text{LF}} \frac{1}{2} (3\hat{I}_z \hat{I}_z - \hat{\vec{\mathbf{I}}} \cdot \hat{\vec{\mathbf{I}}})$$

where $e$ is the elementary charge, $\mathbf{V}$ is electric field gradient with tensor components $V_{\alpha\beta}$, and $\hat{\vec{\mathbf{I}}} \cdot \hat{\vec{\mathbf{I}}} = \hat{I}_x \hat{I}_x + \hat{I}_y \hat{I}_y + \hat{I}_z \hat{I}_z$.

For $^2$H with $I = 1$, the quadrupolar Hamiltonian matrix reads:

$$\mathbf{H}_Q = \frac{\omega_Q}{3} \begin{bmatrix} 1 & 0 & 0 \\ 0 & -2 & 0 \\ 0 & 0 & 1 \end{bmatrix}$$

where $\omega_Q = \frac{1}{2} \delta_Q (3\cos^2\theta - 1 - \eta_Q \sin^2\theta \cos 2\phi)$ with the quadrupole coupling strength $\delta_Q = \frac{3eQeq}{4\hbar}$, and $(\theta, \phi)$ specifying the orientation of $\vec{\boldsymbol{B}}_0$ in the principal axes system of electric gradient $\mathbf{V}$. For $^2$H, the asymmetry parameter $\eta_Q$ is usually zero due to the approximate uniaxiality of the electron density in $\sigma$ bonds, which is the common chemical environments of $^2$H.

The quadrupolar interaction of $^2$H leads to an oscillation of the observable NMR signal with a frequency $\omega_Q$:

$$\cos \omega_Q t = \frac{1}{2} e^{i\omega_Q t} + \frac{1}{2} e^{-i\omega_Q t}$$

As a result, $^2$H NMR spectra are symmetric. The $^2$H spectrum of a powdered sample is a double-horn pattern (Figure 2.7).
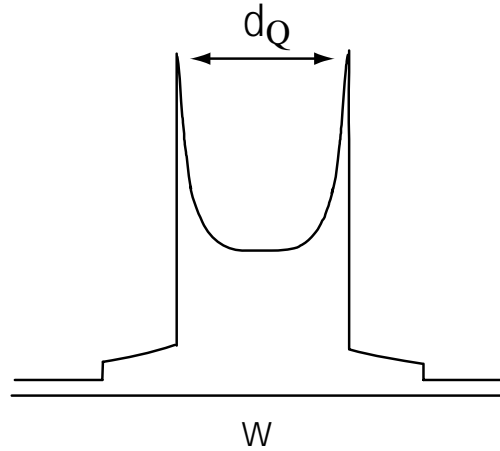


**Figure 2.7.** A powder pattern of $^2$H spectrum.

In $^2$H spectra of rigid samples, the splitting between the two horns measures the value of $\delta_Q$. For an aliphatic C-$^2$H bond, $\delta_Q \cong 2\pi \times 130$ kHz [1]. However, due to molecular motion and reorientation, the observed $^2$H quadrupolar splitting $\bar{\delta}_Q$ is sometimes much smaller. Based on the narrowing of $^2$H quadrupolar splitting and the orientation dependence, the molecular dynamics and anisotropy of materials can be investigated [16-18]. $^2$H NMR has been applied to Nafion hydrated with $D_2O$ to study the local anisotropy and orientational order [19,20]. In the Chapter 3, we deduce the persistence length of water channels based on the simulation of the motional averaged $^2$H quadrupolar splitting of $D_2O$ in Nafion.

## 2.6 References

(1)     Schmidt-Rohr, K.; Spiess, H. W. *Multidimensional Solid-state NMR and Polymers* Academic Press Limited **1994**.

(2)     Haeberle.U; Waugh, J. S. *Phys. Rev.* **1968**, *175*, 453-&.

(3)     Rhim, W. K.; Elleman, D. D.; Vaughan, R. W. *J. Chem. Phys.* **1973**, *59*, 3740-3749.

(4)     Mehring, M.; Waugh, J. S. *Phys. Rev. B: Condens. Matter* **1972**, *5*, 3459-&.

(5)     Bennett, A. E.; Rienstra, C. M.; Auger, M.; Lakshmi, K. V.; Griffin, R. G. *J. Chem. Phys.* **1995**, *103*, 6951-6958.

(6)     Bloembergen, N.; Purcell, E. M.; Pound, R. V. *Phys. Rev.* **1948**, *73*, 679-712.

(7)     Tycko, R.; Dabbagh, G. *Chem. Phys. Lett.* **1990**, *173*, 461-465.

(8)     Gullion, T.; Schaefer, J. *J. Magn. Reson.* **1989**, *81*, 196-200.

(9)     Duer, M. J. *Solid-State NMR Spectroscopy: principles and applications* Blackwell Science Ltd. **2002**.

(10)    Mao, J. D.; Schmidt-Rohr, K. *J. Magn. Reson.* **2003**, *162*, 217-227.

(11)    Schmidt-Rohr, K.; Rawal, A.; Fang, X. W. *J. Chem. Phys.* **2007**, *126*, -.

(12)    Grey, C. P.; Veeman, W. S. *Chem. Phys. Lett.* **1992**, *192*, 379-385.

(13)    Schmidt-Rohr, K.; Clauss, J.; Spiess, H. W. *Macromolecules* **1992**, *25*, 3273-3277.

(14)    Bielecki, A.; Burum, D. P.; Rice, D. M.; Karasz, F. E. *Macromolecules* **1991**, *24*, 4820-4822.

(15)    vanRossum, B. J.; Forster, H.; deGroot, H. J. M. *J. Magn. Reson.* **1997**, *124*, 516-519.

(16)    Ward, I. M. Applied Science Publishers Ltd **1982**.

(17)    Spiess, H. W. *Pure Appl. Chem.* **1985**, *57*, 1617-1626.

(18)    Spiess, H. W. *Adv. Polym. Sci.* **1985**, *66*, 23-58.

(19)    Li, J.; Wilmsmeyer, K. G.; Madsen, L. A. *Macromolecules* **2009**, *42*, 255-262.

(20)    Chen, R. S.; Jayakody, J. P.; Greenbaum, S. G.; Pak, Y. S.; Xu, G.; Mclin, M. G.; Fontanella, J. J. *J. Electrochem. Soc.* **1993**, *140*, 889-895.

# Chapter 3

# Water-Polymer Interface in Nafion and the Parallel Water Channel Model

Xueqian Kong, Klaus Schmidt-Rohr

To be submitted as a *Note* to *J. Polym. Sci. Polym. Phys. Ed.*

**Abstract**

The water-polymer interfacial area, which is reflected in the Porod region of small-angle scattering data, is an important parameter of different models of the Nafion fuel cell membrane. Therefore, we have compared published experimental data of Nafion with various structural models, in particular the parallel water-channel model. The surface-to-volume ratio extracted at intermediate hydration levels typical of fuel-cell conditions matches that of the parallel water-channel model with molecular corrugation. In addition, it is shown that for less than 3.5 water molecules per Nafion sidegroup, the interfacial area must increase strongly with hydration, contrary to the predictions of the polymer bundle model.

**Introduction**

Recently, we introduced a new and relatively simple model of Nafion, the benchmark material for proton-exchange membranes in fuel cells [1,2], based on quantitative simulations of small-angle scattering data. [3] It features parallel water channels with diameters around 2.4 nm (at 20 vol% $H_2O$) and includes elongated crystallites. We also reproduced the changes in small-angle scattering curves with increasing hydration. Nevertheless, it has been suggested that this model is not valid because it predicts water-polymer interfacial areas increasing with hydration, while small-angle scattering supposedly shows a constant interfacial area. [4] To address this issue, in this Note we compare published experimental interfacial areas in hydrated Nafion of 1100 equivalent weight from the Porod region of SAXS curves [5,6] with predictions by various structural models, focusing on the low to intermediate hydration levels up to 30 vol% $H_2O$ relevant in fuel-cell conditions.

**Results**

**Experimental data from the literature**. Figure 1 shows S/V data points for Nafion 1100 as a function of water volume fraction, obtained by Gebel et al. [5] and Kreuer et al. [6] from analysis of the Porod region of SANS and SAXS data, respectively. In the range of 29 to 92 vol% water the surface-to-volume ratio, normalized for the polymer volume fraction, has been found to be essentially constant. [5,7] These samples were mostly prepared at high pressure, and the water volume fraction is mostly higher than in the fuel-cell environment. The result has been reported in terms the area per sidegroup, $\sigma = 0.55$ nm$^2$. With the volume $v_0 = 0.87$ nm$^3$ per sidegroup [5], one can calculate the surface-to-volume ratio

$$S/V = \phi_p \, \sigma/v_0 = \phi_p \, 0.63/\text{nm} \tag{3.1}$$

where $\phi_p$ is the polymer volume fraction. The error margins deduced from the Porod plot in Figure 3.1 B of ref.5 are $\pm 10\%$. The complete set of experimental data suggests a slightly higher value of $\sigma = 0.6$ nm$^2$ per headgroup.

**Structural constraints.** The fact that hydrated Nafion does not phase separate into dry polymer and liquid water shows that it is favorable for the sulfonate groups to be hydrated. Then, in constructing or considering structural models of Nafion, the main constraint is the ~3.6 nm dimension of two Nafion molecules packed back-to-back. At all but extremely low water contents, any point in the polymer, apart from ~10% of crystalline material, should be within $\leq 3.6$ nm/2 = 1.8 nm from the nearest polymer-water interface. Our water-channel model presented in ref.3 fulfills this requirement. This thickness constraint excludes thick polymer bundles or large spacings between water channels. On the other hand, thick layers of water or varying diameters of water channels are possible. As a result, S/V values for $\phi_p$ and 1- $\phi_p$ do not have to be equal or even similar, which explains the lack of symmetry of the plot in Figure 3.1.

Further, stiffness of the Nafion polymer backbones is clearly an important structural aspect. Mainly due to the large size of the fluorine substitutents, the backbone of Nafion forms a helix that is relatively stiff [8,9] compared to its protonated analogues, and therefore the Nafion matrix is not unstructured on the scale of the diameter of the hydrated clusters; this

accounts for the formation of bundles of polymer in excess water and excludes spherical clusters of diameters approaching the intrinsic 3.6-nm length scale.

**S/V in the polymer ribbon model.** In a polymer ribbon model with N ribbons of width w, thickness $d_p$, length L, and polymer volume fraction

$$\phi_p = N\ L\ w\ d_p/V_{tot}, \tag{3.2}$$

the surface-to-volume ratio is

$$S/V = N2L(w+d)/V_{tot} = 2\ \phi_p(w+d_p)/(wd) \tag{3.3}$$

For wide ribbons, $w >> d_p = \phi_p\ L_p$ with the long period $L_P$ and the expression simplifies to

$$S/V = \phi_p\ 2/d_p \tag{3.4}$$

The ribbon thickness $d_p$ can be estimated from the polymer fraction $\phi_p$ and long period $a_p$ derived from the ionomer peak position q* in SAXS, [10] q* $= 2\pi/a_p$ in this simple one-dimensional situation of stacked ribbons. For $\phi_w = 0.2$ and $a_p = 4$ nm, [10] we find d $= \phi_p\ a_p = 3.2$ nm and thus Eq. 3.4 gives

$$S/V = (1 - \phi_w)\ 0.63/nm. \tag{3.5}$$

This is shown as a thin line in Figure 3.1. It should be pointed out that both polymer ribbon and wide-layer models have failed to reproduce the experimental scattering data at the hydration levels relevant for fuel-cell membranes. [3]

**S/V in the polymer bundle model with cylindrical bundles.** In a polymer bundle model with N bundles of radius R, length L, and polymer volume $\phi_p = N\pi R^2 L/V_{tot}$, the surface-to-volume ratio is

$$S/V = N\ 2\pi RL/V_{tot} = \phi_p\ 2/R = (1-\phi_w)\ 1.1/nm \tag{3.6}$$

with the radius R = 1.8 nm of a polymer bundle based on form-factor (rather than S/V) analysis in ref. [11]. This is shown by a dotted line in Figure 3.1, which lies generally above the experimental data points. The discrepancy will be reduced by contacts between bundles, which will reduce the surface area, but if many such contacts occur, the identity of the bundles will be compromised, and the model ceases to be a bundle model.

**Low-$\lambda$ regime.** At low hydration values, the limited surface area of the available water molecules represents an important additional constraint on the S/V ratio and the possible structures. Each water molecule has a surface area $\sigma_{H2O}$; the maximum water-polymer surface-to-volume ratio is the surface area of $\lambda$ water molecules per sidegroup, divided by the volume per sidegroup, 0.87 nm$^3$: [5]

$$\text{S/V} \leq \lambda \, \sigma_{H2O}/0.87 \text{ nm}^3 \approx 29 \, \phi_W \, \sigma_{H2O}/0.87 \text{ nm}^3 \qquad (3.7)$$

Here, we have used relations between $\phi_w$, relative volume change $\Delta V$, and relative mass changes $\Delta m$, respectively: [10]

$$\phi_w = 1 - 1/(1+\Delta V) \approx \Delta V \qquad (3.8)$$

$$\text{and} \quad \Delta V = \frac{\rho_{dry}}{\rho_{H_2O}} \Delta m = \frac{\rho_{dry}}{\rho_{H_2O}} \, 18/1100 \, \lambda = 0.034 \, \lambda \qquad (3.9)$$

This shows that in this regime S/V *increases* with $\phi_W$, approximately linearly, while the extrapolation of the experimental data from large hydration levels [5] and the polymer bundle model incorrectly predict a *decrease* in S/V with increasing $\phi_W$.

The relevant surface area $\sigma_{H2O}$ of a water molecule can be estimated from its effective diameter of ~0.3 nm (values between 0.28 – 0.32 nm have been reported[12] ) in various ways. In a spherical approximation, the total surface area is $\sigma_{H2O} = 4 \, \pi \, (0.3 \text{ nm}/2)^2 = 0.28 \text{ nm}^2$, but not all parts of the molecule can interact with a convex or planar surface as in the polymer bundle or ribbon models. Then, a cylinder with two circular surfaces of total area of $\sigma_{H2O} = 2 \, \pi \, (0.3 \text{ nm}/2)^2 = 0.14 \text{ nm}^2$ is a better approximation. It might still be an overestimate because often a double layer of water molecules would be more favorable; then $\sigma_{H2O} = \pi \, (0.3 \text{ nm}/2)^2 = 0.07 \text{ nm}^2$. With a surface area of the sulfonate group of $\sigma_{SO3} = 0.6$ nm$^2$ and using,

conservatively, $\sigma_{H2O} \leq 0.2$ nm$^2$, we must conclude that for $\lambda \leq 3$ water molecules per sulfonate group, the interfacial area *cannot* reach the full water coverage required for the polymer bundle model. On the other hand, the concave surface of a narrow water channel is quite suitable for enhancing contact between the water molecules and the sulfonate groups in this low-hydration regime. In summary, this analysis shows that the extrapolation of the experimental data from high hydration levels [5] and the corresponding predictions of the polymer bundle model cannot be correct at low hydration levels.

**S/V for smooth cylindrical channels.** We have shown quantitative evidence that in the hydration regime relevant for fuel cells, around $\lambda = 7$, locally parallel water channels exist in Nafion. [3] In a simple water-channel model with N smooth circular-cylindrical channels of diameter d and length L, the water volume fraction and surface-to-volume ratio are given by

$$\phi_w = N\pi(d/2)^2 L/V_{tot} \tag{3.10}$$

$$S/V = N \pi dL/V_{tot} = 4/(d/\phi_w) = \phi_w \, 4/d \tag{3.11}$$

The channel diameter d increases with water volume fraction according to $\phi_w = V_w/(V_0+V_w)$, where $V_0$ and $V_W$ are the volumes of dry polymer and of water, respectively. Assuming a fixed number N of clusters, we have again $V_w = N\pi(d/2)^2 L$, and with $V_w = \phi_w/(1-\phi_w) \, V_0$ we obtain

$$d = 2 \, (V_0 \, \phi_w/(1-\phi_w))^{1/2} \, 1/(N\pi L)^{1/2} \tag{3.12}$$

and thus

$$S/V = (\phi_w(1-\phi_w))^{1/2} \, 2 \, (N\pi L/V_0)^{1/2} \tag{3.13}$$

With $V_0 = N \, L \, 0.87 \, a_0^2$, where $a_0$ is the "long period" of the unswollen structure approximated as hexagonally packed, see Figure 3.2a, this simplifies to

$$S/V = (\phi_w(1-\phi_w))^{1/2} \, 1/a_0 \, 2(\pi/0.87)^{1/2} \quad V = (\phi_w(1-\phi_w))^{1/2} \, 3.8/a_0 \tag{3.14}$$

With $a_0 = 3.5$ nm, we obtain

$$S/V \; (\phi_w(1-\phi_w))^{1/2} \; 1.1/nm \tag{3.15}$$

which was confirmed by comparison with S/V extracted from the simulations of ref.3. This function is very steep for small $\phi_w$, but flattens out quickly, see the left-hand side of Figure 3.1.

In order to modify the simple relation between S/V and $\phi_w$, we could invoke a large change in the number N of water channels per given volume of polymer. However, on a molecular level, there is no rationale for such a major structural reorganization. The high speed of water uptake [13] also speaks in favor of limited changes in the polymer structure with hydration.
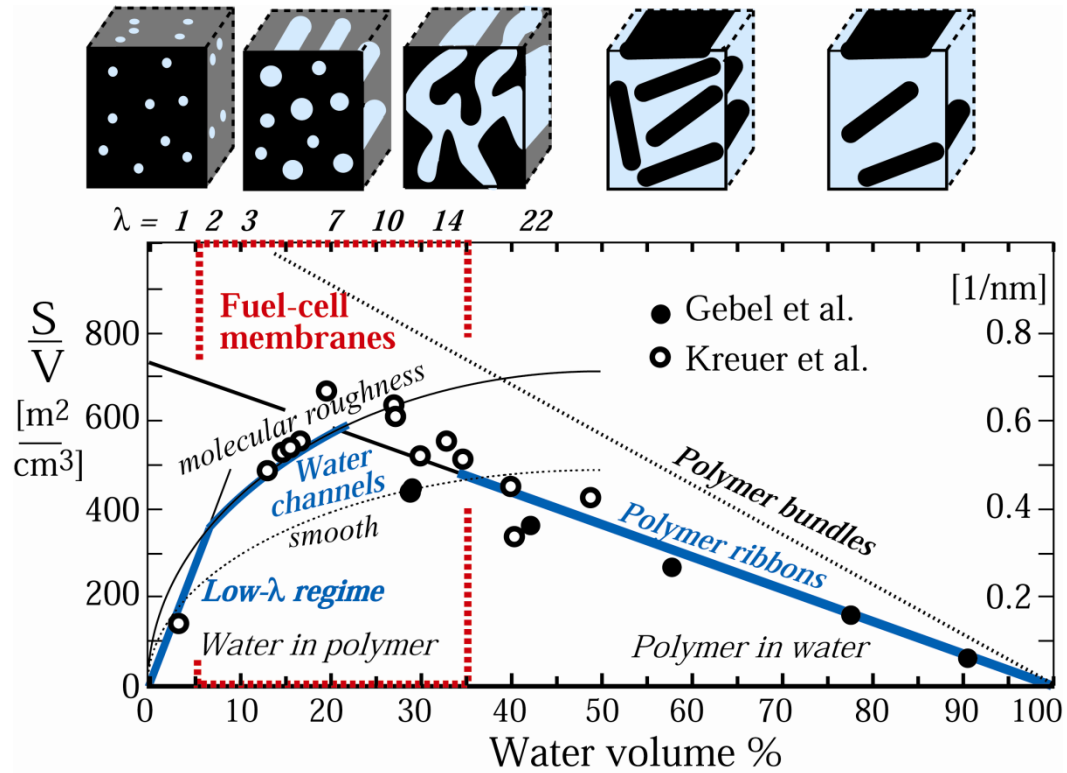


**Figure 3.1**. Plot of the surface-to-volume ratio of Nafion 1100. Experimental data points from references 1 and 2 are compared with curves for several models. From left to right: The straight line with positive slope is obtained in the low-$\lambda$ regime; the dashed and continuous rising curves are calculated from the parallel-water-channel model with smooth water cylinders (dashed) and constructed on a square lattice with a distribution of channel diameters [3] or with molecular roughness of the interface (continuous); straight lines of negative slope are obtained from models featuring polymer bundles (dashed line) and

polymer ribbons (continuous line). At the top of the figure, models featuring dispersed water molecules, parallel water channels, and polymer ribbons in water are shown schematically. The transitional model shown at the center, between channel and ribbon models, was not explicitly analyzed in this paper.

**S/V for water channel with molecularly resolved surface features.** With channel diameters on the 2.5-nm scale, the assumption of perfectly smooth cylinders is clearly an unrealistic approximation. Molecular roughness of the interface must be taken into account on this scale. The van-der-Waals diameter of a sulfonate group or folded sidechain is on the order of 0.6 nm. At a given volume fraction, the smooth circular cylinder has the smallest S/V of all cylinders. Any shape distortion or surface corrugation will give a larger S/V value.

The surface area of the cylindrical water channels on the cubic lattice from ref.3 corresponds to the surface of square channels of sidelength d, whose area is bigger by $4d/(\pi d)$ = $4/\pi$ = 1.3 than that of smooth cylindrical channels, see Figure 3.2b. Similarly, in the channel for $\lambda = 7$ sketched in Figure 3.2c with some molecular detail, the curved sidegroups have a ~1.4-times larger surface area than the corresponding smooth cylindrical channel. The curved continuous line in Figure 3.1 (labeled "molecular roughness") corresponds to this situation.

At the lowest hydration levels, the water-channel model becomes unrealistic when the channel radius shrinks below the dimension of a water molecule. Then, the low-$\lambda$ regime discussed above, with isolated water molecules, is reached.

**Expansion of water channels**. We should provide a plausible molecular-level description of how the diameter of a water channel can expand. As indicated in Figures 3.2c and 3.2d, each polymer molecule carries one sidebranch per 0.8 nm length projected onto the channel axis, on average. Thus, the sidebranches shown in Figures 3.2c and 3.2d are not all in the same plane, but distributed over a 0.8 nm length. At a hydration level of $\lambda = 7$ water molecules surrounding each sidegroup, the hydration shells overlap strongly throughout the volume shown. At lower hydration levels of $\lambda \approx 2$, the channel can shrink by moving sidegroups "on top of each other" in the z-direction, see Figure 3.2d.

**Discussion**

The experimental S/V data in Figure 3.1 are well matched by three of the models discussed in this paper. In particular, in the hydration range relevant in fuel cells, we find good agreement with the water-channel model [3], which also reproduces all details of the small-angle scattering data. At the lowest hydration levels, we have identified the available surface area of water molecules as the determining factor, while in the other extreme, for polymer in an excess of water, the ribbon model of Rubatat et al. [14] provides a good fit. All the models discussed are compatible with the significant stiffness (persistence length of 2 to 5 nm) of the Nafion backbone [8].

This paper has focused on the comparison of experimental S/V ratios in Nafion with those of models that are supported by other structural analyses. A detailed analysis of free energies is beyond its scope. In addition, it is not clear that the ribbon structures at high hydration levels are actually energetically favorable. Nafion in excess liquid water does not disperse but remains a swollen solid with $\lambda = 22$ [13] for years. The data shown in Figure 3.1 in the high-hydration range were in fact obtained for samples hydrated at high temperature and pressure in a water-filled autoclave. [11]

It has been argued that an increase in S/V with hydration could not occur in Nafion because this would result in an increase of the interfacial energy of the system. However, our analysis has shown that at the lowest hydration level, the interfacial area *must* increase with water content since it is limited by the surface area of the water molecules. In other words, under these conditions the bundle and ribbon models cannot apply, since the available water molecules are insufficient to form a layer around each polymer bundle.
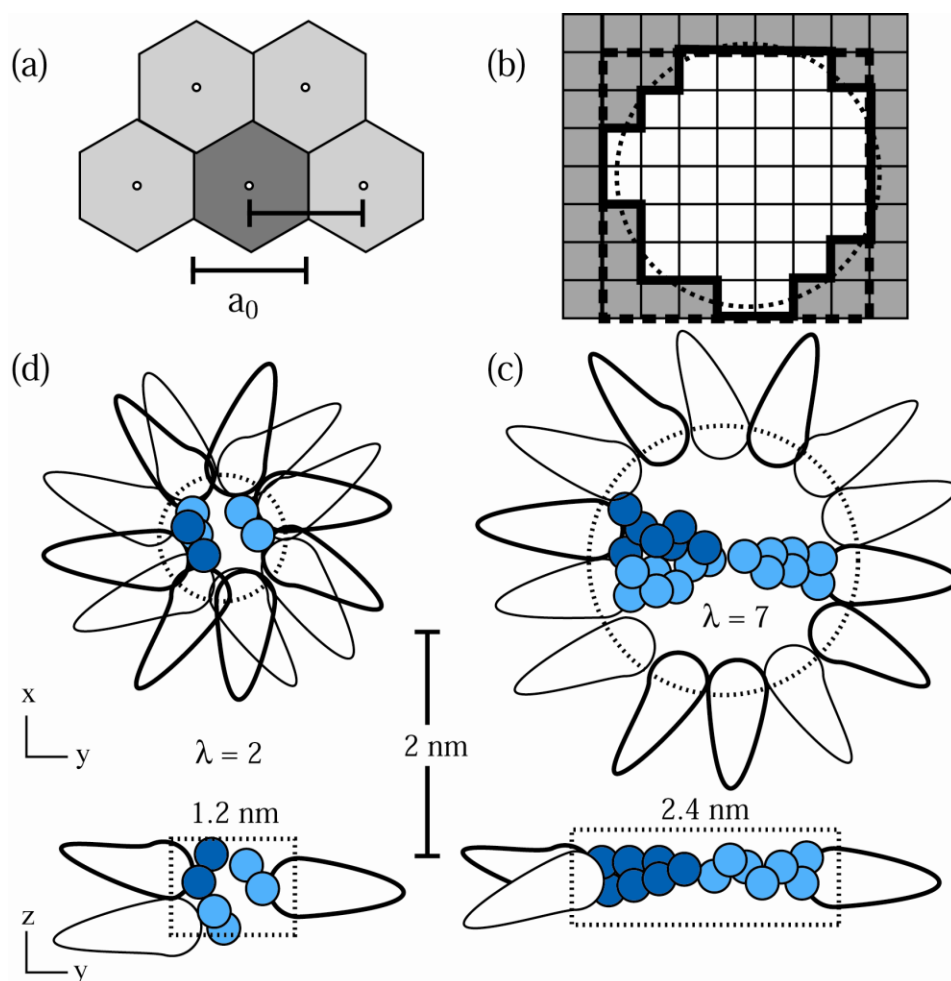
**Figure 3.2.** Representation of geometrical relations for surface-to-volume calculation in the parallel water-channel model of Nafion. (a) Relation between the (lateral) long period $a_0$ for vanishing hydration and the area $A_P$ of polymer (dark shaded hexagon) per channel (central circle), which is $A_P = a_0^2 * 3^{1/2}/2$. (b) The circumference of a water channel cross section constructed of small squares is equal to that of the square that encloses it (dashed line) and thus larger than that of the smooth circular cross section (dotted line) that it approximates. An element square is counted as being inside the channel if its center is inside the dotted circle. (c,d) Schematic representation of how the arrangement of ionic sidegroups (shown drop-shaped) could change with hydration level in the water-channel model. Top: View along the axis of a 0.8-nm long section of water channels for (c) $\lambda = 7$ and (d) $\lambda = 2$. Water molecules of one sidegroup are shown as dark disks, those associated with two neighboring sidegroups as light disks. Sidegroups that are at different depths along the channel at low hydration ($\lambda = 2$) are shown with thick and thin outlines, respectively. Bottom: Side views of 0.8-nm-long cross sections through the channel.

## Conclusions

Our analysis of the water-polymer surface-to-volume ratio S/V of Nafion as a function of hydration has shown that in the range typical of fuel-cell operation, the parallel water channel model matches the experimentally observed S/V values. Bundle or ribbon models are suitable for polymer dispersed in an excess of water, but not for water as a minority phase (< 20 vol%) in a polymer matrix. At the lowest hydration levels, bundle or ribbon models deviate strongly from the experimental data and are physically impossible since the surface area of the available water molecules is not sufficiently large to cover the bundle surface.

## Acknowledgement

## References

(1)     Devanathan, R. *Energy Environ. Sci.* **2008**, *1*, 101-119.

(2)     Mauritz, K. A.; Moore, R. B. *Chem. Rev.* **2004**, *104*, 4535-4585.

(3)     Schmidt-Rohr, K.; Chen, Q. *Nat. Mater.* **2008**, *7*, 75-83.

(4)    Gebel, G.; Kreuer, K. D. *Private Communication at CARISMA 2008 Conference* **2008**.

(5)     Gebel, G. *Polymer* **2000**, *41*, 5829-5838.

(6)     Kreuer, K. D.; Paddison, S. J.; Spohr, E.; Schuster, M. *Chem. Rev.* **2004**, *104*, 4637-4678.

(7)     Gebel, G.; Lambard, J. *Macromolecules* **1997**, *30*, 7914-7920.

(8)     Chen, Q.; Schmidt-Rohr, K. *Macromol. Chem. Phys.* **2007**, *208*, 2189-2203.

(9)     RosiSchwartz, B.; Mitchell, G. R. *Polymer* **1996**, *37*, 1857-1870.

(10)    Gierke, T. D.; Munn, G. E.; Wilson, F. C. *J. Polym. Sci., Part B: Polym. Phys.* **1981**, *19*, 1687-1704.

(11)    Rubatat, L.; Gebel, G.; Diat, O. *Macromolecules* **2004**, *37*, 7772-7783.

(12)    Franks, F. *Water: a matrix of life, 2nd Edition* Royal Society of Chemistry, Cambridge **2000**.

(13)    Zawodzinski, T. A.; Derouin, C.; Radzinski, S.; Sherman, R. J.; Smith, V. T.; Springer, T. E.; Gottesfeld, S. *J. Electrochem. Soc.* **1993**, *140*, 1041-1047.

(14)    Rubatat, L.; Rollet, A. L.; Gebel, G.; Diat, O. *Macromolecules* **2002**, *35*, 4050-4055.

# Chapter 4

# An Estimate of the Persistence Length of Water Channels in Nafion from $^2$H NMR of D$_2$O

Xueqian Kong, Robert B. Moore, Klaus Schmidt-Rohr

**Abstract**

We have estimated the persistence length of the water channels in Nafion through a quantitative analysis of line narrowing and T$_2$ relaxation in $^2$H NMR of D$_2$O in Nafion. In drawn Nafion where scattering shows that the channels are mostly oriented along the draw direction, a 1-2 kHz quadrupolar $^2$H splitting is observed, which means that the quadrupolar interaction tensor, essentially fixed to the D$_2$O molecule, does not undergo fully isotropic tumbling. The hydration dependence of the spectral splittings and relaxation times indicates exchange between bound water affected by the anisotropic environment of the straight channels and free water in the channel core. In unoriented Nafion, the splitting is ~10-fold smaller. This means that the drawn and unoriented films differ not only in the orientation distribution of μm-size structural units, but in the orientation and structure on the length scale of D$_2$O diffusion on the 1/(1 kHz) = 1 ms NMR time scale. The observed ~10-fold motional averaging in the undrawn relative to the drawn film is explained by diffusion of water along coiled channels, which results in additional motional averaging. Thus, the persistence length of the channels must be much shorter than the diffusion length $<x^2>^{1/2} = (2\ D\ t)^{1/2} = 1$ μm of water on the 1-ms NMR time scale, with a diffusion coefficient of $D \sim 10^{-5}$ cm$^2$/s = 1 μm$^2$/ms. The quantitative analysis of NMR frequency exchange via diffusion along and orthogonal to a model channel, using an exchange algorithm suitable for long channels, shows that the persistence length of the channels in Nafion is within 30 and 80 nm, which is near the lower limit of the value estimated from small-angle scattering.

## Introduction

Nafion, a perfluorinated ionomer with a hydrophobic backbone and hydrophilic sulfonic acid side groups, is the benchmark material for proton exchange membranes (PEMs) in hydrogen-oxygen fuel cells [1-3]. Hydrated Nafion is an excellent proton conductor and highly permeable to water. We have introduced a new and relatively simple model of Nafion based on quantitative simulations of small-angle scattering data [4] and NMR [5,6]. It features parallel water channels with diameters around 2.4 nm (at 20 vol% $H_2O$) lined by the hydrophilic sidegroups and includes elongated crystallites of the polymer backbone, as indicated schematically in Figure 4.1. We also reproduced the changes in small-angle scattering curves with increasing hydration, and excluded many other models [4].
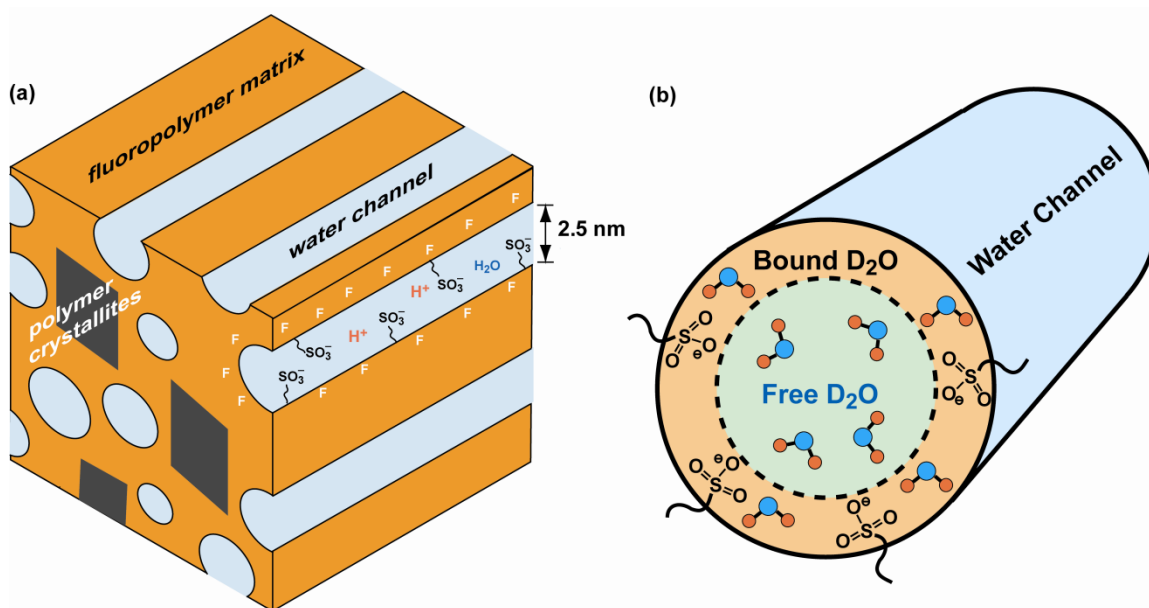


**Figure 4.1**. (a) Parallel water channel model of Nafion. (b) Cross section of a water channel. The water molecules that strongly interact with $SO_3^-$ groups near channel wall are regarded as "bound water", while those with weak constraints near the channel center are regarded as "free water".

While the structure on a 20-nm scale is well constrained by the scattering analysis, the length scale on which the water channels in Nafion are essentially straight (the persistence length) has not been determined with high accuracy. While the range of the $I(q) \sim q^{-1}$ power law in the small-angle scattering curve appears to suggest a persistence length > 100 nm [7,8],

we have shown in simulations that undulations of the channels and crystallites on the 20-nm scale do not change the $I(q)$ curve greatly [4]. In addition, the relevant low-q intensity is dominated by scattering by the crystallites, which may have a different persistence length than the water channels.

In this paper, we report an estimate of the persistence length of the channels in Nafion 117 by ^{2}H NMR of $D_2O$ in the channels. Due to the presence of bound water and the cylindrical shape of the water channels, see Figure 4.1b, the ^{2}H frequency of $D_2O$ in drawn Nafion remains orientation dependent, with a unique axis along the local channel axis. [9,10] We exploit diffusion of $D_2O$ along the curved channels, which results in frequency changes that produce additional motional narrowing of the ^{2}H NMR spectrum, compared to the spectrum of a drawn sample with straightened water channels, see Figure 4.2. We have developed a simple two-dimensional approach to measure the quadrupolar spectrum and splitting with optimum resolution independent of field inhomogeneity. From quadrupolar splittings of $D_2O$ in drawn Nafion and $T_1$ relaxation data measured as a function of hydration, we have estimated the fraction of bound water in the channels. On that basis, we have simulated the spectra and [2]H $T_2$ relaxation of $D_2O$ molecules moving along model channels of various persistence lengths, and more slowly perpendicular to the bundle of channels. Thus, we estimate an upper limit to the channel persistence length in undrawn Nafion. In previous ^{2}H NMR studies of $D_2O$ in Nafion [9], the preferential orientation of the channels in the commercial Nafion membrane and in drawn samples was studied, but the effects of diffusion along the channels were not considered.
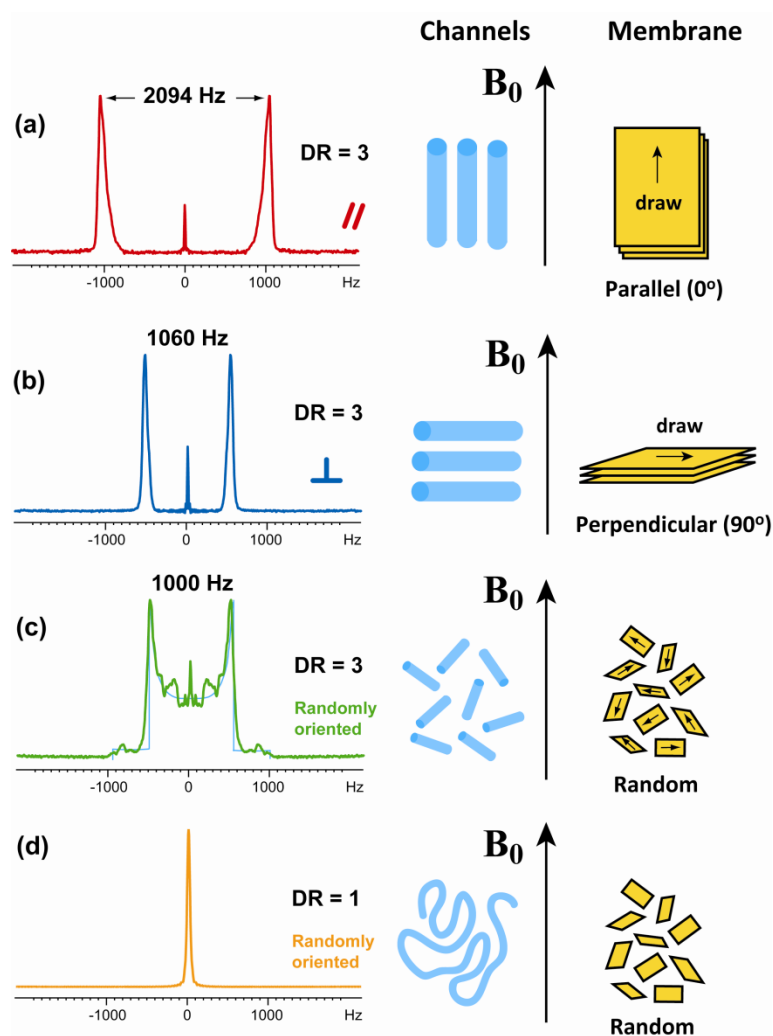
**Figure 4.2.** $^2$H NMR spectra of $^2H_2O$ in (a-c) drawn Nafion (DR = 3) and (d) regular Nafion (DR = 1) with $\lambda = 7$, prepared by Method I. (a) Draw direction parallel to $B_0$, (b) perpendicular to $B_0$, and (c) same drawn material cut into pieces. A simulated "powder" spectrum for an unoriented sample is shown using a dashed line. (d) Spectrum of undrawn Nafion (cut into small pieces), showing additional motional narrowing. The sharp peak in the center of spectra (a-c), which accounts for less than 5% of the total intensity, is due to pulse length imperfection.

**Experimental**

**Samples**.

*Pretreatment*

Nafion 117 membranes with draw ratios (DR) from 1 to 4 (DR = 1 means that the membrane was not drawn) were produced with the procedure described below. Most measurements in this paper have used these samples, labeled as "DR = n". In Figure 4.13, the results of boiled samples and as-received samples were also shown. The boiled samples were pretreated by boiling in 0.5M $H_2SO_4$ and then boiling in deionized water repeatedly to leak out paramagnetic ions; while as-received membranes were used without pretreatment.

*Uniaxial Orientation of As-Received $H^+$-Nafion.*

Extruded Nafion$^{®}$ 117CS from E.I. DuPont de Nemours & Co. (1100 g/equivalent, sulfonic acid form) was pre-cleaned by refluxing in aqueous 8M nitric acid for 2 h, and then in deionized (DI) water for 1 hr. These cleaned membranes were dried at 70 $^{o}$C for 12 hr in a vacuum oven. Uniaxially oriented samples were prepared by cutting the vacuum-dried $H^+$-Nafion$^{®}$ membranes into dog-bone shapes and mounting them on a specially designed drawing apparatus. This drawing apparatus allowed $H^+$-Nafion$^{®}$ membranes to be drawn at 150 °C (above the α-relaxation temperature of $H^+$-form[11]) to draw ratios (DR = final length (L) / initial length ($L_0$)) ranging from 1 to 4 as determined by the displacement of ink marks on the samples. Stretching rate was 10 mm /min and temperature was increased from room temperature to 150 $^{o}$C at a rate of 6 $^{o}$C /min. As soon as the desired draw ratio was reached, the membranes were rapidly quenched to room temperature to prevent thermal relaxation. [10] Uniaxially oriented, dry $H^+$-form membranes were then mounted in Kel-F clamps and soaked in DI water for 24 hr.

*Sample packing*

For oriented samples, Nafion films were cut into strips with dimensions of ~ 2 mm × 10 mm. For drawn Nafion, the draw directions of a stack of strips were carefully aligned. The strips were then securely fixed into a 5-mm-wide NMR glass tube. Later, the tubes were carefully placed in the NMR probe with lateral coil with the membrane or draw direction fixed along

the orientations as needed. For unoriented samples, the Nafion films were cut into small pieces with less than $2 \times 2$ mm$^2$ sizes. The pieces were then packed with random orientations into a glass tube.

*Hydration procedures*

These packed samples were first dried under vacuum overnight at room temperature and weighed. It was assumed that the vacuum-dried sample contains one water molecules per –SO$_3$ group. The hydration level is expressed in term of $\lambda$, which indicates the number of water molecules per –SO$_3$ group. [12]After drying, different hydration methods have been used.

Method I is to add a weighed amount of D$_2$O matching a desired hydration level the dry membranes. The samples were then sealed and stored for weeks for them to reach equilibrium before NMR measurements. However, the hydration level ($\lambda$) determined by this method may not always be reliable as seen from the large variations of T$_1$ and T$_2$ relaxation times at a selected hydration level for different samples. A 0.5 mg uncertainty in weight will translate into a considerable error in hydration level especially for samples weighing only tens of milligrams.

In Method II, the dry membranes were stored in a D$_2$O humidified chamber with saturated NaCl/D$_2$O solution. The hydration level is expected to be constant for different batches and it can be determined from representative piece of membrane with larger mass. The hydration level determined from Method II could be more consistent than Method I, but it is hard to obtain samples with different hydration levels.

In Method III, measurements of various hydration levels were achieved through the successive dehydration of the same sample in vacuum, which is similar to the procedure introduced by Li et al. The hydration level is determined from weight difference as well. The Method III mitigates the systematic error generated by different samples, and thus gives more consistent results.

**NMR parameters.** The NMR measurements were performed on a Bruker DSX400 spectrometer at a $^2$H frequency of 61.4 MHz in a static probe with a horizontal radio-frequency coil. The quadrupolar splitting was measured with a 2D pulse sequence. A Hahn

echo was used in the $\omega_1$ dimension to eliminate effects of field inhomogeneity and refocus chemical shift evolution. Pure quadrupolar spectra that allow the accurate measurement of the $^2$H quadrupolar splitting were obtained by projection onto the $\omega_1$ dimension. A z-filtered pulse sequence with solid echo before detection was used for $T_1$ measurement and a pulse sequence with Hahn-solid-Hahn echo was used for $T_2$ measurements.
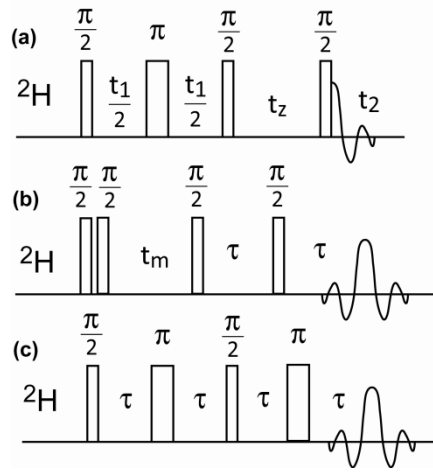


**Figure 4.3**. (a) Pulse sequence for measuring the $^2$H quadrupolar spectrum without broadening by field inhomogeneity. (b) Pulse sequence for $T_1$ measurement, by varying $t_m$. (c) Pulse sequence for $T_2$ measurement, by varying $\tau$.

For oriented samples, the draw direction (in the membrane plane) was carefully aligned with respect to the $B_0$ field. The angle between them was fixed at $0^o$ (parallel), $90^o$ (perpendicular) or $60^o$ (near the magic angle of $54.7^o$) during measurement.

**Simulations**

**Persistence length $L_p$.** The straightness of the water channels in Nafion is quantified by the persistence length $L_p$: the larger $L_p$, the straighter the channels. Formally, $L_p$ is defined as the length along the channel over which correlations in the direction of the tangent decay to $1/e$:

$$\langle \cos \chi(x) \rangle = e^{-x/L_P} \tag{4.1}$$

For our analysis, we describe the curved channel as a chain of segments of length *a*. We use a freely jointed chain, i.e. with random "torsion angles", and with a moderate "bond angle" ($\chi \approx 15^o$) between segments. The segment length a and bond angle $\chi$ are related to the persistence length $L_p$ according to

$$\cos\chi = \exp(-a/L_p) \qquad\qquad (4.2)$$

In the simulations, the persistence length $L_p = -a/\ln(\cos\chi)$ was controlled by adjusting the segment length a.

**Simulation of D$_2$O diffusion along a curved channel**. We calculate the NMR frequency of D$_2$O in segment j as

$$\omega_j = \bar{\delta}_Q (3\cos^2\theta_j - 1)/2 \qquad\qquad (4.3)$$

from the scalar product $\cos\theta_j$ between the B$_0$ field and the direction of segment j. The coupling constant $\bar{\delta}_Q$ is determined experimentally below. It has been adjusted for the different value of $\lambda^{bound}$ for undrawn and drawn Nafion determined from the hydration dependence of T$_1$ relaxation (see below). Under normal fuel cell working conditions, $\lambda = 7$, which corresponds to 11 wt% and 20 vol% H$_2$O, so $\bar{\delta}_Q = 8$ kHz $\times$ 1/7 $\times$ 0.4/0.62 = 0.7 kHz was used for the simulation of the unstretched Nafion channels.

Following Abragam [13], we can simulate the $^2$H spectrum of D$_2$O diffusing along the chain by solving the precession-and-exchange equation of the x-y magnetization, written as a complex number M$_j$, of D$_2$O in segment j:

$$\frac{dM_j}{dt} = i\omega_j M_j(t) + \sum_k \pi_{jk} M_k(t) \qquad\qquad (4.4)$$

where the exchange matrix $\bar{\bar{\pi}}$ of the diffusion process is

$$\ddot{\pi} = \begin{bmatrix} -W & W & 0 & 0 & \dots \\ W & -2W & W & 0 & \dots \\ 0 & W & -2W & W & \dots \\ 0 & 0 & W & -2W & \dots \\ 0 & 0 & 0 & W & \dots \end{bmatrix} \tag{4.5}$$

with the exchange rate W, which relates to the diffusion coefficient via the square of the segment length "a",

$$D = W\,a^2. \tag{4.6}$$

The channel (curved chain) and corresponding chain of frequencies are sketched in Figures 4.4a and 4.4b, respectively. The signal S(t) is proportional to the total magnetization $\Sigma_{j=1}^{N}$ $M_j(t)$, which is given by

$$S(t) = \vec{1}^{T}\exp(i\ddot{\omega}t + \ddot{\pi}t)\vec{1} \tag{4.7}$$

where $\ddot{\omega}$ is a diagonal matrix with elements $\omega_{jj} = \omega_j$, and $\vec{1}$ is a vector of N elements which are all unity. [13] Compared to most previous simulations of $^2$H intermediate exchange, N is rather large in our problem. To speed up the calculation, we reduced the problem from repeated calculations of exponentials of matrices to simple matrix multiplication. Writing $\ddot{E}$ (t) = $\exp(i\ddot{\omega}t_{dw} + \ddot{\pi}t_{dw})$, we used

$$\ddot{E}(t+t_{dw}) = \ddot{E}(t) \times \ddot{E}_{dw} \tag{4.8}$$

with

$$\ddot{E}_{dw} = \exp(i\ddot{\omega}t_{dw} + \ddot{\pi}t_{dw}) \tag{4.9}$$

The spectrum is obtained by Fourier transformation of S(t). The chain used in the simulations is selected to have a very small average frequency $\Sigma_{k=1}^{N} \omega_k /N$, otherwise a splitting is observed in the spectra of channels with short persistence length. Since many different segmental orientations are present in the chain, powder averaging is not required.
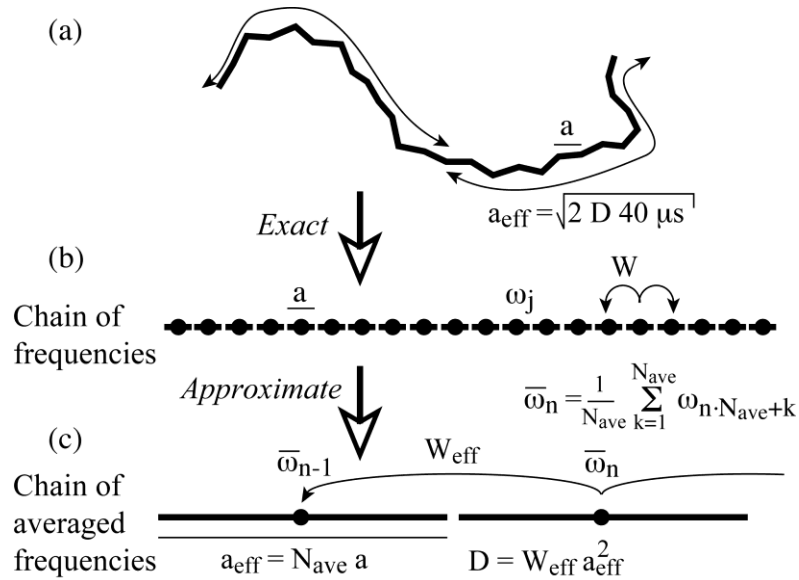


**Figure 4.4.** Principle of $^2$H NMR simulations with curvilinear diffusion (a) Freely jointed chain with segments of length a. (b) Corresponding chain of $^2$H quadrupolar frequencies. (c) Effective chain with increased segment length $a_{eff}$; fast diffusion pre-averages the frequencies on this length scale (double arrows in (a)).

**$^2$H T$_2$ simulation**. Due to motion along the channel, the D$_2$O frequency changes on the ms time scale. This results in imperfect refocusing of the quadrupolar dephasing in a T$_2$ measurement by the Hahn-solid-Hahn echo pulse sequence (see Figure 4.3c). While the 180$^o$ pulses only refocus the field-inhomogeneity effects and can be ignored in the simulation, the central solid-echo 90$^o$ pulse effectively inverts the phase $\omega t$ of the quadrupolar evolution, to -$\omega t$. Thus, the relaxation curve can be simulated according to

$$R_2(t) = \vec{1}^T \exp(i\vec{\omega}t/2 + \vec{\pi}t/2)\exp(-i\vec{\omega}t/2 + \vec{\pi}t/2)\vec{1} \qquad (4.10)$$

$T_2$ is more reliable than the spectral line width for assessing the motional averaging, since partial orientation of the sample increases the line width but not $T_2$ relaxation.

**Effective-chain simulation.** The approach outlined so far is too time-consuming for long chains. But if the chain is shorter than the diffusion length, the molecule keeps sampling the same frequencies, rather than experiencing further frequency changes, which results in erroneously long $T_2$ relaxation times and small line widths. We can speed up the calculation by using an effective chain of effective segments, see Figure 4.4c, constructed based on the following heuristic arguments: Intensity modulations within one dwell time ($t_{ave} \approx 0.05$ ms) of the NMR time signal are insignificant, since we have little spectral intensity at the Nyquist frequency. Within this time $t_{ave}$, a $D_2O$ molecule diffuses over a length

$$a_{eff} = (2D\ t_{ave})^{1/2}, \tag{4.11}$$

which contains $N_{ave}$ segments of length a,

$$N_{ave} = a_{eff}/a \tag{4.12}$$

Typically, $N_{ave} = 100$. The fast exchange between the frequencies of the $N_{ave}$ segments is not important, only the average frequency

$$\overline{\omega}_n = \frac{1}{N_{ave}} \sum_{k=1}^{N_{ave}} \omega_{n \cdot N_{ave}+k} \tag{4.13}$$

experienced by the $D_2O$ molecule.

Therefore, we replace the original chain of N segments of length a with frequencies $\omega_j$ with an effective chain of $N_{ave}$ segments of length $a_{eff}$ with frequencies $\overline{\omega}_n$. The effective exchange rate ($W_{eff}$) needs to be chosen such that the diffusion coefficient remains unchanged,

$$W_{eff}\, a_{eff}^{2} = D = W\, a^{2} \qquad\qquad (4.14)$$

Figure 4.5, which compares the simulated spectrum and $T_2$ relaxation curve for an effective chain with $N_{ave}$ = 32 with those of the full simulation, shows good agreement between the two approaches; the effective-chain simulation was several orders of magnitude faster. The smaller number of segments in the chain of averaged frequencies enables the use of much longer chains (~80 µm in length).
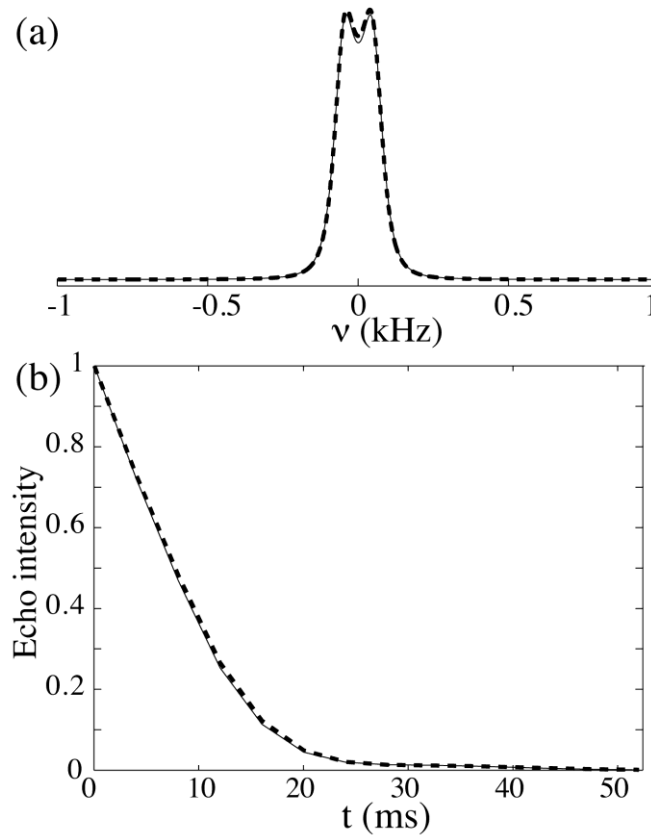


**Figure 4.5.** Demonstration of the equivalence of the original and the effective chain for simulation of (a) $^2$H NMR spectra and (b) $T_2$ relaxation for $D_2O$ diffusion along a curved channel. Continuous thin line: Regular simulation for a channel consisting of 2048 segments of a = 3.5 nm length; the angle between neighboring segments was 15$^o$, resulting in a persistence length of 100 nm; the coupling constant was 0.66 kHz and D = 2 µm$^2$/ms. Thick dashed line: Simulation for the corresponding channel of 64 effective segments of $a_{eff}$ = 32 x 3.5 nm = 112 nm length each. A spectral splitting is observed in (a) because the

averaged frequency of this relatively short channel is significantly different from zero.

The averaged frequencies along the chain have a random Gaussian distribution (according to the central limit theorem), with a standard deviation $\sigma \approx \bar{\delta}_Q/(a_{eff}/L_p)^{1/2}$, where the quantity under the square root is the number of persistence lengths in the effective segment. We ran simulations to confirm that scrambling the sequence of these random frequencies does not change the $^2$H spectrum or $T_2$ relaxation significantly.

**Simulation results of diffusion of D$_2$O along a curved channel.** We have simulated the diffusion of D$_2$O along a long, randomly curved channel using the algorithm described above. We used a diffusion coefficient $D = (\lambda-\lambda_{bound})/\lambda \times D_w$, where $D_w = 2.3 \times 10^{-5}$ cm$^2$/s = 2.3 $\mu$m$^2$/ms is the self-diffusion coefficient of liquid water at 295 K. Note that this coefficient of linear diffusion along the channel is larger than the coefficient of diffusion in three-dimensions measured in Nafion by pulsed field gradient NMR. This is reasonable since linear diffusion produces smaller mean-square displacements than diffusion in three dimensions. (Nevertheless, in the most realistic simulations with lateral diffusion shown below, we used a more moderate 1.2 $\mu$m$^2$/ms.)
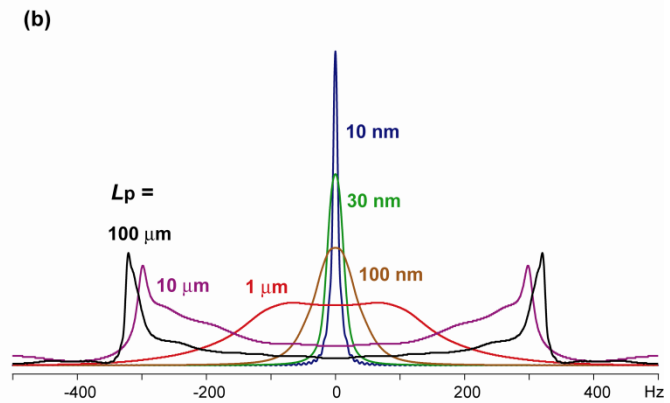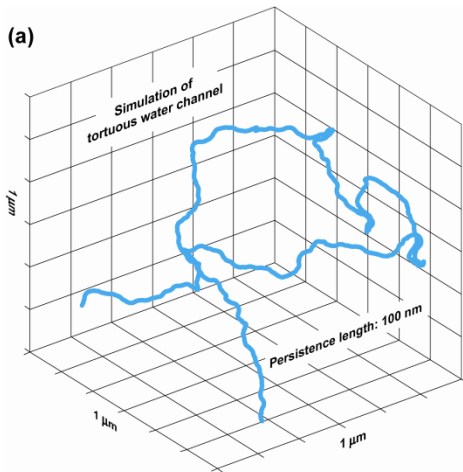
**Figure 4.6.** (a) Channel with freely-jointed segments with $15^{\circ}$ bond angle used in the NMR simulations. A channel with persistence length of 100 nm is shown. (b) Simulated $^2$H NMR spectra of $D_2O$ diffusing in channels of various persistence lengths. Intensities were scaled for clarity. The rigid limit splitting was 0.74 kHz and an averaged $D_2O$ diffusion coefficient of 1.9 $\mu m^2$/ms was used.

The line width may be dominated by effects of residual orientation. Therefore, the $T_2$ relaxation time provides a more stringent measure of the persistence length. Figure 4.7 shows the dependence of $T_2$ and line width$^{-1}$ on the persistence length, in a log-log plot. As expected, the linewidth decreases with decreasing persistence length, due to motional averaging by diffusion. The $T_2$ curve shows the expected minimum when $L_p$ is comparable to the diffusion length of $D_2O$ on the NMR time scale.
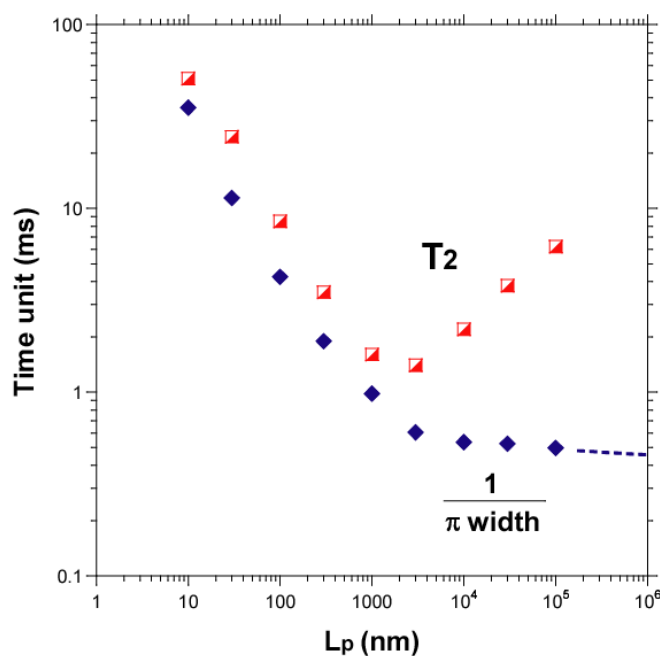


**Figure 4.7.** Dependence of simulated $^2$H NMR $T_2$ and inverse line width (or inverse splitting width) for diffusion along a curved channel (without lateral diffusion) on the persistence length, in a log-log plot. The rigid limit splitting was 0.74 kHz and an averaged $D_2O$ diffusion coefficient of 1.9 $\mu m^2$/ms was used.

The $T_2$ minimum is observed at a persistence length of around 3 μm, which is close to the diffusion length of $D_2O$ on the $^2H$ NMR time scale of 1 ms.

**Diameter variation along the channel.** A distribution in (i.e., significant range of) channel diameters, between 1.9 and 3.5 nm for $\lambda = 7$, was deduced from the smooth Porod region of the SAXS curves of Nafion [4]. Since wider channel segments have a larger fraction of free water, according to Eq. 4.23 below, this must result in a variation of the average $^2H$ quadrupolar frequency along the channel axis. Therefore, such a variation was included in our most realistic simulations. This variation is also indicated by the observed angle-dependence of the $T_2$ relaxation time for oriented samples. Without such a variation, $T_2$ for the 90° orientation is longer than for 60°, which can be understood in terms of the stronger variation of the quadrupolar frequency with angle (larger $|d\omega/d\theta|$) near 60°. In contrast, the magnitudes of the frequencies themselves are larger near 90°, and their variation due to varying $\delta_{ave}$ is therefore larger than at 60°.

In the simulations, the coupling constants $\overline{\delta}_Q$ were kept the same over segments of length $L_p$ (~ 40 nm), and varied randomly between 0.5 × and 1.5 × 0.66 kHz. This variation also produced additional fluctuations that reduced $T_2$ relaxation times. The difference between $T_2$ for 60° and 90° orientations can be increased by increasing the range of variation of $\overline{\delta}_Q$ or by increasing the length of constant-$\overline{\delta}_Q$ segments (towards the diffusion length of $D_2O$ on the NMR time scale, where relaxation effects are most pronounced). For different parameters that produced the same ratio of 60°- and 90°- $T_2$ values, the absolute values of $T_2$ were similar. The chosen three-fold variation in coupling strength on a length scale of $L_p$ seemed structurally most reasonable.

**Channel ends.** It is easy to incorporate channel ends, or slow links, into the exchange matrix, by reducing $\Pi_{n,n-1} = \Pi_{n-1,n}$ and adjusting $\Pi_{n,n} = \Pi_{n-1,n-1}$ to keep the column sum equal to zero. For a single channel without lateral diffusion, such slow links result in a pronounced increase in $T_2$ when the time needed to cross a slow link is longer than the time required for diffusion between slow links; then, the $H_2O$ molecule samples a limited set of frequencies, rather than

experiencing exchange with new frequencies and the resulting exchange broadening. However, this effect is canceled by the exchange by lateral diffusion discussed in the following, which makes other frequencies accessible and increases $T_2$ by a different mechanism.

**Lateral diffusion.** Curvilinear diffusion along the water channels is a fairly inefficient exchange process. Therefore, even relatively slow lateral diffusion between channels with different orientations can speed up the exchange process quite significantly and increase $T_2$. If channels merge with a neighbor on a length scale $L_{lat}$, motion of $D_2O$ by $L_{lat}$ along the channel results in a lateral displacement of d, the "long period" obtained from the position of the ionomer peak diffusion, both within a time $t_{lat}$. Thus,

$$2 \, D_{lat} \, t_{lat} = d^2 \tag{4.15a}$$
$$2 \, D \, t_{lat} = L_{lat}^2 \tag{4.15b}$$

which yields

$$D_{lat} = D \, d^2 / L_{lat}^2 \tag{4.16}$$

We assume that

$$L_{lat} \approx L_p, \tag{4.17}$$

the length scale on which the channel bundle becomes non-ideal. With $L_{lat} \approx L_p \approx 50$ nm and $d \approx 4.5$ nm, our model predicts that lateral diffusion is two orders of magnitude slower than the longitudinal diffusion. Nevertheless, it significantly speeds up the exchange process.

In addition to the lateral diffusion coefficient, we need the lateral diffusion distance from one bundle to another. Figure 4.8a demonstrates that the bundle diameter, i.e. the correlation length over which the channel directions are significantly correlated, must be of the order of the persistence length $L_p$; if it was larger, different parts of a bundle would

sterically interfere with each other, as indicated in Figure 4.8a. Next, we determine the longitudinal diffusion length $L_{long,lat}$ that results in lateral diffusion by $L_p$, within the same time $t_{long,lat}$

$$2\,D\,t_{long,lat} = L_{long,lat}^2 \tag{4.18a}$$
$$2\,D_{lat}\,t_{long,lat} = L_p^2 \tag{4.18b}$$

This requires

$$L_{long,lat}^2 = D\,/\,D_{lat} \times L_p^2 = L_p^4\,/\,d^2 \tag{4.19a}$$
$$L_{long,lat} = L_p^2\,/\,d \tag{4.19b}$$

We approximated the effect of the lateral loss of correlation within a bundle of length $L_{long,lat}$ as a two-fold reduction in average frequency, and generally as a scaling of $\bar{\delta}_Q$ by $0.5$ ^ ($a_{eff}$/ $L_{long,lat}$)

After laterally diffusing by a few $L_p$, a water molecule will reach a significantly differently oriented bundle of channels. We simulated this lateral exchange process in terms of exchange from effective segments, spaced by $2 \times L_{long,lat}$, to randomly chosen effective segments in the model channel. For $a_{eff} = L_{long,lat}$, the value of the exchange matrix element is equal to that for diffusion along the channel, and in general

$$W_{lat} = D_{lat}/L_p^2 = D/L_p^4 \times d^2 = W_{long}\,a_{eff}^2/L_p^4 \times d^2 \tag{4.20}$$

Given the many approximations and assumptions required, the persistence length cannot be determined with high accuracy. Nevertheless, the lateral diffusion parameters $L_{long,lat}$ and $W_{lat}$ depend so strongly on $L_p$ that the lateral diffusion rate decreases steeply with $L_p$ and fairly stringent upper and lower limits on $L_p$ can be obtained.
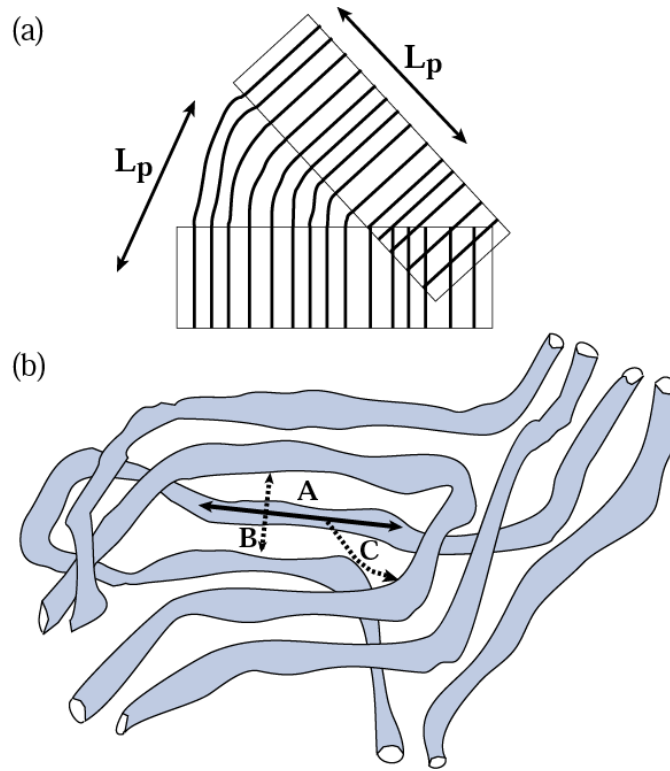
**Figure 4.8**. (a) Schematic demonstrating that the radius of a bundle of curved channels (shown as thick lines) in Nafion must be limited to a value close to $L_p$. The figure demonstrates that wider bundles would interfere with each other (overlap at the lower right) (b) Schematic indicating diffusion along a channel (A), perpendicular to a channel within a bundle (B), and between differently oriented bundles (C). The channel diameter is exaggerated relative to the persistence length.

**Drawn-sample simulations.** In order to simulate the spectra of $D_2O$ in drawn Nafion, the channel was deformed affinely by transforming every link at (x, y, z) to (x', y', z') according to

$$z' = DR\ z, \qquad x' = 1/DR^{1/2}\ x, \qquad y' = 1/DR^{1/2}\ y \qquad\qquad (4.21)$$

This affine deformation is sketched in Figure 4.9.
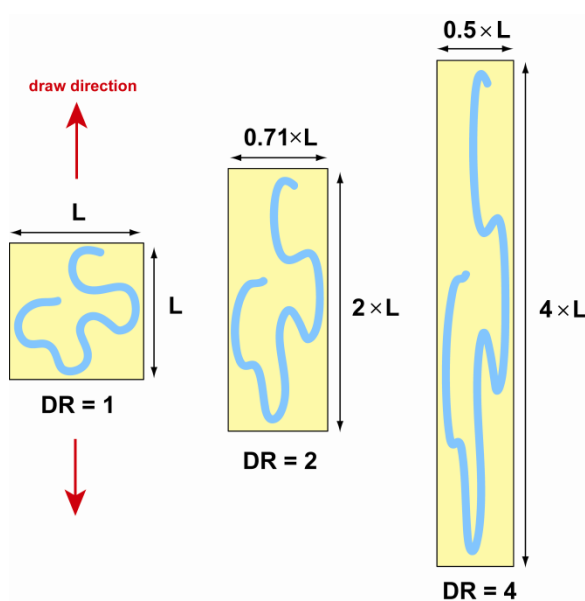
**Figure 4.9**. Schematic illustration of uniaxial drawing of stretching Nafion. When the draw ratio increases, the channels become straighter, but the turn-backs still restrict diffusion along the draw direction. SAXS indicates that at higher draw ratios, the channel diameters also shrink. As the channels become extended, the separation between sulfonic acid groups increases and so does $\lambda^{bound}$.

## Results and Discussion

**²H NMR spectra of drawn Nafion.** The ²H NMR spectra of $D_2O$ in drawn Nafion in Figures 4.2a and b show the behavior expected from the channel model. The observed ²H splitting is orientation dependent as expected for a uniaxial system,

$$\omega_Q(\theta) = \frac{1}{2}\bar{\delta}_Q(3\cos^2\theta - 1)$$

(4.22)

where $\theta$ is the angle between the draw direction and the applied field $B_0$. As expected, the size of the splitting for the parallel orientation increases with draw ratio, see Figure 4.10. The quadrupolar coupling in an infinite long channel perfectly oriented along the external field may be estimated by extrapolating the linear fit in Figure 4.10b. The limit is at ~ 1200 Hz. However, we will show below, based on $T_1$ relaxation times, that some deformation of the

channel also occurs with drawing that increases the coupling strength relative to that in the undrawn sample.
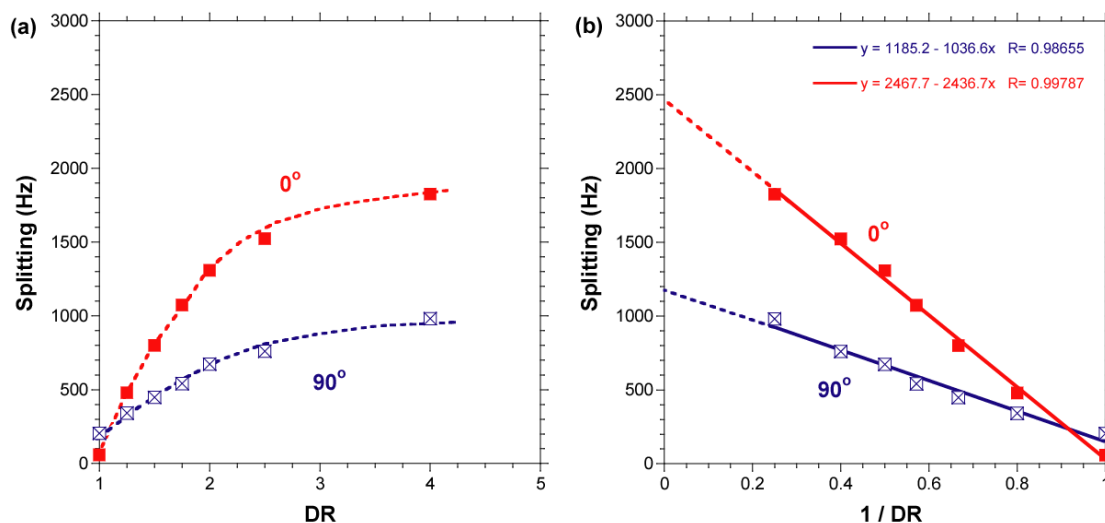


**Figure 4.10.** (a) $^2$H splitting vs. draw ratio DR and (b) $^2$H splitting vs. 1/DR for parallel and perpendicular orientations ($\lambda = 7$, prepared via Method I). The lines are guides to the eye.

**$^2$H NMR spectrum of undrawn Nafion.** The $^2$H spectrum of undrawn Nafion displayed in Figure 4.2d shows dramatic additional narrowing, compared with that of "powdered" drawn Nafion shown in Figure 4.2c. This shows a second motional process narrows the spectrum in undrawn Nafion further. We identify this as diffusion of $D_2O$ along a channel that is strongly curved on the length scale of $D_2O$ diffusion, $\sim 2$ μm, on the NMR time scale of $\sim 2$ ms. In other words, the persistence length must be $\ll 2$ μm.

In order to evaluate this more quantitatively, we need to simulate the $^2$H spectrum of diffusing $D_2O$. This requires an estimate the $^2$H coupling strength, $\bar{\delta}_Q$, in the undrawn sample. The value in the drawn sample is a first approximation, but it is conceivable that it is increased by structural changes during drawing. We can characterize these changes by analyzing $T_1$ relaxation as a function of draw ratio and hydration.

**Hydration-dependence of $^2$H NMR observables.** Figures 4.11 and 4.12 show the dependence of the $T_1$ relaxation time and $^2$H NMR splitting on the hydration level, quantified in terms of the number $\lambda$ of water molecules per sulfonate group.

The observed hydration-dependence of the $T_1$ relaxation time and $^2$H NMR splitting can be explained in terms of exchange between a fixed amount, $\lambda_{bound}$, of bound water and free water whose amount increases with $\lambda$, within a cylindrical segment. This analysis of $\lambda_{bound}$ in drawn and undeformed samples provides the basis for a good estimate of $\bar{\delta}_Q$ in undrawn samples.

In a simplified model, the $D_2O$ in Nafion channels can be viewed as consisting of two different types. The $D_2O$ molecules next to the channel wall have relatively large quadrupolar couplings due to stronger interactions with $-SO_3$ side groups; these $D_2O$ molecules may be termed bound $D_2O$. The rest, near the center of the channel, have $^2$H quadrupolar couplings approaching zero because of their fast tumbling; these $D_2O$ molecules may be considered as free $D_2O$. These two $D_2O$ species exchange with each other on a short time scale, which results in an averaged quadrupolar coupling that we can observe by $^2$H NMR. The averaging can be expressed as follows:

$$\bar{\delta}_Q = \delta_Q^{bound} \times f^{bound} + \delta_Q^{free} \times f^{free} \tag{4.23}$$

with

$$f^{bound} = 1 - f^{free} = \lambda^{bound}/\lambda \tag{4.24}$$

Isotropic tumbling of the free water results in $\delta_Q^{free} \approx 0$ Hz as for bulk $D_2O$, so the above equation simplifies to

$$\bar{\delta}_Q = \delta_Q^{bound} \times \lambda^{bound}/\lambda \tag{4.25}$$
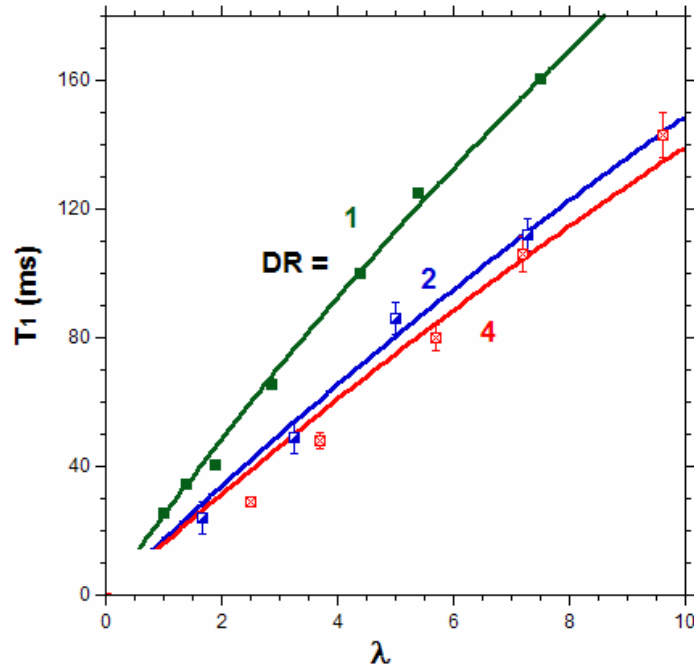
**Figure 4.11**. $T_1$ relaxation time vs. hydration for drawn Nafion with draw axis parallel to $B_0$ (prepared via Method III).

Similarly, $T_1$ relaxation can be described by

$$\frac{1}{T_1} = \frac{1}{T_1^{bound}} \times f^{bound} + \frac{1}{T_1^{free}} \times f^{free} \qquad (26)$$

The $T_1$ values are chosen to be $T_1^{bound}$ = 10 ms for bound $D_2O$ and $T_1^{free}$ = 1 s for free $D_2O$. Since $1/T_1^{bound} \gg 1/ T_1^{free}$, we have approximately a linear dependence on $\lambda$:

$$T_1 \approx \lambda/\lambda^{bound} \; T_1^{bound} \qquad (27)$$

From the fits in Figure 4.12, $\lambda^{bound}$ = 0.62 in drawn Nafion with DR = 4, $\lambda^{bound}$ = 0.58 in drawn Nafion with DR = 2, and $\lambda^{bound}$ = 0.40 in drawn Nafion with DR = 1.
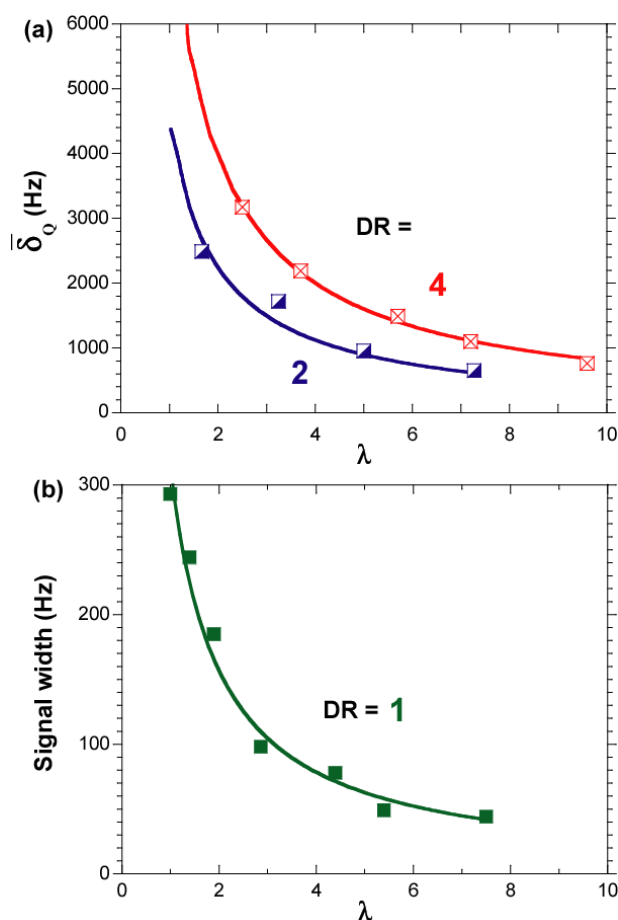
**Figure 4.12**. $^2$H NMR quadrupolar splitting or signal width vs. hydration level for (a) DR = 2 and 4 and (b) DR = 1. For each draw ratio, the points are fitted to the equation $\bar{\delta}_Q \times \lambda$ = constant.

The $^2$H splitting is fitted by Eq. 4.25, with $\bar{\delta}_Q \times \lambda \approx 8$ kHz for drawn Nafion DR = 4. Using $\lambda^{bound} = 0.62$ as determined above, $\delta_Q^{bound} = 8$ kHz/0.62 = 12.9 kHz if the channels for DR = 4 are assumed to be straight. The fit for drawn Nafion with DR = 2 gave $\bar{\delta}_Q \times \lambda \approx 4.8$ kHz. With $\lambda^{bound} = 0.58$, the apparent $\delta_Q^{bound}$ is around 8.3 kHz. The reduced value is attributed to the residual undulation of the water channels in the DR = 2 sample. Fitting the line widths $W_Q$ of normal Nafion, with DR = 1, gave $W_Q \times \lambda \approx 0.31$ kHz. The value of $W_Q \times \lambda$ is strongly reduced compared to that for DR = 4, due to D$_2$O diffusion through curved water channels that generates additional motional averaging of the observed $^2$H splitting. By

evaluating the narrowing of $^2$H splitting due to $D_2O$ diffusion, the curvature of water channels can be quantified.
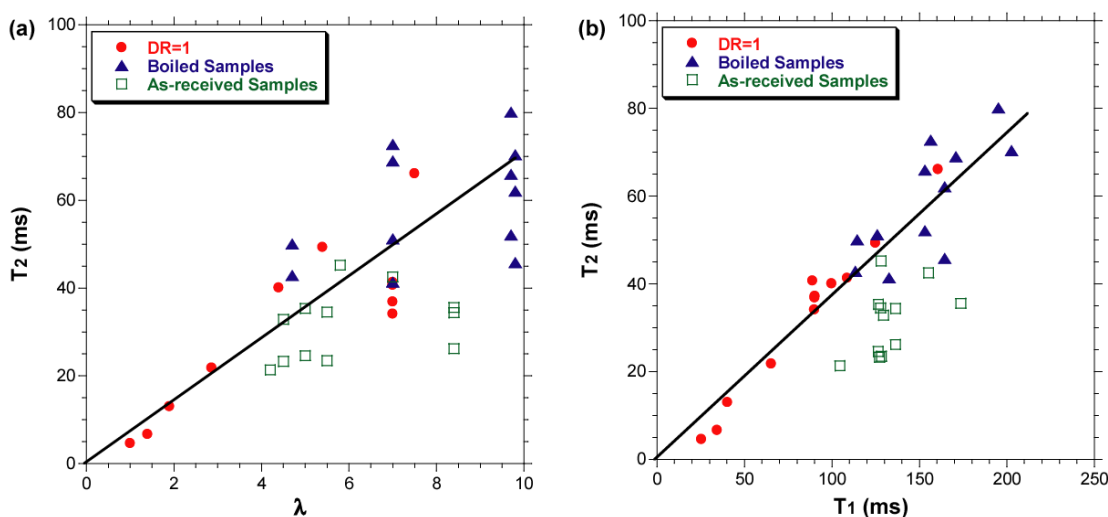


**Figure 4.13.** (a) $T_2$ vs hydration level plot for un-drawn samples. (b) $T_2$ vs $T_1$ plot for un-drawn samples (all preparation methods are included). The lines are guides to the eye, disregarding the data from the as-received samples (open squares).

Figure 4.13 shows the increase of $T_2$ with hydration, and the correlation between $T_2$ and $T_1$. The $T_2$ values of as-received samples (open squares) are below the trend line of the samples pretreated by boiling. Possibly, the $T_2$ relaxation times are shortened due to the presence of paramagnetic ions that are washed out during the boiling process. Due to the uncertainty of hydration level obtained from weight measurement and the possible inconsistency between samples, the variation in the $T_2$ vs. hydration level plot, Figure 4.13a, is rather large. The variation is reduced in the $T_2$ vs $T_1$ plot, in which the error generated by weight measurement is irrelevant. Thus, it may be more reliable to determine the hydration level via $T_1$ or $T_2$ relaxation time for samples prepared under the same conditions.

**Persistence length of channels in Nafion.** Figure 4.14 shows the simulated dependence of $^2$H NMR $T_2$ relaxation times on the persistence length of the water channel in our most realistic (and complex) model, for hydration of $\lambda = 7$. $T_2$ rather than spectral line width was evaluated quantitatively since it is insensitive to slight preferential orientations of channels,

while such anisotropy results in residual quadrupolar splittings in $^2$H NMR spectra that dominate over the line width due to diffusion that is of interest here.

Along the lines of Figure 4.8b, the model included diffusion along a channel of varying diameter, as well as diffusion inside the bundle and diffusion between bundles; these latter two features were approximated as described in the theory section, by a two-fold reduced coupling constant for an effective segment of length $L_p$ and by additional off-diagonal elements in the exchange matrix, respectively. The parameters used were chosen to be close to the center of their expected range, in particular the averaged coupling $\bar{\delta}_Q = 0.85$ kHz in a straight channel segment and the diffusion coefficient $D = 1.2$ $\mu m^2/ms$ (twice smaller than in bulk water) for diffusion along a channel.

As expected from the strong dependence of lateral diffusion on $L_p$ (see Eq. 4.20), the $T_2$ relaxation time in Figure 4.14 changes dramatically with $L_p$. According to Figure 4.13, the measured $T_2$ of between 30 and 70 ms at $\lambda = 7$ corresponds to a persistence length of $L_p \approx 40$ nm in the simulation. Given the approximations for the lateral diffusion in the simulation, a range of $25 - 80$ nm must be considered possible. Note that a persistence length shorter than 25 nm (ten times the average channel diameter) would also be inconsistent with the small-angle upturn in SAXS. At lower hydration levels, the increased coupling strength $\bar{\delta}_Q \sim 1/\lambda$ and decreased diffusion coefficient $D$ will result in reduced $T_2$ relaxation times ($\sim 1/\lambda$), as observed experimentally.

Our analysis shows that a picture of straight channels extending across a membrane of $> 100$ $\mu m$ thickness [9] is not correct. The orientation dependence of the small quadrupolar splitting of $D_2O$ in commercial Nafion membranes is not due to parallel orientation of all channels [9], but due to a slight anisotropy in the nearly isotropic orientation distribution of channel segments.
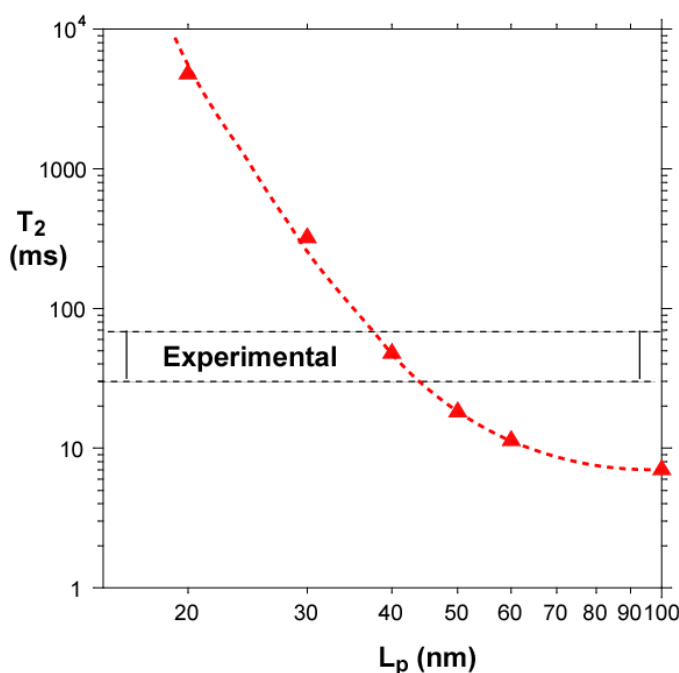
**Figure 4.14.** $^2$H $T_2$ relaxation times vs. persistence length $L_p$ for $\lambda = 7$, obtained from our most detailed simulation of $D_2O$ diffusing along a channel of $> 80$ μm length and also undergoing lateral diffusion, with $\bar{\delta}_Q = 0.85$ kHz in a straight channel segment and $D = 1.2$ μm$^2$/ms along the channel. The dashed line through the simulated points is a guide to the eye. The corresponding range of experimental values of the $T_2$ relaxation time for $\lambda = 7$ is indicated on the vertical axis.

**Conclusions**

We have investigated the persistence length (straightness) of the water channels in Nafion fuel cell membranes. $^2$H NMR of $D_2O$ diffusing in the channels of undrawn Nafion showed motional narrowing by an order of magnitude compared to the splitting in the straightened channels of drawn Nafion. This was attributed to diffusion along channels strongly curved within the ~1 μm length of diffusion on the NMR time scale. $T_1$ relaxation was investigated to estimate the coupling strength in a straight channel segment. A simple model of bound and free water accounted for the observed hydration dependence of the spectral splittings and relaxation times. The spectra and $T_2$ relaxation times were simulated in terms of diffusion-induced exchange between segments along a curved channel. In order to simulate sufficiently long channels (~ 100 μm), we developed an algorithm that lumped segments subject to fast

frequency averaging by diffusion into an effective segment. Lateral diffusion between bundles was found to speed up exchange significantly and was therefore incorporated into the most realistic simulations, as were fluctuations in channel diameter on the scale of the persistence length. The simulated $T_2$ matched the experimental value for a persistence length of $L_p = 40$ nm, but due to approximations made in the simulations, a range of $L_p$ between 25 and 80 nm must be considered possible. In other words, the channels are "perfect", i.e. quite straight and not merged with neighbors, only on a length scale of a few tens of nanometers. This is at the lower end of the value suggested by small-angle scattering data.

## Acknowledgements

## References

(1)     Kreuer, K. D.; Paddison, S. J.; Spohr, E.; Schuster, M. *Chem. Rev.* **2004**, *104*, 4637-4678.

(2)     Mauritz, K. A.; Moore, R. B. *Chem. Rev.* **2004**, *104*, 4535-4585.

(3)     Devanathan, R. *Energy Environ. Sci.* **2008**, *1*, 101-119.

(4)     Schmidt-Rohr, K.; Chen, Q. *Nat. Mater.* **2008**, *7*, 75-83.

(5)     Chen, Q.; Schmidt-Rohr, K. *Macromolecules* **2004**, *37*, 5995-6003.

(6)     Chen, Q.; Schmidt-Rohr, K. *Macromol. Chem. Phys.* **2007**, *208*, 2189-2203.

(7)     Gebel, G. *Polymer* **2000**, *41*, 5829-5838.

(8)     Rubatat, L.; Rollet, A. L.; Gebel, G.; Diat, O. *Macromolecules* **2002**, *35*, 4050-4055.

(9)     Li, J.; Wilmsmeyer, K. G.; Madsen, L. A. *Macromolecules* **2009**, *42*, 255-262.

(10)    Page, K. A.; Landis, F. A.; Phillips, A. K.; Moore, R. B. *Macromolecules* **2006**, *39*, 3939-3946.

(11)    Osborn, S. J.; Hassan, M. K.; Divoux, G. M.; Rhoades, D. W.; Mauritz, K. A.; Moore, R. B. *Macromolecules* **2007**, *40*, 3886-3890.

(12)     Zawodzinski, T. A.; Springer, T. E.; Davey, J.; Jestel, R.; Lopez, C.; Valerio, J.; Gottesfeld, S. *J. Electrochem. Soc.* **1993**, *140*, 1981-1985.

(13)     Abragam, A. *Principles of Nuclear Magnetism* Oxford University Press **1961**.

# Chapter 5

# Determination of the Structure of a Novel Anion Exchange Fuel Cell Membrane by Solid-State Nuclear Magnetic Resonance Spectroscopy

Xueqian Kong, Kuldeep Wadhwa, John G. Verkade, Klaus Schmidt-Rohr

## Abstract

A novel anion exchange fuel cell membrane was successfully synthesized by chemically attaching proazaphosphatranium/phosphatranium cations under microwave treatment to the sulfonic groups of Nafion-F. Solid-state nuclear magnetic resonance (NMR) techniques were employed to determine the actual structure and composition of this anion exchange membrane. $^{31}$P NMR showed two main signals with a 2:1 intensity ratio and chemical shift changes of +89 ppm and +46 ppm, respectively, from the main peak of phosphatranium chloride. $^{1}$H–$^{31}$P heteronuclear correlation (HetCor) NMR and $^{1}$H–$^{31}$P recoupling experiments indicated that the proton originally bonded to phosphorus in phosphatranium chloride is replaced in the major component of the Nafion–proazaphosphatranium/phosphatranium composite. $^{19}$F NMR experiments showed that the fluorine in the –SO$_2$F group of the Nafion-F precursor is fully replaced. $^{31}$P{$^{19}$F} rotational-echo double resonance (REDOR) experiments measured a P–F internuclear distance of ~0.4 nm, which showed that the proazaphosphatranium is covalently attached to Nafion through a S–P bond. $^{13}$C NMR and $^{1}$H–$^{13}$C HetCor spectra indicated that the proazaphosphatranium structure is maintained even after the microwave treatment at 180 $^{\text{o}}$C and also showed the presence of entrapped dimethylformamide solvent.

## Introduction

The increasing demand for alternative sources of energy[1-4] has placed direct methanol-based fuel cells (DMFCs) at the forefront of the search for alternatives to fossil fuels. DMFCs are projected to be the first fuel cells that will be commercially available for use by the general population. Among the advantages of DMFCs are their high energy density (5–10 times greater than that of commonly available batteries), moderate operating temperatures, and easy replacement of the methanol fuel cartridge; all of which make DMFCs ideal for usage in portable electronic devices.[5-7] In many modern fuel cells, a proton exchange membrane (PEM) is utilized to transport protons produced in the anodic half reaction for consumption on the cathodic side of the cell (Scheme 5.1a). However, PEMs in DMFCs suffer from (i) parasitic crossover of methanol, which leads to a lowering of cell voltage and efficiency; (ii) electro-osmosis of water from anode to cathode, which causes severe flooding at the cathode; and (iii) reduced catalyst kinetics in the acidic environment requiring high loadings of costly precious-metal catalysts, e.g. platinum.[8] For these reasons, alkaline fuel cells (AFCs) with the same net reaction but exploiting different half reactions as shown in Scheme 5.1b have become attractive to investigate. The most important advantages of AFCs are that they can operate at a lower catalyst loading owing to more facile methanol oxidation in alkaline media,[9-11] and that they may utilize a broader range of catalysts, such as nickel and silver.[12-14]

(a)

Anode: $CH_3OH + H_2O \rightarrow CO_2 + 6\,e^- + 6\,H^+$

Cathode: $3/2\,O_2 + 6\,H^+ + 6\,e^- \rightarrow 3\,H_2O$

Net: $CH_3OH + 3/2\,O_2 \rightarrow CO_2 + 2\,H_2O$

(b)

Anode: $CH_3OH + 6\,OH^- \rightarrow CO_2 + 5\,H_2O + 6\,e^-$

Cathode: $3/2\,O_2 + 3\,H_2O + 6\,e^- \rightarrow 6\,OH^-$

Net: $CH_3OH + 3/2\,O_2 \rightarrow CO_2 + 2\,H_2O$
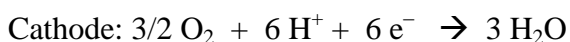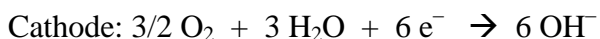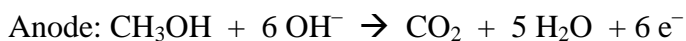
**Scheme 5.1:** Half-reactions and the overall net reaction in a methanol fuel cell. (a) Protonic half reactions in a conventional fuel cell. (b) Reactions in an alkaline fuel cell.

In the past, methanol was not suitable as a fuel in AFCs because such cells utilized liquid alkaline electrolytes such as hydroxide ion conductors, which are vulnerable to precipitation of carbonate (e.g. $K_2CO_3$) that destroys the catalyst layer, which forms from $CO_2$ released in the cell reaction (Scheme 5.1b).[15-17] As a result, solid alkaline anion exchange membranes (AAEMs) containing hydroxide ions were developed. They combine the advantages of PEMs (flexibility, durability, small volume, and no leakage) and traditional AFCs (good catalyst kinetics) and they can operate when carbonate species are present.[8] Some efforts have been made to use fluorinated polymers as AAEMs. For example, poly(vinylidene fluoride) (PVDF) and poly(tetrafluoroethene-co-hexafluoropropylene) (FEP) have been grafted with 4-vinylbenzyl chloride, followed by modification of the benzyl chloride functionality with trimethylamine to give the trimethylbenzyl ammonium salt, which was then tested as an AAEM.[18] While the FEP-based AAEM gave conductivities of ca. 0.02 S/cm at ambient temperature and an atmospheric relative humidity of 100%, the PVDF-based AAEM degraded on subsequent amination and hydroxide ion exchange.
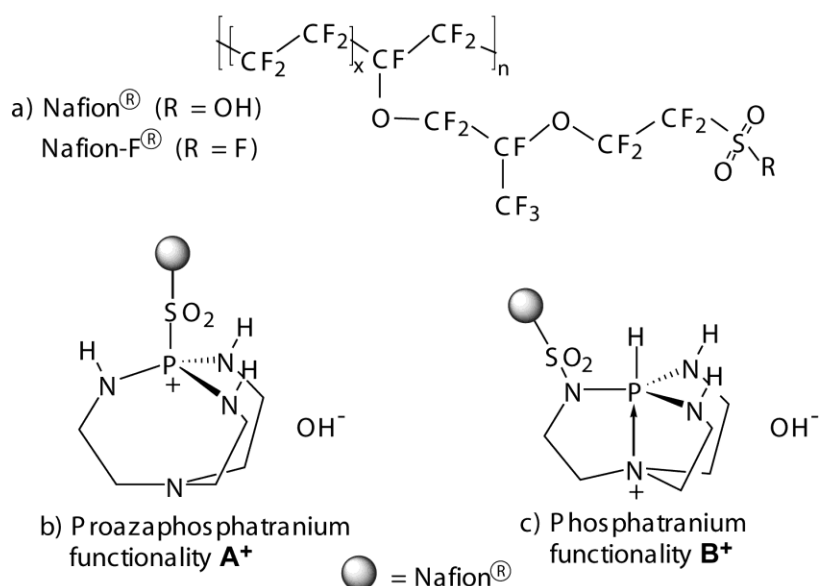


**Scheme 5.2.** a) Representation of the average chemical structure of Nafion® and Nafion-F®. b) Representation of Nafion® polymer segments attached to proazaphosphatranium functional groups $A^+$. c) Representation of the same Nafion® polymer segments bonded to phosphatranium functional groups $B^+$.

An important feature of AAEMs is that their conductivities are directly proportional to the ionophore densities. Commonly studied ionophores tethered to AAEM backbones are quaternary ammonium salts. However, these salts experience relatively intense cation–anion interactions, which further impede hydroxide ion mobility. Here we report the synthesis and characterization of a potentially improved AAEM that incorporates novel types of phosphonium cations as depicted in Scheme 5.2b and 5.2c. These ionophores have a reduced charge density due to their resonance structures that distribute the positive charge (Scheme 5.3) and thus diminish ionic interaction, which should facilitate hydroxide ion mobility.

These phosphonium sidegroups have been attached to Nafion® (Scheme 5.2a), a tetrafluoroethylene copolymer bearing sulfonic acid (-$SO_2OH$) functional groups which is extensively used as a PEM in fuel cells. Being perfluorinated and semicrystalline, Nafion® (a proton cation conductor commercially-derived via base hydrolysis of Nafion-F®) and its precursor, Nafion-F® (which contains -$SO_2F$ functionalities), possess good thermal and mechanical stability, which are particular advantages of Nafion® compared with many other potential PEM materials. Nafion® is stable up to 300 °C.[19] Its excellent conductivity stems from its combination of a hydrophobic polymer backbone and hydrophilic functional groups which self-organize to form water channels of ~2.5-nm diameter through which small ions can be easily transported.[20]
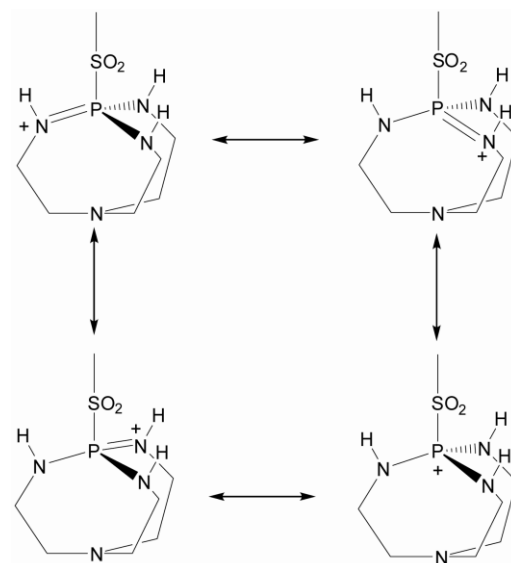


**Scheme 5.3**: Resonance structures for a proazaphosphatranium cation.

The synthesis steps for our material are summarized in Scheme 5.4, wherein Phan denotes the incorporation into the Nafion® (Naf) polymer of the two structurally different types of phosphorus cations [i.e., proazaphosphatranium ($\mathbf{A}^+$ in Scheme 5.2) and phosphatranium ($\mathbf{B}^+$ in Scheme 5.2)] and "X" designates the anions Cl⁻ or F⁻. Solid state nuclear magnetic resonance (NMR) is a promising tool for assessing the relative levels of $\mathbf{A}^+$, $\mathbf{B}^+$ or other functionalities incorporated, and for detailing their chemical structure, since the material is rich in NMR-active spin-1/2 isotopes, namely $^1$H, $^{13}$C, $^{31}$P, $^{19}$F and $^{15}$N. The characteristic chemical shifts of the $^{31}$P, $^1$H, $^{19}$F, $^{13}$C and $^{15}$N in Naf-Phan-X were detected in quantitative direct polarization (DP) experiments (for $^{31}$P and $^{19}$F) and in cross polarization (CP) experiments (for $^{31}$P, $^{13}$C, and $^{15}$N). The potential bonding of the three latter isotopes to hydrogen was determined by recoupling the dipolar interaction with $^1$H. The correlations between phosphorus or carbon and their nearest protons were determined by 2D $^1$H–$^{31}$P and $^1$H–$^{13}$C heteronuclear correlation (HetCor) NMR. The bonding between Nafion® and proazaphosphatranium/phosphatranium moieties was elucidated using $^{31}$P{$^{19}$F} rotational echo double resonance (REDOR)[25]. $^{13}$C spectra were edited with CH and CH$_2$ selection sequences[33, 34] to identify such segments unambiguously.
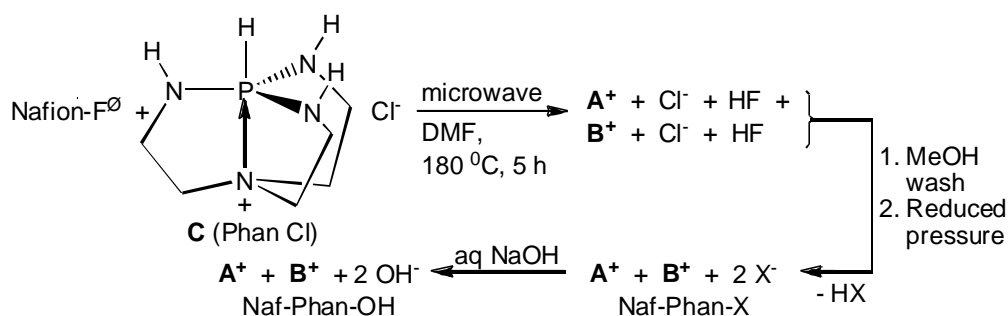


**Scheme 5.4**: Synthesis of Naf-Phan-X and Naf-Phan-OH.

**Experimental Section**

**Samples.** Nafion-F® membrane (6 cm x 6 cm), with a 0.9 mmol/g loading of SO$_2$F functionality and a thickness of 25 microns (a product of Du Pont supplied by Ion Power Inc.) was charged to a microwave vial. To this was added excess phosphatranium chloride (Phan-Cl in Scheme 5.4; 500 mg, 2.3 mmol) prepared according to a literature method[21] and dry

dimethyl formamide (ca 8 mL) such that the membrane was completely immersed in the solution. The mixture was microwaved at 180 $^{\circ}$C for 5 hours using a 300 watt CEM Discover apparatus and then the membrane was washed with copious amounts of methanol to remove any unreacted phosphatranium salt, HX and solvent. For solid state NMR characterization, the Naf-Phan-X membrane was dried at room temperature under reduced pressure. For electrical measurements (to be reported in due course) the Naf-Phan-X membrane was soaked in aq. NaOH to exchange the halide ions for hydroxide, giving Naf-Phan-OH in Scheme 5.4.  The change in counterion is unlikely to result in significant structural changes of the polymer or sidegroups.

**NMR parameters.** All NMR experiments were performed on a Bruker DSX-400 spectrometer at a resonance frequency of 400 MHz for $^{1}$H, 100 MHz for $^{13}$C, 162 MHz for $^{31}$P, 376 MHz for $^{19}$F and 40.5 MHz for $^{15}$N, using double-resonance or triple-resonance magic-angle spinning (MAS) probes. $^{13}$C experiments were performed in 7-mm rotors at 6.5 kHz with 90$^{\circ}$ pulse lengths of 4 μs and 3-s recycle delays; $^{31}$P experiments in 4-mm rotors at 7 kHz with 90$^{\circ}$ pulse lengths of 4 μs and either 2-s recycle delay for cross polarization or 100 s for direct polarization; and$^{19}$F experiments in 2.5-mm rotors at 30 kHz, which reduces $^{19}$F dipolar couplings enough to resolve various sidegroup- and backbone signals in Nafion, with 90$^{\circ}$ pulse lengths of 1.85 μs and 3-s recycle delays. $^{15}$N experiments were performed in 7-mm rotors at 5 kHz with 90$^{\circ}$ pulse lengths of 9.2 μs and 2.5-s recycle delays; the number of scans was 6,144 for phosphatranium chloride and 28,672 for Naf-Phan-X.  Two-pulse phase-modulation (TPPM) was used for $^{1}$H–$^{13}$C, $^{1}$H–$^{31}$P, or $^{1}$H–$^{15}$N heteronuclear dipolar decoupling. $^{31}$P and $^{15}$N chemical shifts were indirectly referenced to $H_3PO_4$ and liquid $NH_3$, respectively, using hydroxyapatite ($^{31}$P chemical shift at +3 ppm) and N-acetyl valine ($^{15}$N chemical shift at +122 ppm). All experiments were carried out at ambient temperature.

*$^{1}$H–$^{31}$P and $^{1}$H–$^{13}$C HetCor.* Two-dimensional (2D) $^{1}$H–$^{31}$P and $^{1}$H–$^{13}$C heteronuclear correlation (HetCor) NMR experiments[22,23] were performed at spinning frequencies of 7 kHz and 6.5 kHz, respectively. Frequency-switched Lee-Goldburg[24] homonuclear decoupling was applied during the evolution period t$_1$. Lee-Goldburg cross polarization was used to suppress

$^1$H–$^1$H spin diffusion during polarization transfer and to show mostly one- and two-bond $^1$H–$^{13}$C connectivities. For $^1$H–$^{31}$P HetCor, the cross polarization time was 0.7 ms, the number of scans was 128, and the number of $t_1$ increments was 100. For $^1$H–$^{13}$C HetCor, the cross polarization time was 0.2 ms, the number of scans was 128, and the number of $t_1$ increments was 72.

*$^{31}$P{$^{19}$F} REDOR.* $^{31}$P{$^{19}$F} REDOR experiments[25] were performed in 2.5-mm rotors at a spinning frequency of 30 kHz, which avoids excessive dephasing losses and allows semi-quantitative $^{31}$P{$^{19}$F} distance measurements. The dephasing of $^{31}$P magnetization in the field of the $^{19}$F spins was observed. $^{19}$F composite 90$^o$x-180$^o$y-90$^o$x pulses of 7.6-μs duration were applied with pulse centers spaced by $t_r$/2 during a period of N$t_r$ in order to recouple the dipolar interaction between $^{31}$P and $^{19}$F. EXORCYCLE was used for the single 180$^o$ pulse on the $^{31}$P channel.[26] The recoupling $^{19}$F pulses were turned off to obtain the reference signal $S_0$.

## Results and Discussion

**$^{31}$P NMR: chemical bonding of phosphorus.** The $^{31}$P MAS NMR spectra (Figure 5.1a, b) of phosphatranium chloride (Phan-Cl) show a dominant centerband at an isotropic chemical shift of –48 ppm with spinning sidebands (labeled with asterisks) spaced by the spinning frequency $\omega_r$. The signal was quickly dephased by the H–P dipolar coupling during gated recoupling, see Figure 5.1c, as expected for a P-H group ("protonated phosphorus"). The $^{31}$P chemical shift is close to the value of –43 ppm for the phosphatranium ion in solution as reported in the literature.[27] Peaks at 0 ppm and +41 ppm must be assigned to impurities or more likely degradation products due to decomposition of Phan-Cl in the presence of water; these peaks do not appear in solution spectra of fresh Phan-Cl in organic solvents.[27] In the spectra of the product Naf-Phan-X (Figure 5.1d, e), two major peaks at +41 ppm and ~ +5 ppm are observed, with an area ratio of 2:1 in the quantitative DP spectrum. The peak at 41 ppm is associated with a non-protonated phosphorus as indicated by slow CP and slow dephasing by gated recoupling (see Figure 5.1f). The peak near 5 ppm consists of two components (which are confirmed by $^1$H-$^{13}$C correlation below): (i) a broader band centered at 3 ppm, with significant spinning sidebands, and fast H-P dephasing indicative of P bonded

to H, and (ii) the peak at 5 ppm, which shows slower H-P dephasing that may suggest a phosphorus close to a proton but with a smaller H–P dipolar coupling due to a larger internuclear distance or motional averaging. The peak at 41 ppm is assigned to Naf-Phan-X of functionality $\mathbf{A^+}$. This assignment is proven below using $^1$H-$^{31}$P HetCor spectra, and further supported by chemical-shift analysis. The peaks at ~5 ppm can be tentatively assigned to the $\mathbf{B^+}$ functionality; the ~3-ppm variation in chemical shifts might be due to different hydrogen bonding. According to the peak areas in the quantitative $^{31}$P NMR spectrum, the Naf-Phan-X functionality $\mathbf{A^+}$ accounts for 67% of the total phosphorus content in our sample.
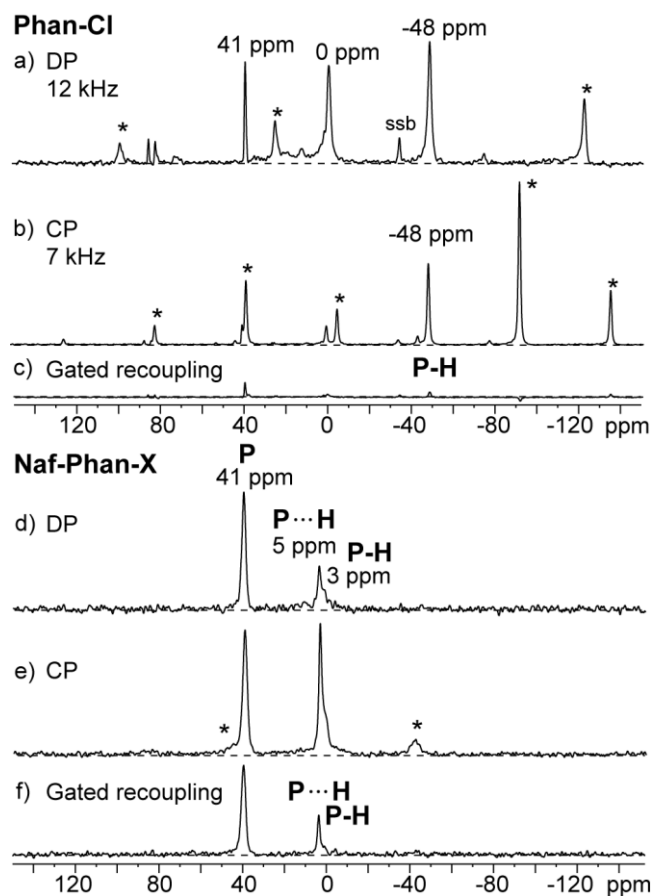


**Figure 5.1.** $^{31}$P spectra of phosphatranium chloride (Phan-Cl, a - c) and Naf-Phan-X membrane (d - f). For Phan-Cl, a) direct polarization (DP) at $\nu_r = 12$ kHz with a recycle delay of 100 s and b) $^1$H–$^{31}$P cross polarization (CP) at $\nu_r = 7$ kHz with a recycle delay of 100 s show the centerband of the main $^{31}$P signal with an isotropic chemical shift of −

48 ppm; its spinning sidebands are labeled with asterisks. A sideband of the +41-ppm peak is labeled "ssb". c) CP spectrum after gated recoupling for one rotation period, which confirms that the peak at −48 ppm is the signal of a protonated phosphorus. For the Naf-Phan-X membrane, the DP spectrum d) at $\nu_r$ = 12 kHz with a recycle delay of 100 s, shows two resolved $^{31}$P peaks (at 41 ppm and ~5 ppm) with an area ratio of 2:1. e) CP spectrum at $\nu_r$ = 7 kHz. Sidebands of the shoulder at 3 ppm are labeled by asterisks. f) CP spectrum after gated recoupling for one rotation period.

In order to identify $^1$H near phosphorus, two-dimensional $^1$H–$^{31}$P HetCor experiments (Figure 5.2) were performed with mixing times of 0.05 ms (nearest $^1$H) and 50 ms ($^1$H within ~3 nm). For phosphatranium chloride, the proton bonded to the phosphorus resonates at 5.6 ppm,[28] which is shown by the stronger cross peak to the $^{31}$P at −48 ppm and its spinning sideband in the spectrum of Figure 5.2a. In the spectrum after 50 ms of spin diffusion (Figure 5.2b), the cross peaks for longer distance $^1$H–$^{31}$P correlation, i.e. between phosphorus and protons in NH and NCH$_2$ groups ($^1$H chemical shift at ~3 ppm), surpass those for the direct P–H bonding, due to their larger number. The $^1$H band of protons in P–NH groups, whose chemical shift varies between ~ 4 and 5.1 ppm in the literature,[27,28] is not clearly recognizable in the 2D HetCor spectra. For Naf-Phan-X, the phosphorus at 41 ppm correlates only to the NH and NCH$_2$ protons. The phosphorus at 5 ppm seems to be close to a proton at ~10 ppm (Figure 5.2c), which might suggest a strongly H-bonded proton (P – H…X where X = O or N). This could occur in structure **B**$^+$, wherein the presence of a five-membered -N-S-O-H-P-ring is conceivable. Further, a distinct set of cross peaks is seen at +3 ppm in the $^{31}$P dimension and ~ 6 ppm in $^1$H, assigned to P-H groups, confirming the presence of two components resonating near 5 ppm in the $^{31}$P spectrum of Naf-Phan-X. It is interesting to note that an impurity with quite similar $^{31}$P and $^1$H chemical shifts is visible in the spectrum of Phan-Cl, see Figure 5.2a.
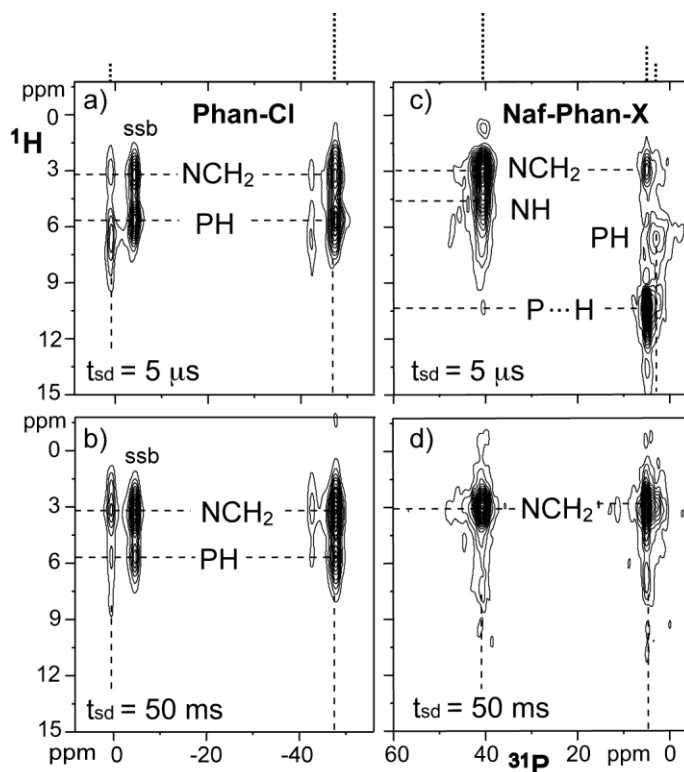
**Figure 5.2.** $^1$H–$^{31}$P HetCor spectra of (a, b) phosphatranium chloride (Phan-Cl) and (c, d) Naf-Phan-X with a CP time of 0.7 ms and at $v_r$ = 7 kHz for mixing times of 5 μs and 50 ms. For Phan-Cl, the HetCor spectra show the centerband at –48 ppm in the $^{31}$P dimension, a spinning sideband ("ssb") near –5 ppm, and an impurity peak at +1 ppm. The centerband positions are indicated by dashed lines at the top of the figure.

**$^{19}$F and $^{31}$P{$^{19}$F} REDOR NMR: changes in the Nafion® side chain.** The $^{31}$P NMR results have proven the change in phosphorus bonding from protonated to non-protonated for the primary product **A**$^+$ in the Naf-Phan-X sample. $^{19}$F NMR spectra (Figure 5.3) show that the fluorine in SO$_2$F groups in the precursor Nafion-F®, which originally resonated at +46.5 ppm, have totally disappeared in the $^{19}$F spectrum for Naf-Phan-X membrane. This confirms that Nafion® side chains have reacted by losing a fluorine atom. In addition, the $^{19}$F spectral lines have become broader, which indicates reduced mobility of the perfluoropolymer matrix,[29] likely due to attached large molecules.
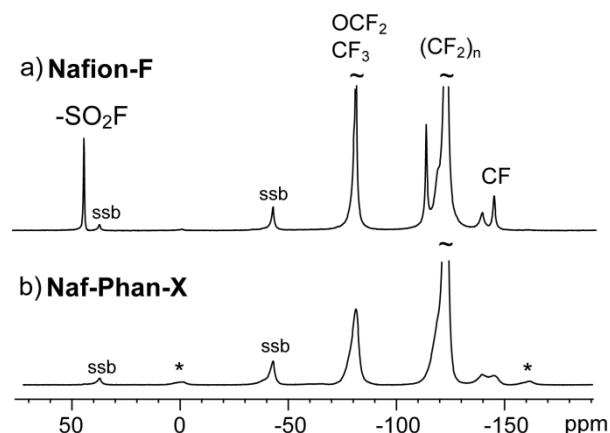
**Figure 5.3.** $^{19}F$ NMR spectra of a) Nafion-F$^®$ and b) Naf-Phan-X by direct polarization at $\nu_r = 30$ kHz. The peak of the $^{19}F$ directly bonded to sulfur at +46.5 ppm in Nafion-F$^®$ has disappeared in the Naf-Phan-X sample. In addition, the $^{19}F$ peaks of the Naf-Phan-X sample are broader than those of Nafion-F$^®$, which indicates reduced mobility. Spinning sidebands of the $(CF_2)_n$ peak are labeled "ssb" and those of the main side group signal by asterisks.

$^{31}P\{^{19}F\}$ REDOR experiments (Figure 5.4) were performed to confirm the bonding between the perfluoropolymer matrix and the proazaphosphatranium cations by estimating the distance between phosphorus and fluorine. Figures 5.4a and 5.4b show $^{31}P\{^{19}F\}$ REDOR reference ($S_0$) and dephased (S) spectra, respectively, for Naf-Phan-X at $Nt_r = 1$ ms. The $^{31}P$ peak at 41 ppm, tentatively assigned to $\mathbf{A}^+$ functionality from $^1H$-$^{31}P$ spectra, was dephased to 50%, while the peak at 5 ppm, (possibly associated with $\mathbf{B}^+$ from $^1H$-$^{31}P$ spectra) showed no significant dephasing. The REDOR experiment was also run at $Nt_r = 2$ ms, where the peak at 41 ppm had dephased to about 17% (circles in Figure 5.4c). The dephasing rate was compared to that of fluoroapatite, a crystalline mineral solid with a F–P distance of ~0.36 nm,[30] (triangles in Figure 5.4c). The dephasing of the phosphorus peak in Naf-Phan-X of functionality $\mathbf{A}^+$ is faster than for the phosphorus in fluoroapatite. This suggests an F–P distance comparable to ~0.4 nm, which corresponds approximately to a three-bond fluorine–phosphorus distance. This is confirmed by REDOR simulations, see dashed lines in Figure 5.4, of one $^{31}P$ spin coupled to many $^{19}F$ spins on a cubic lattice of 0.28-nm spacing (45 $^{19}F/nm^3$), analogous to simulations described previously.[31, 32] A time scaling factor of 0.73 was used, as determined from the fluoroapatite dephasing and consistent with the finite-pulse length effects (only 54% of a rotation period are without pulses). Adequate fits of the

dephasing in Naf-Phan were obtained for a closest $^{31}P$-$^{19}F$ distance of 0.4 $\pm$ 0.1 nm. Thus, the 41 ppm feature is again consistent with the $\mathbf{A^+}$ functionality, while the 5 ppm feature matches the larger P-F distance of the $\mathbf{B^+}$ functionality.
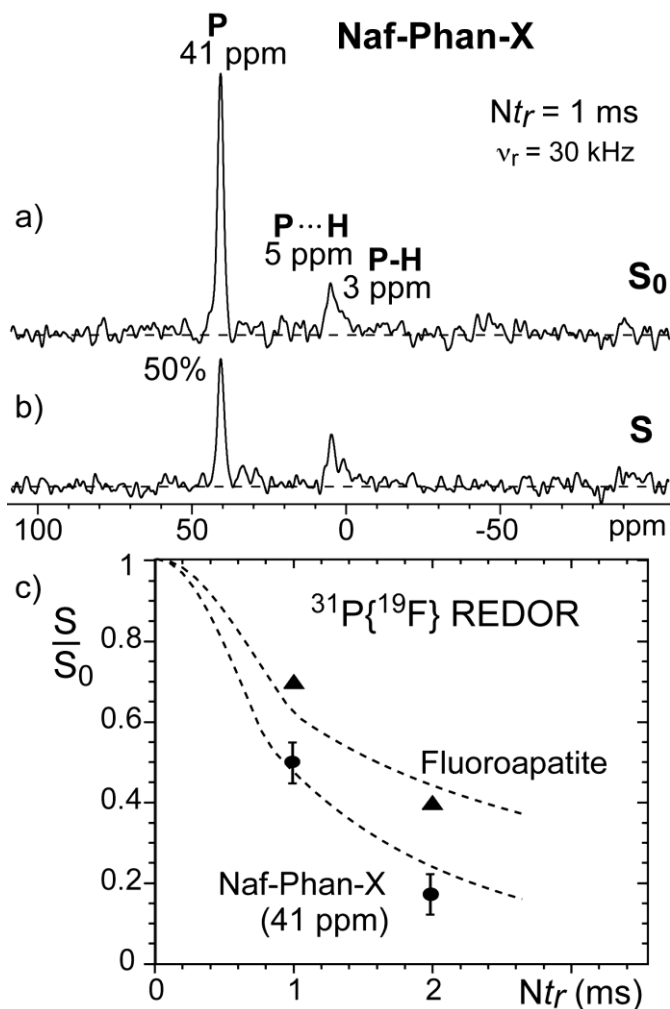


**Figure 5.4.** $^{31}P\{^{19}F\}$ REDOR spectra of Naf-Phan-X at $Nt_r = 1$ ms with recycle delay of 30 s and 256 scans. a) Reference spectrum ($S_0$) and b) spectrum after recoupling (S) which shows dephasing for $^{31}P$ peak at 41 ppm of 50% but little, if any, dephasing for the peak at 5 ppm. c) REDOR $S/S_0$ curve of Naf-Phan-X (circles) with comparison to fluoroapatite (triangles), which has an F–P distance of ~ 0.36 nm. Dashed lines are simulation curves, with a closest $^{31}P$-$^{19}F$ distance of 0.4-nm for Naf-Phan-X (further details see text).

**$^1H$–$^{13}C$ NMR: structure of the proazaphosphatranium cation.** To ensure that the primary structure of the phosphatranium chloride has not been altered during the synthesis of the Naf-

Phan-X membrane, a set of one-dimensional NMR spectra with spectral editing[33,34] was recorded (Figure 5.5). For phosphatranium chloride, the $^{13}C$ spectra clearly show two $NCH_2$ signals, at 34 ppm and 51 ppm. This assignment is confirmed by spectral editing that selects signals of $CH_2$ groups, see Figure 5.5c. The $^{13}C$ chemical shifts are in good agreement with literature values (see below). However, for Naf-Phan-X, four $^{13}C$ peaks were observed. In addition to signals at 54 ppm and 46 ppm, assigned to $NCH_2$ groups of the proazaphosphatranium cations bonded to Nafion®, additional bands are seen at 159 ppm, from a protonated carbonyl group (aldehyde, HC=O), and at 37 ppm, from a methyl group which persists in the spectrum after gated decoupling due to motional averaging of C-H coupling by fast uniaxial rotation. The carbonyl and methyl groups are most likely from dimethylformamide (DMF), the swelling agent used, which may be trapped in the membrane. The structure and solution state $^{13}C$ chemical shifts of DMF are shown in Figure 5.5. As expected, in the $^{1}H$ –$^{13}C$ HetCor spectra (Figure 5.6) the carbonyl carbon correlates to a proton at ~8 ppm, and all other carbons correlate to $NCH_n$ protons at ~3 ppm. Interestingly, one methyl group of DMF, which resonates at 31.3 ppm, is not observed in the $^{13}C$ spectra of Naf-Phan-X. The second correlation of the 159 ppm $^{13}C$ resonance to a $^{1}H$ at 3 ppm is consistent with a more distant coupling to $NCH_n$ protons, as confirmed by its relative prominence with a longer delay for spin diffusion, see Fig. 6(b).
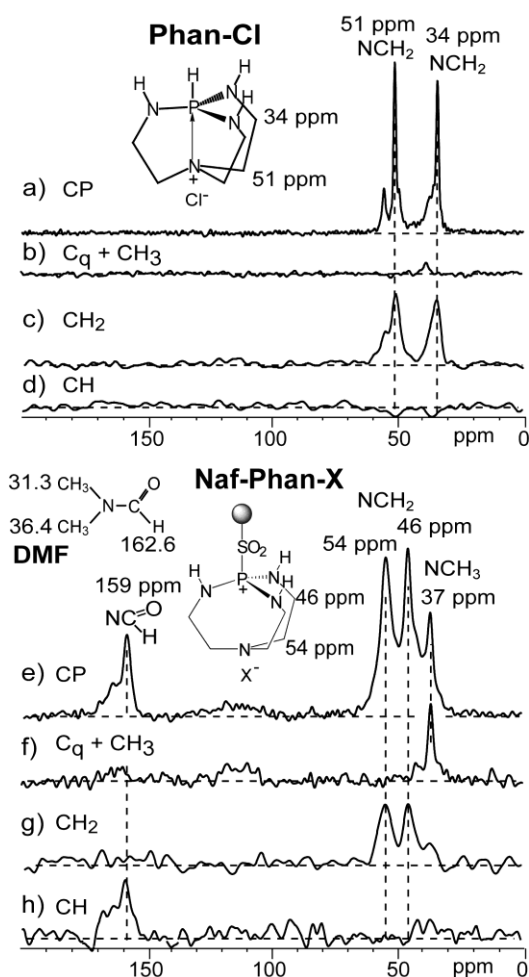
**Figure 5.5.** $^{13}$C spectra of phosphatranium chloride (Phan-Cl, a-d) and Naf-Phan-X membrane (e-h). (a, e) CP and (b, f) CP/gated decoupling experiments, run at $\nu_r$ = 6.5 kHz; (c, g) CH$_2$- and (d, h) CH-selection experiments at $\nu_r$ = 5.787 kHz. For phosphatranium chloride, two peaks of CH$_2$ bonded to nitrogen are seen, at 34 ppm and 51 ppm. For Naf-Phan-X, the two CH$_2$ peaks shift to 46 ppm and 54 ppm, respectively. In addition, a protonated carbonyl group and a nitrogen-bonded methyl group are present in a ~1:1 ratio. These are most likely from the swelling agent N,N-dimethyl formamide (DMF) trapped in the membrane. The structure of DMF is shown, with solution state $^{13}$C chemical shifts indicated.
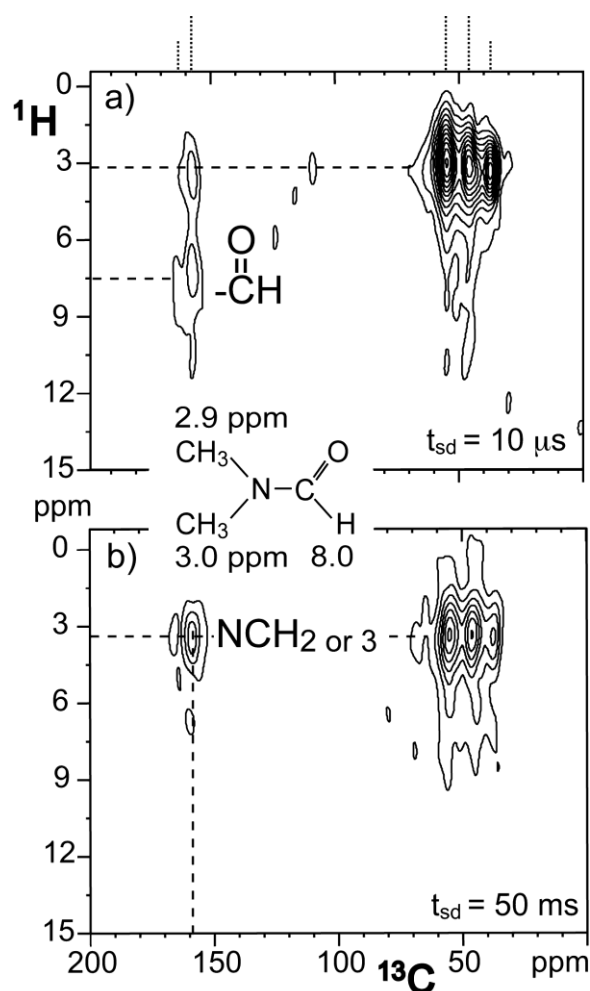
**Figure 5.6.** $^1H$–$^{13}C$ HetCor spectra of Naf-Phan-X with spin-diffusion times of a) 10 μs and b) 50 ms at $v_r$ = 6.5 kHz. $^{13}C$ signal positions are indicated by dashed lines at the top of the figure. Solution state $^1H$ NMR chemical shifts for DMF are shown with the structure.

**$^{15}N$ NMR.** The $^{15}N$ NMR spectrum of phosphatranium chloride obtained by cross polarization from $^1H$ (Figure 5.7) shows a peak at 50 ppm (referenced to liquid $NH_3$) from protonated nitrogen, and a peak at 37 ppm from non-protonated (tertiary) nitrogen, so assigned due to signal persistence in the CP/gated experiment, see Fig 7b. A small signal is also observed at 23 ppm, but due to limited sensitivity it is uncertain whether this is protonated or not. The relative peak areas are 1.6:1:0.5, which does not match the expected 3:1 ratio. However, it should be noted that a significant level of degradation products are detected in the $^{31}P$ spectrum of this sample, see Figure 5.1a, and similar degradation might

account for the 23 ppm $^{15}$N resonance.  The signal of the protonated nitrogen has been shifted to 25 ppm in the spectrum for Naf-Phan-X (Figure 5.7c).  No peak of non-protonated nitrogen is seen, which may be due to low cross-polarization efficiency of this tetra-coordinated nitrogen strongly diluted in the polymer matrix; the cross-polarization condition may have shifted due to power absorption by the slightly conductive sample.  The $^{15}$N peak at 116 ppm can be assigned to an amide (N-C=O) structure; it may come from DMF, but the nitrogen appears to be protonated (HN-C=O).
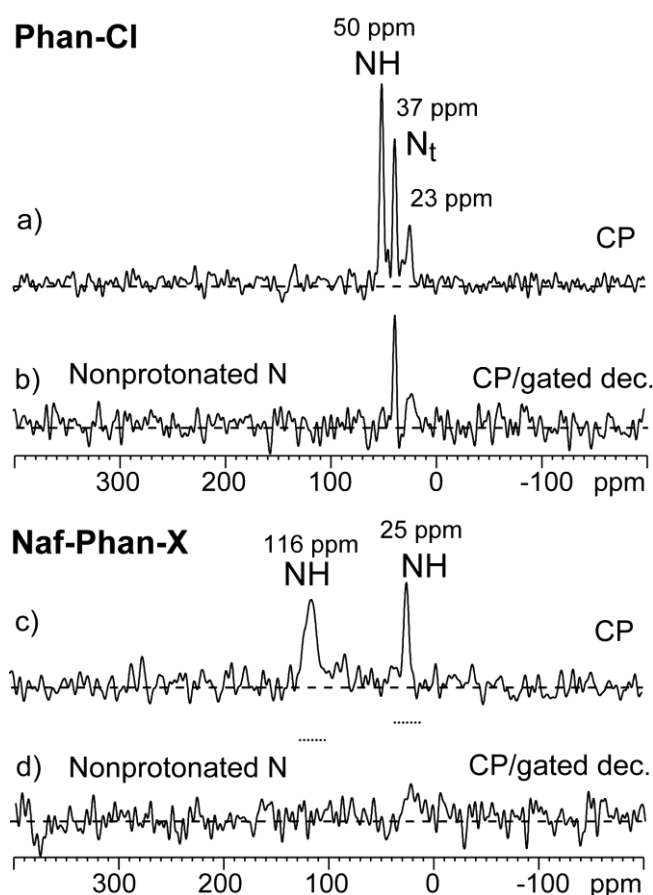


**Figure 5.7.** $^{15}$N spectra of phosphatranium chloride (a, b) and Naf-Phan-X (c, d) obtained after CP and CP with recoupled gated decoupling, respectively, at $v_r$ = 5 kHz.  Dashed horizontal lines in d) mark the intensity expected if the N observed in c) was not protonated.
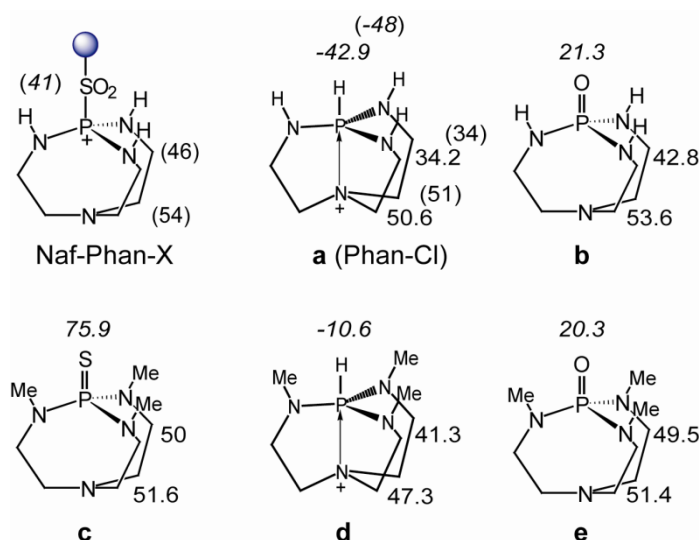
**Figure 5.8.** Chemical shifts of structures similar to phosphatranium chloride from reference 26. [31]P chemical shifts are in italics, while ^{13}C chemical shifts are in regular font. The results from our experiments are given in parentheses.

**Analysis of chemical shifts.** In Figure 5.8, literature chemical shift values[27] of [31]P (in italics) and [13]C (in regular font) are listed for phosphatranium chloride and its derivatives. For phosphatranium chloride, the literature values agree well with the results from our experiments (given in parentheses). Though none of the derivatives have the same structure as Naf-Phan-X, we can analyze them to obtain insights into chemical shift trends. For example, substituting the proton on phosphorus by a sulfur (from structure **d** to **c**) changes the ^{31}P chemical shift by +87 ppm, which is similar to the change by +89 ppm from phosphatranium chloride to the chemical shift assigned to the proazaphosphatranium functionality **A**[+] in Naf-Phan-X. In addition, the similar ^{13}C chemical shifts for structures **b**, **c**, **e** and Naf-Phan-X may indicate elongation of the cage-like molecular structure of the proazaphosphatranium functionality **A**[+] in Nafion-Phan-X. Such elongation is relative to structures a (Phan-X) and d of Fig. 8, with their shorter P-N distances due to transannular donation of a nitrogen lone pair to phosphorous. This bonding yields correspondingly unique ^{13}C shifts and a P-N distance of ~0.2 nm, in contrast to ~0.3 nm for structures **b**, **c** and **e**, [35] whose ^{13}C shifts are more akin to the Naf-Phan-X system.

**Structural implications.** The new AAEM possesses several interesting features which we now discuss. Resonance structures of proazaphosphatranium cations of type **A**[+] in Scheme

5.2b can distribute the positive charge in the P–N bonds surrounding the phosphorus (Scheme 5.3). Such resonance structures minimize coulombic attractions between the cations and anions, and hence can improve the mobility of the anion. It is interesting that analogous cations representative of $\mathbf{A}^+$ and $\mathbf{B}^+$ {i.e., $[-CS(O)_2P(N-)_3]^+$

and $[-CS(O)_2N(C)P(N-)_2]^+$, respectively} are, to our knowledge, completely unprecedented in the literature. The robust mechanical, oxidative, hydrolytic and thermal stability of the Nafion® framework, the diffuse distribution of positive charge and hydrolytic stability of 4-coordinate proazaphosphatranium and 5-coordinate phosphatranium cations are combined in the novel "hybrid" AAEM depicted in Scheme 5.2. Thus we have in a formal sense transformed Nafion® from a PEM material into a halogenide- and a hydroxide-containing AAEM. We accomplished this "ion polarity inversion" of Nafion® by a simple experimental procedure using commercially available Nafion-F® as shown in Scheme 5.4. The Naf-Phan-OH film may be an excellent candidate in AFC fuel cell applications according to preliminary studies showing that it retains good conductivity under strongly basic conditions as well as at elevated temperatures.

## Conclusions

A Nafion–proazaphosphatranium/phosphatranium composite cationic film, a potential anion exchange membrane for direct methanol-based fuel cells, was successfully synthesized via a microwave process from Nafion-F® and phosphatranium chloride. Most of the latter was converted to proazaphosphatranium cations attached to the Nafion® via a P–S bond (structure $\mathbf{A}^+$), as shown by $^{31}P\{^{1}H\}$, $^{19}F$, and $^{31}P\{^{19}F\}$ REDOR NMR. These ionophores have a reduced charge density due to resonance structures that distribute positive charge to diminish ionic interaction, which should facilitate hydroxide ion mobility. Electrical measurements to complement the present structural study and further test these hypotheses are underway. The 4-coordinate stereochemistry of phosphorus in the novel proazaphosphatranium cation was substantiated by $^{13}C$ and $^{15}N$ NMR. About 1/3 of the phosphatranium ions are converted into two other structures, with S not bonded to P but most likely to N as in structure $\mathbf{B}^+$. In addition, moieties derived from the solvent, DMF, were found in the final product. Efforts to inhibit formation of these impurities are underway.

## Acknowledgements

## References

(1)  Chu, D.; Jiang, R. *Solid State Ionics* **2002**, *148*, 591.

(2)  Dyer, C. K. *J. Power Sources* **2002**, *106*, 31.

(3)  Chang, H.; Kim, J. R.; Cho, J. H.; Kim, H. K.; Choi, K. H. *Solid State Ionics* **2002**, *148*, 601.

(4)  Meyers, J. P.; Maynard, H. L. *J. Power Sources* **2002**, *109*, 76.

(5)  *Eye for Fuel Cells conference on Fuel Cells for Portable Applications* Hilton Back Bay, Boston, MA, USA, September 5th-6th **2002**.

(6)  Ren, X.; Zelenay, P.; Thomas, S.; Davey, J.; Gottesfeld, S. *J. Power Sources* **2000**, *86*, 111.

(7)  Raadschelders, J. W.; Jansen, J. *J. Power Sources* **2001**, *96*, 160.

(8)  Varcoe, J. R.; Slade, R. C. T., *Fuel Cells* **2005**, *5*, 187.

(9)  Lamy, C.; Belgsir, E. M.; Leger, J.-M., *J. Appl. Electrochem.* **2001**, *31*, 799.

(10) Tripkovic, A. V.; Popovic, K. D.; Grgur, B. N.; Blizanac, B.; Ross, P. N.; Markovic, N. M., *Electrochim. Acta*, **2002**, *47*, 3707.

(11) Yu, E. H.; Scott, K.; Reeve, R. W., *J. Electroanal. Chem.* **2003,** *547*, 17.

(12) Gamburzev, S.; Petrov, K.; Appleby, C. L., *J. Appl. Electrochem.* **2002**, *32*, 805.

(13) Wagner, N.; Schulze, M.; Gulzow, E., *J. Power Sources* **2004**, *127*, 264.

(14) Schulze, M.; Gulzow, E., *J. Power Sources* **2004**, *127*, 252.

(15) McLean, G. F.; Niet, T.; Prince-Richard, S.; Djilali, N. *Int. J. Hydrogen Energy* **2002**, *27*, 507.

(16) Schulze, M.; Gulzow, E., *J. Power Sources* **2004**, *127*, 243.

(17) Cifrain, M.; Kordesch, K. V., *J. Power Sources* **2004**, *127*, 234.

(18) Danks, T. N.; Slade, R. C. T.; Varcoe, J. R. *J. Mater. Chem.* **2002**, *12*, 3371.

(19) Sun, L.; Thrasher, J.S. *Polymer Degradation and Stability* **2005**, *89*, 43.

(20) Schmidt-Rohr, K.; Chen, Q. *Nature Materials* **2008**, *7*, 75.

(21) Laramay, M. A. H.; Verkade, J. G. *Z. Anorg. Allg. Chem.* **1991**, *605*, 163-174

(22) Bielecki, A.; Burum, D. P.; Rice, D. M.; Karasz, F. E. *Macromolecules* **1991**, *24*, 4820.

(23) Clauss, J.; Schmidt-Rohr, K.; Spiess, H. W. *Acta Polymer.* **1993**, *44*, 1.

(24) Bielecki, A.; Kolbert, A.C.; de Groot, H. J. M.; Griffin, R. G.; Levitt, M. H. *Adv. Magn. Reson.* **1990**, *14*, 111.

(25) Gullion, T.; Schaefer, J. *J. Magn. Reson.* **1989**, *81*, 196.

(26) Sinha, N.; Schmidt-Rohr, K.; Hong, M. *J. Magn. Reson.* **2004**, *168*, 358.

(27) Galasso, V. *J. Phys. Chem. A* **2004**, *108*, 4497-4504.

(28) Reddy, C. R. V.; Verkade, J. G. *J. Org. Chem.* **2007**, *72*, 3093.

(29) Chen, Q.; Schmidt-Rohr, K. *Macromolecules* **2004**, *37*, 5995.

(30) Nikcevic, I.; Jokanovic, V.; Mitric, M.; Nedic, Z.; Makovec, D.; Uskokovic, D. *J. Solid State Chem.* **2004**, *177*, 2565.

(31) Rawal, A.; Wei, X.; Akinc, M.; Schmidt-Rohr, K., *Chem. Mat.* **2008**, *20*, 2583.

(32) Schmidt-Rohr, K.; Rawal, A.; Fang, X.-W., *J. Chem. Phys.* **2007**, *126*, 05401-(1-16).

(33) Schmidt-Rohr, K.; Mao, J.-D. *J. Am. Chem. Soc* **2002**, *124*, 13938.

(34) Mao, J.-D.; Schmidt-Rohr, K. *J. Magn. Reson.* **2005**, *176*, 1.

(35) Verkade, J. G. In New Aspects of Phosphorus Chemistry II, *Top. Curr. Chem.* Majoral, J. P. Ed., **2002**, *233*, 1.

# Chapter 6

# Distribution of Silica and of Zirconium Phosphate in the Pores of Nafion

Xueqian Kong, Klaus Schmidt-Rohr

To be submitted to *Chem. Mat.*

## Abstract

The nanoscale structures of Nafion silica (NafSil) and Nafion zirconium phosphate (NafZrP) composites, which have improved fuel cell performance above $100^{o}C$ and at reduced hydration levels, have been studied by solid state nuclear magnetic resonance (NMR). $^{19}F$ NMR shows that the nanoparticles have little effect on the segmental mobility of the perfluoroionomer matrix. The silica particles are cylindrical with a ~ 2.8 nm diameter estimated from the surface-to-volume ratio that is measured by the fraction of $Si(OSi)_4$ "$Q^4$" interior sites in $^{29}Si$ NMR. The $^{19}F$-$^{29}Si$ internuclear distances between $(HO)Si(OSi)_3$ "$Q^3$" surface sites and the fluoropolymer matrix measured by $^{29}Si\{^{19}F\}$ rotational-echo double-resonance (REDOR) experiments indicate that the silica particles are in the core of water channels surrounded by a water layer of 0.8-nm thickness. $^{31}P$ NMR suggests that the ZrP formed inside Nafion consist of two disordered ZrP layers with dominant $(HO)P(OZr)_3$ sites. The elongated ZrP particles have an elliptical cross section with an area of ~ 6 $nm^2$. The thickness of the water layer surrounding ZrP particles is also around 0.8 nm, according to $^{31}P\{^{19}F\}$ REDOR experiments.

## Introduction

Nafion, a perfluoroinated ionomer, is widely used as the proton exchange membrane for low temperature fuel cells. It has a high conductivity of protons with good selectivity, and it has good chemical and mechanical stability under normal operating conditions.[1,2] The superior properties of Nafion can be attributed not only to its chemical structure, but also result from its nanoscale morphology. A model featuring parallel water channels is supported by

quantitative simulations of small-angle X-ray scattering curves[3] and the backbone stiffness seen by solid-state nuclear magnetic resonance (NMR).[4,5] Water channels lined by sulfonic acid side-groups provide pathways for proton transport, while fluoropolymer crystallites in the backbone provide the material with mechanical strength.

One of the crucial challenges for Nafion as a PEM is its deteriorated performance at higher temperatures ($> 90^oC$) and low hydration levels because water, which serves as the carrier for proton transport, cannot be retained under these conditions. As a result, the humidity and temperature inside a fuel cell must be controlled, which complicates the design and adds costs. The platinum catalysts in fuel cells are vulnerable to CO and other impurity gases at low operating temperatures. The development of new PEM materials that can perform well at high temperatures and low hydration level would be favorable for introducing affordable fuel cells into the automobile industry.

One promising approach to increasing the working temperature is to incorporate inorganic particles, such as silica and zirconium phosphate (ZrP), into Nafion. It has been reported that Nafion silica (NafSil) and Nafion zirconium phosphate (NafZrP) composites may operate in a fuel cell at temperatures of $120^oC$ or higher.[6,7] Knowledge of the nanoscale structures of the composites is important for understanding how the inorganic particles improve the properties of Nafion. X-ray diffraction (XRD) and scattering,[8-10][11] electron microscopy,[11,12] and NMR[13,14] have been applied to study these systems. SAXS and electron microscopy studies have shown that these Nafion inorganic are nanocomposites.[10,11] Based on SAXS studies, Yang et al. suggested that the ZrP and $SiO_2$ may act as rigid scaffolds that provide the membrane with dimensional stability against swelling,[15] while Ye et al.[13] suggested low $SiO_2$ loading with more surface OH groups in Nafion improve the proton conductivity.

In this paper, we use solid-state NMR primarily to study the nanometer-scale structure of the composites with ZrP or $SiO_2$ particles grown in-situ inside Nafion channels.[15,16] The effects of the inorganic particles on the polymer dynamics are investigated by ^{19}F NMR, the compositions of silica and ZrP by ^{29}Si and ^{31}P NMR, respectively. The particle sizes and shapes in the channels were studied, in particular, through internuclear distance

measurements by $^{29}Si\{^{19}F\}$ and $^{31}P\{^{19}F\}$ REDOR experiments. The spectroscopic observations are explained by suitable structural models.

## Experimental

**Materials.** Nafion 117 membranes were obtained from ElectroChem Inc, MA. Tetraethyl orthosilicate (TEOS) and HCl were purchased from Sigma-Aldrich. $HNO_3$ was purchased from Fisher Scientific.

**Sample preparation**. Nafion 117 membrane was boiled first in 0.5 M $H_2SO_4$ for 2 hrs and then in deionized $H_2O$ until the pH reached 7. It was then dried in vacuum at room temperature and kept in a desiccator for weeks.

*Nafion zirconium phosphate.* Pre-treated Nafion was later swelled in ethanol/water (1:1 in volume) at 80$^{\circ}$C for 3 hrs. Then Nafion was immersed in 1M $ZrOCl_2$ solution at 80$^{\circ}$C for 2 hrs, followed by immersion in 1M $H_3PO_4$ at 80$^{\circ}$C for 17 hrs. After that, it was boiled in deionized $H_2O$ for 4 hrs to remove excess acid and solvent. The composite membrane was dried in vacuum at 105$^{\circ}$C for 1 day and then stored in a desiccator for weeks before NMR and TGA measurements.

*Nafion silica composite and pure silica.* Pre-treated Nafion was swelled in $H_2O$/ethanol (1:4 in volume) solution for 24 hrs. After that, TEOS was introduced into the solution under stirring, where the TEOS/$H_2O$ mole ratio was kept at 1:4. 10 minutes later, the membrane was immediately removed from the solution, rinsed in ethanol for 1 to 2 seconds and blotted dry. After that, the composite membrane was dried under vacuum at 105$^{\circ}$C for 1 day and then stored in a desiccator for weeks before NMR and TGA measurements.

The pure silica gel was prepared by mixing TEOS with 0.05 M HCl solution (TEOS/$H_2O$ 1:4 mole ratio) at 50$^{\circ}$C for 2 hrs. The mixture was then dried under vacuum at 105$^{\circ}$C for 1 day to form silica gel.

*Nafion doped with tetramethylammonium.* Nafion 117 film incorporating a small amount of tetramethylammonium (TMA) cations was obtained from R. Moore's research group in Virginia Polytechnic Institute and State University.

**NMR parameters.** NMR experiments were performed on a Bruker DSX-400 spectrometer at a resonance frequency of 400 MHz for $^1$H, 376 MHz for $^{19}$F, 162 MHz for $^{31}$P, and 79.5 MHz for $^{29}$Si using double-resonance or triple-resonance MAS probes. $^{19}$F experiments were performed in 2.5-mm rotors at 30 kHz. $^{29}$Si spectra were measured in 4-mm rotors at a spinning speed of 6.5 kHz with a recycle delay of 100 s. $^{31}$P spectra were measured in 4-mm rotors at a spinning speed of 8 kHz with a recycle delay of 60 s. Two-pulse phase-modulation (TPPM)[17] was used for $^1$H-$^{31}$P heteronuclear dipolar decoupling. All experiments were carried out at ambient temperature.

*$^{31}$P{$^{19}$F} and $^{29}$Si{$^{19}$F} REDOR.* $^{31}$P{$^{19}$F} and $^{29}$Si{$^{19}$F} rotational-echo double-resonance (REDOR) experiments[18] were performed in 2.5-mm rotors at a spinning speed of 30 kHz, and in 4-mm rotors at a spinning speed of 4 kHz, respectively. The dephasing of $^{31}$P /$^{29}$Si magnetization was observed in the field of $^{19}$F spins. $^{19}$F composite 180$^o$ pulses were applied spaced by $t_r$/2 during $Nt_r$ period in order to recouple the dipolar interaction between $^{31}$P /$^{29}$Si and $^{19}$F. EXORCYCLE was used for the single 180$^o$ pulse on the $^{31}$P /$^{29}$Si channel.[19] The recoupling $^{19}$F pulses were turned off when obtaining the reference signal. $^1$H decoupling was applied in the $^{29}$Si{$^{19}$F} REDOR but not in the $^{31}$P{$^{19}$F} REDOR.

*$^1$H{$^{19}$F} REDOR.* $^1$H{$^{19}$F} REDOR was performed on 4-mm MAS probe equipped with an HFX unit. The MAS spinning speed was 5.5 kHz.

*$^{31}$P-$^{31}$P 2D exchange.* $^{31}$P-$^{31}$P 2D exchange experiments were performed at 6250 Hz MAS. $^{31}$P magnetization was generated through direct polarization with 1-s recycle delay and 0.1-s spin diffusion time.

*$^1$H-$^{29}$Si HetCor.* Two-dimensional (2D) $^1$H-$^{29}$Si heteronuclear correlation (HetCor) experiments [20] were performed in 4-mm rotor at a spinning speed of 6.5 kHz. Frequency-

switched Lee-Goldburg (FSLG) homonuclear decoupling [21] was applied during the evolution period $t_1$. Lee-Goldburg cross polarization (LGCP) of 1 ms or 5 ms was used to suppress $^1H$-$^1H$ spin diffusion during polarization transfer and to show mostly two-bond $^1H$-$^{29}Si$ proximities. 10-µs mixing times ($t_m$) were used to allow minimum spin diffusion

*Enhancing $^{29}Si$ signals.* In $^{29}Si\{^{19}F\}$ REDOR experiments, the signal of $^{29}Si$ was enhanced by refocusing the $^{29}Si$ magnetization with multiple Hahn echoes during signal detection.[22,23] A train of $^{29}Si$ 180$^o$ pulses, separated by a delay of 2n rotor periods with n=2, or 0.8 ms, typically, was applied during the acquisition time. The total acquisition time was 60 ms.

**Thermogravimetric analysis measurement.** A TA Instruments$^®$ Q50 thermogravimetric analyzer (TGA) was used to obtain the thermograph of the composite membrane. The sample was heated from ambient to 630$^o$C at a rate of 10$^o$/min under constant air flow.

**X-ray diffraction.** Powder X-ray diffraction (XRD) measurements were performed on a Scintag XDS 2000 diffractometer using a quartz substrate.

**Results and Discussion**

*Thermogravimetric analysis.* The weight percentage of silica or ZrP can be obtained from TGA measurement. 15 wt% of silica (against the mass of dry Nafion) was measured for NafSil composite and ~20 wt% of ZrP was measured for NafZrP. These correspond to 15 vol% and 13 vol%, respectively, given that the density of Nafion is ~2.0 g/cm$^3$, the density of silica is ~2.0 g/cm$^3$, and the density of ZrP is ~ 3.3 g/cm$^3$. In both samples, the weight fraction of water is around 10%, which corresponds to ~ 20% of water in volume. In NafSil, the molar ratio (Si : -SO$_3^-$) is approximately 2.8 : 1. In NafZrP, the molar ratio (Zr : P : -SO$_3^-$) is 1 : 2 : 1.3.

*X-ray diffraction (XRD).* XRD patterns (Figure 6.1) indicate that the ZrP and SiO$_2$ in Nafion are mostly amorphous and the crystallinity of Nafion may be reduced as seen by the

broadened polymer diffraction peak. The observation is consistent with literature findings, though some α-crystalline structure of ZrP has been observed at high ZrP loadings.[8,12]
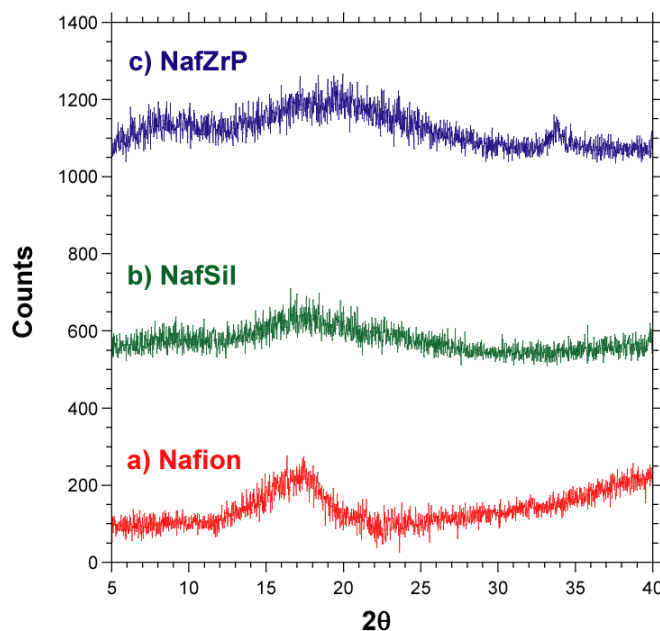


**Figure 6.1.** X-ray diffraction (XRD) patterns of (a) Nafion, (b) NafSil, and (c) NafZrP.

### Structural models of Nafion composites

*^{19}F NMR.* ^{19}F NMR spectra of NafSil and NafZrP were compared to that of pure Nafion (Figure 6.2). For NafSil and NafZrP, the changes in the ^{19}F spectrum are insignificant, which indicates that the mobility of Nafion backbone and side-chains are not significantly affected by the presence of silica or ZrP particles.
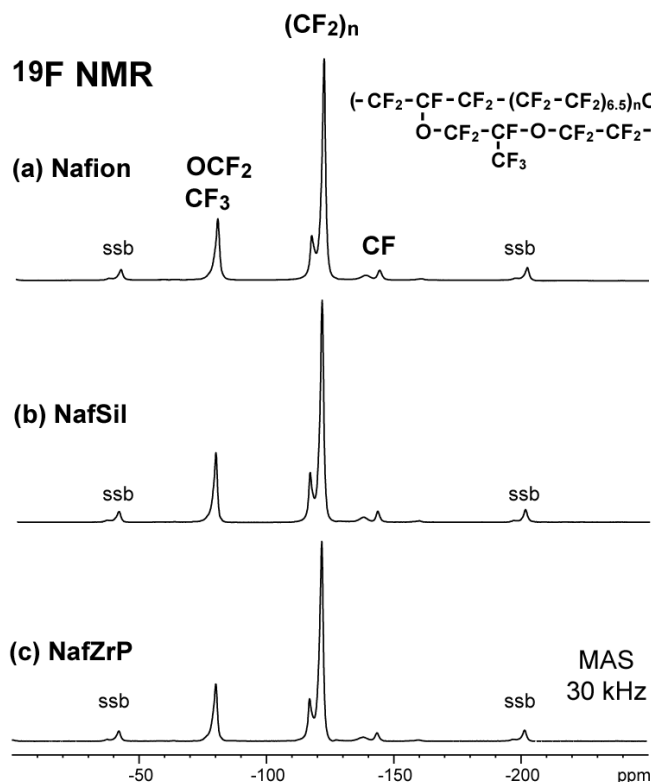
**Figure 6.2.** $^{19}$F NMR with direct polarization of (a) Nafion, (b) NafSil and (c) NafZrP. MAS = 30 kHz.

*Particle size from $^{29}$Si NMR of NafSil.* In the sol-gel process, the TEOS solution hydrolyzes under acidic conditions and condenses into silica particles.[24] The size of the particles may depend on the preparation conditions, such as pH, concentration of precursors, and drying temperature. The size and surface-to-volume ratio (S/V) of silica nanoparticles can be derived from quantitative $^{29}$Si NMR (Figure 6.3) based on the fraction of surface silicon sites. Different silicon sites, labeled as $Q^n$, have their own characteristic chemical shift ranges.[25] $Q^n$ sites are connected to n neighboring silicon atoms by bridging oxygens, i.e. $Si-(OSi)_n(OR)_{4-n}$ (where R = H or $C_2H_5$). The $Q^0$ to $Q^4$ sites have $^{29}$Si chemical shifts of $\sim -70$ ppm, $\sim -80$ ppm, $\sim -90$ ppm, $\sim -100$ ppm and $\sim -109$ ppm, respectively. For silica particles, $Q^2$ and $Q^3$ sites are on the surface, while $Q^4$ sites are in the interior. The area fraction of $Q^2 + Q^3$ represents the S/V ratio of the silica particles.

$$\frac{\text{Surface}}{\text{Volume}} = \frac{\text{area of } Q^2 \text{ \& } Q^3}{\text{total area}}$$

$$S/V = \frac{\pi R^2 \cdot L - \pi(R-u)^2 \cdot L}{\pi R^2 \cdot L} \quad \text{for cylinders}$$

$$S/V = \frac{\frac{4}{3}\pi R^3 - \frac{4}{3}\pi(R-u)^3}{\frac{4}{3}\pi R^3} \quad \text{for spheres}$$

Diameter of a $SiO_2$ particle $= 2R + 2r_{oxygen}$

Given a presumed particle shape, the diameter of the particles can be estimated based on the S/V ratio. The specific diameter of a $SiO_2$ unit "$u$" can be determined from the density of amorphous silica (2.2 g/cm$^3$) [26] following the calculation below.

$$u^3 = V_{SiO_2} = \frac{M_{SiO_2}}{N_A \rho_{SiO_2}} = \frac{60 \text{g} \cdot \text{mol}^{-1}}{6.0 \times 10^{23} \text{mol}^{-1} \times 2.2 \text{g} \cdot \text{cm}^{-3}} = 4.5 \times 10^{-23} \text{cm}^3 = (3.6 \text{Å})^3$$

The spectral fractions of $Q^2$, $Q^3$, and $Q^4$ signals obtained from direct polarization (DP) $^{29}$Si NMR (Figure 6.3) were 9.6%, 56.2%, and 34.2%, respectively for pure silica, and 3.8%, 42.2%, and 54.0%, respectively for NafSil. The S/V ratio of pure silica gel prepared by the sol-gel process is 0.66 nm$^{-1}$, corresponding to a diameter of 2.5 nm assuming spherical particles, which is consistent with the literature.[24] For silica grown inside Nafion, the S/V ratio decreased to 0.46 nm$^{-1}$. The corresponding particle diameter is 2.8 nm for cylindrical particles, or 4.0 nm for spherical particles. Since the silica particles are grown inside the water channels of Nafion, particles with a cylindrical shape are more likely given the spatial constraints and their reduced S/V ratio.
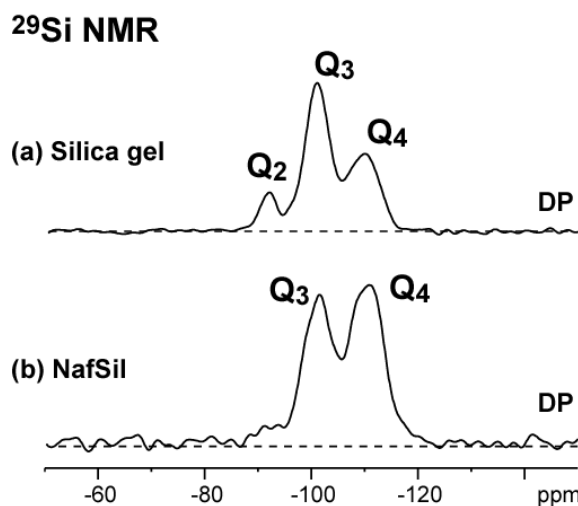
**Figure 6.3.** $^{29}$Si NMR with direct polarization of (a) silica gel and (b) NafSil with 100-s recycle delay.

*$^{31}$P NMR of NafZrP.* For ZrP grown in Nafion, the major $^{31}$P resonance at -22.4 ppm (Figure 6.4a), which accounts for ~ 80% of total $^{31}$P sites, is assigned to $(HO)P(OZr)_3$, labeled as "$Q^3$". The $^{31}$P chemical shift is different from that of α-ZrP (-18.8 ppm) and anhydrous α-ZrP (-21.3 ppm). The -6.7, -14.5, and -28.2 ppm $^{31}$P peaks are assigned to $(HO)_2P(OZr)_2$ "$Q^2$", $(HO)_2P(OZr)_2$ "$Q^2$", and $P(OZr)_4$ "$Q^4$", respectively. A $^{31}$P NMR spectrum after dipolar recoupling to $^1$H was also measured, which shows that only ~ 50% of the $Q^3$ sites have strong dipolar coupling to protons. It suggests that the $Q^3$ sites are in two different environments although their chemical shifts overlap. The $Q^3$ sites with weak dipolar coupling are probably involved in fast proton exchange with water. The connectivity of these $^{31}$P sites can be determined from 2D exchange NMR spectra (Figure 6.4b). In order to detect the low-intensity peaks at -6.7 and -14.5 ppm, whose $T_1$ relaxation times are short, a short recycle delay of 1 s was used. The cross peaks show that the protonated $^{31}$P sites are connected to each other in the nanometer scale. The mole fractions of these sites are listed in Table 6.1.
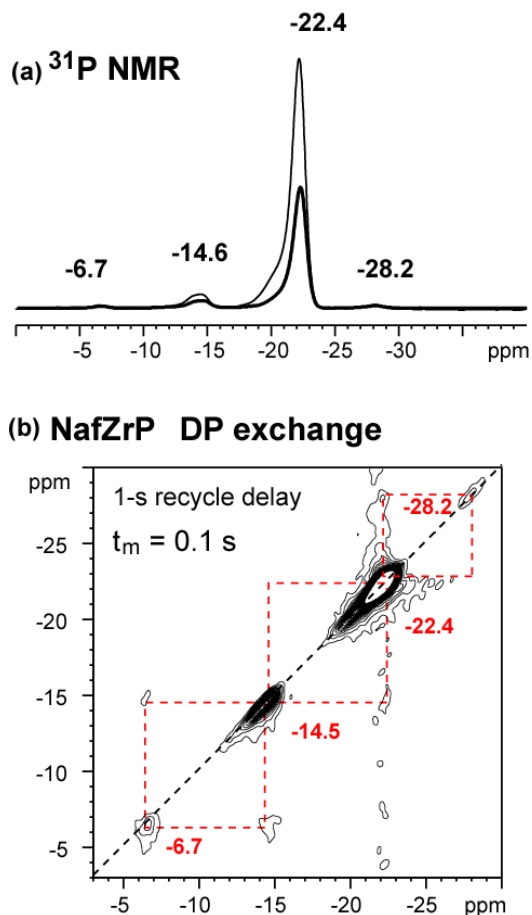
**Figure 6.4.** (a) $^{31}$P NMR of NafZrP with direct polarization and 60-s recycle delay (thin line) and same after dipolar recoupling to $^{1}$H (bold line). (b) $^{31}$P 2D DP exchange spectrum of NafZrP, with 1-s recycle delay and a mixing time of 0.1 s.

| $^{31}$P chem. shift | -6.7 ppm | -14.5 ppm | -22.4 ppm | -28.2 ppm |
|---|---|---|---|---|
| Mole fraction | 1.2% | 7.4% | 88.9% | 2.5% |

**Table 6.1.** Mole fractions of different $^{31}$P sites in NafZrP.

*Internuclear distance measurements.* The distance between the atomic sites in the internally grown inorganic particles and Nafion polymer matrix can be estimated by X{$^{19}$F} REDOR experiments (Figure 6.5). The X{$^{19}$F} REDOR experiments measure the dipolar coupling

strength between X nuclei and $^{19}F$ spins, which can be converted into internuclear distances.[18] The X{$^{19}F$} REDOR experiments use rotor-synchronized $180^{\circ}$ $^{19}F$ pulses to recouple the dipolar interaction that is removed by magic angle spinning. For data analysis, the ratio of the spectral intensity with REDOR recoupling (S) over the spectral intensity without REDOR recoupling (S$_0$) is plotted against total recoupling time (N$t_r$). A steeper dephasing curve indicates a shorter internuclear distance.

For NafSil, the distance between surface Q$^3$ sites and the fluoropolymer matrix is closer than the distance between internal Q$^4$ sites and fluoropolymer (Figure 6.5a). It suggests that the silica particles are grown at the center of water channels. The $^{29}Si$-$^{19}F$ distance of Q$^3$ sites is around 1 nm, which corresponds to a water layer of around 0.8-nm thickness that surrounds the particle excluding the volume occupied by sulfonate side-groups and the oxygen atoms attached to silicon (Figure 6.6). At this distance, the Nafion side-group is not in contact with the silica particles, which is in agreement with the $^{19}F$ NMR results.

In NafZrP, the $^{31}P$-$^{19}F$ distances of different $^{31}P$ species are all around 1 nm (Figure 6.5b), which suggests that, similar to NafSil, the ZrP particles in Nafion also have a surrounding water layer of 0.8-nm in thickness, again in agreement with the $^{19}F$ NMR results. The $^{31}P$-$^{19}F$ distances of the various $^{31}P$ sites are similar, but some differences are observed. The (HO)$_2$P(OZr)$_2$ "Q$^2$" site at -14.5 ppm shows the shortest distance from the Nafion matrix; while the P(OZr)$_4$ "Q$^4$" at -28.2 ppm shows the longest. It could be rationalized as follow: the (HO)$_2$P(OZr)$_2$ "Q$^2$" species are at the particle surface, which is close to Nafion matrix; the (HO)P(OZr)$_3$ "Q$^3$" species could be both on the interior and the surface of the particles, and the average $^{19}F$-$^{31}P$ distance is moderately greater than Q$^2$ species; the P(OZr)$_4$ "Q$^4$" species are mostly in the interior so its $^{19}F$-$^{31}P$ distance is the longest. The REDOR curve for the -6.7 ppm peak is not shown due to the large error margin. However, since the differences of the $^{19}F$-$^{31}P$ distances are within a few angstroms, the thickness of the ZrP particle is expected to

be small. In addition, from $^{31}$P NMR of NafZrP, we know that ~ 50% of the dominant $Q^3$ species have access to water. Considering the confinement effect of water channels, the internuclear distance, and the factions of $^{31}$P species, an elongated ZrP particle consisting of roughly two ZrP layers is the most likely structure. This observation is different from the analysis of the X-ray scattering peaks and SEM by Truffier-Boutry et al.,[11] who suggested that the ZrP forms oblate ellipsoids with 56-nm length and 7-nm thickness. Note that our model is supported by the absence of sharp Bragg peaks in the XRD pattern (Figure 6.1).
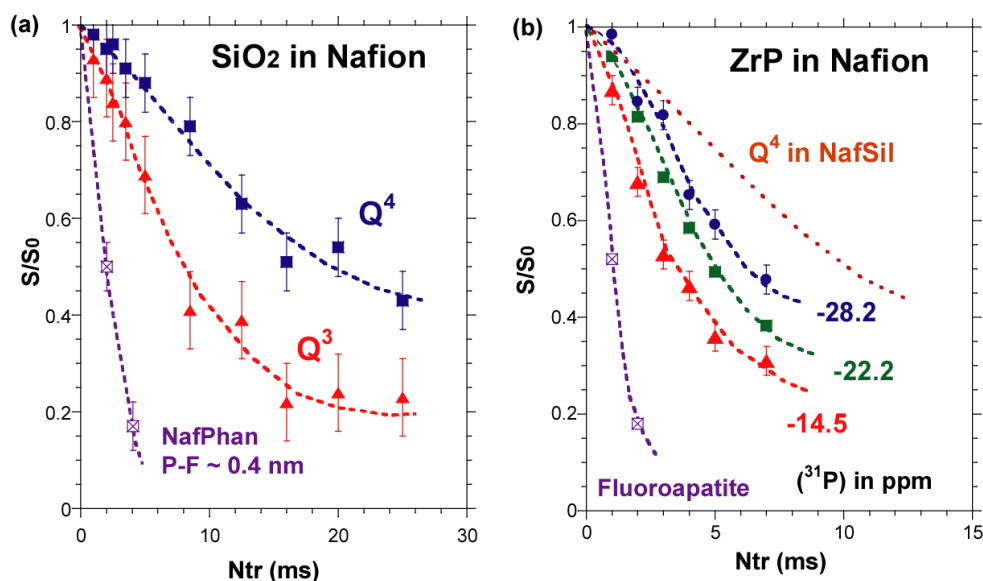


**Figure 6.5.** (a) $^{29}$Si$\{^{19}$F$\}$ REDOR of NafSil with MAS = 4 kHz. (b) $^{31}$P$\{^{19}$F$\}$ REDOR of NafZrP with MAS = 14 kHz. The lines are guides to the eye. The dephasing curve of $Q^4$ of NafSil in (b) is scaled according to the gyromagnetic ratios of $^{29}$Si and $^{31}$P.
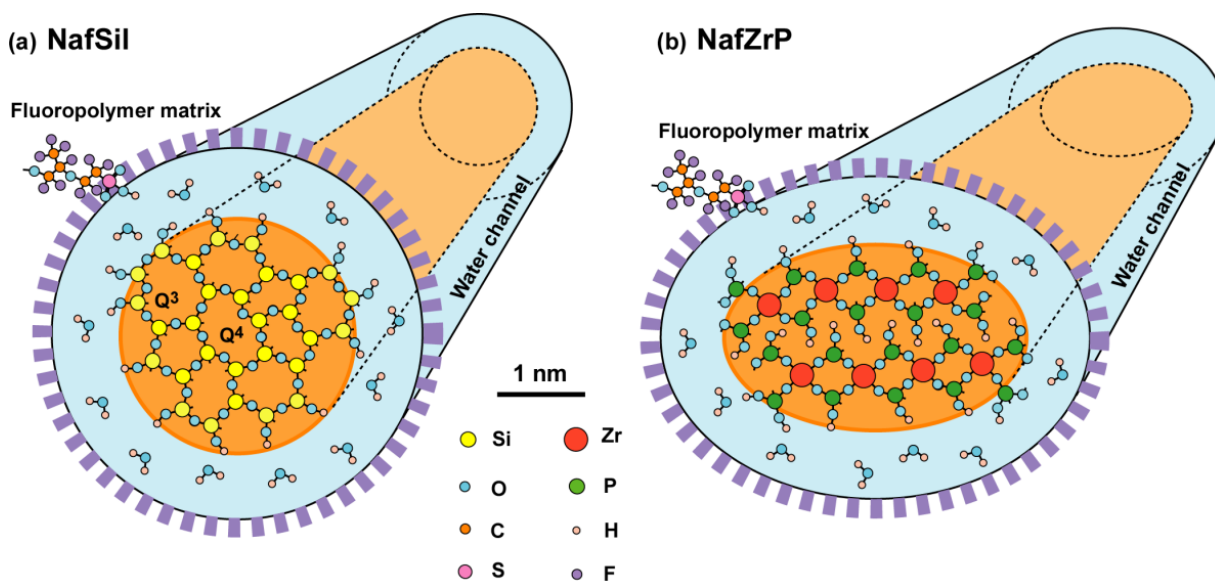
**Figure 6.6.** Models of water channels and inorganic phases in (a) NafSil and (b) NafZrP. The cylinders represent segments of a water channel. Most of the fluoropolymer matrix is omitted in the figure. The filled circles representing different atoms are labeled in the figure.

*Estimating particle size in NafZrP.* The size of inorganic particles may also be analyzed via their volume fraction in Nafion assuming the parallel channels persist in the composites. In both materials studied, the inorganic particles, water, and fluoropolymer matrix occupy approximately 10%, 15%, and 75% of the total volume, respectively. In NafSil, the water/silica volume ratio obtained from particle diameters is $[(1.4+0.8)^2-1.4^2]/1.4^2 = 1.5$ in agreement with the volume ratio of 15%/10% = 1.5 obtained from TGA. In NafZrP with an only slightly smaller inorganic volume fraction, the size of ZrP particles should be almost as large as that of silica in Nafion. In the model of NafSil (Figure 6.6a), the radius of cylindrical particle is around 1.4 nm with a surrounding water layer of 0.8-nm thick. To account for the layered structure of ZrP, we propose an elliptical cross-section structure model of NafZrP composite compared to a circular cross-section in the structural model of the NafSil composite. In the model of NafZrP (Figure 6.6b), the major and minor diameters of the

elliptical cross section are approximately 3.6 nm and 2.2 nm, respectively. The values match the thickness of two ZrP layers and to provide the correct volume fraction; the thickness of the surrounding water layer is again ~ 0.8 nm. In both models, the inorganic particles form elongated structures along the water channels in Nafion although they could be discrete along the channel direction.

*Si-OH groups of the Nafion-silica composite*

In the models of NafSil and NafZrP presented above, the connectivity of water channels, thus the water transport pathway, is preserved by the water layers surrounding the inorganic particles. This explains why these composite materials, when hydrated, have proton conductivities comparable to normal Nafion [6,7]. The surface of the inorganic particles may play an important role in maintaining proton conductivity at low hydration levels or at higher temperatures, where the fuel cell performance of the composites surpasses that of Nafion. In the following, we demonstrate that solid-state NMR can be used to characterize the surface of the inorganic nanoparticles, in particular silica in Nafion. A more comprehensive investigation of the surface of zirconium phosphate in Nafion will be published elsewhere.

The $^1$H NMR spectra of pure silica gel and the NafSil composite are shown in Figure 6.7a and 7b, respectively. The former exhibits signals at 5, 3.6, and 1.2 ppm. The peak at ~ 5 ppm is assigned to water molecules adsorbed on the silica surface which are known to be weakly hydrogen-bonded to Si-OH groups. [23] The other two signals at 1.2 ppm ($CH_3$) and 3.6 ppm ($OCH_2$) are assigned to the unreacted ethoxyl groups and trapped ethanol. Signals of these two species can be resolved in $^{13}$C NMR (Figure 6.7c). The broadened peak at ~ 61 ppm can be assigned to $OCH_2$ of unreacted ethoxyl group, with broadening due to reduced mobility.

The presence of a considerable amount of unreacted ethoxyl group suggests that the hydrolysis reaction of TEOS was not complete. For the silica particle grown inside Nafion, the $^1$H NMR spectrum (Figure 6.7b) shows that the chemical shift of water is around 7.5 ppm. The downfield shift, compared to liquid water at pH = 7 (5 ppm), is due to the acidic environment in the Nafion channels. There is a weak and relatively broad $^1$H peak resonating at ~ 5 ppm as well, which could be assigned to the water in silica on the membrane surface but not in the channels (see analysis by $^1$H{$^{19}$F} REDOR NMR below). The presence of unreacted ethoxyl groups as seen in $^1$H NMR and $^{13}$C NMR of NafSil is not significant for silica in Nafion. The more complete hydrolysis reaction of TEOS could be due to the strongly acidic environment in Nafion. According to Ye et al. [13], a low concentration of ethoxyl groups is desirable for proton transport because the ethoxyl groups may inhibit the formation of hydrogen bonds and block proton hopping pathways on the silica surface.
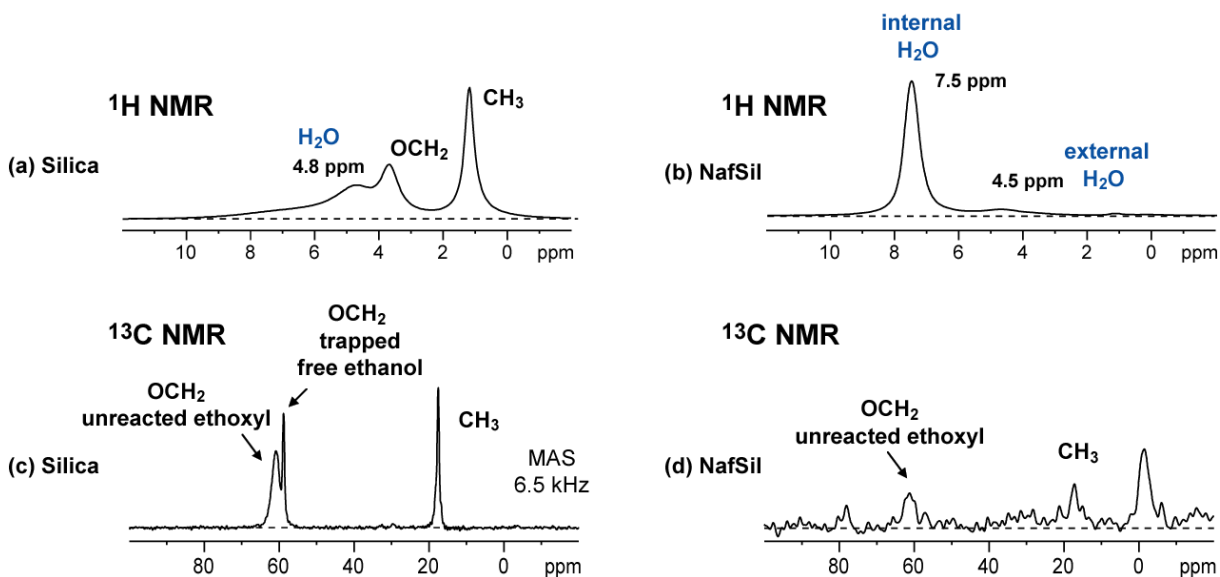


**Figure 6.7.** (a, b) $^1$H spectra (with probehead background suppression) of (a) silica gel and (b) NafSil. (c, d) $^{13}$C cross polarization NMR of (c) silica gel with 1600 scans and (d) NafSil with 14336 scans.

*$^1H\{^{19}F\}$ REDOR.* REDOR experiments measure the strength of dipolar coupling between two spins, which can be affected not only be the internuclear distance but also by molecular motion. For two rigid spins, the strength of the dipolar coupling is proportional to $1/r^3$, where *r* is the internuclear distance; but for mobile spins, the dipolar coupling could be significantly reduced due to motional averaging [27]. When measuring dipolar coupling between OH protons and X nuclei, we must take into account the mobility of $^1H$ spins, which is often associated with water diffusion and proton exchange through hydrogen bonds.

Nafion doped with tetramethylammonium (TMA) cations, namely NafTMA, was first used to test the effectiveness of $^1H\{^{19}F\}$ REDOR. The structure of NafTMA is shown in Figure 6.8a. The TMA cations are attracted by and in close contact with the negatively charged sulfonate side groups of Nafion. The large size of the TMA molecules may have an effect on reducing water diffusion inside Nafion channels. A pair of $^1H\{^{19}F\}$ REDOR spectra with total recoupling time ($Nt_r$) equal to 0.73 ms was shown as an example, where $S_0$ is the spectrum without $^{19}F$ recoupling and S is the recoupled spectrum. In the spectra, the $^1H$ peaks at 6.7 ppm and 3.2 ppm are assigned to water in the channels of Nafion and the $NCH_3$ groups on TMA, respectively. The $^1H\{^{19}F\}$ REDOR dephasing curve of the $NCH_3$ peak suggests a $^1H$-$^{19}F$ distance of around 3 to 4 chemical bonds, since the dephasing rate is comparable to that of the 0.4-nm $^{31}P$-$^{19}F$ distance in NafPhan [28]. The $^1H$ peak of water resonating at 6.7 ppm also shows dephasing, but appears to correspond to a far weaker coupling. As mentioned above, the reduction of the $^1H$-$^{19}F$ dipolar coupling is partly due to the residual water diffusion that has not been total blocked by TMA molecules. Nevertheless, we would not expect to see any $^1H$-$^{19}F$ dipolar coupling for water in Nafion if no TMA was added. The $^1H\{^{19}F\}$ REDOR tested on NafTMA indicates that it could be a useful method to study proton species in the NafSil composite.

For the $^1$H{$^{19}$F} REDOR experiments performed on the NafSil, a small amount of NafTMA was added into the rotor in order to calibrate recoupling pulses. Note that the NafTMA and NafSil are macroscopically separate in the rotor. Also the weak 6.7-ppm $^1$H peak of water in Naf-TMA is negligible. Three peaks are seen in the $^1$H spectrum (Figure 6.8d), with the peaks at 7.7 ppm and 4.5 ppm for Naf-Sil, and the peak at 3.2 ppm for Naf-TMA. As expected, the protons of TMA resonating at 3.2 ppm are coupled to $^{19}$F spins in Nafion. However, for the proton species in NafSil, the coupling to $^{19}$F is too weak to be seen. For the protons resonating at 7.7 ppm, this could be explained by the high mobility of water in Nafion. Unlike TMA molecules that can significantly slow down the water diffusion, the silica particles do not have such negative effect on water diffusion.

For the protons resonating at ~ 4.5 ppm, the interpretation must be different. Since they are the ones associated with adsorbed water on silica surfaces, their mobility is much more limited. The absence of $^1$H-$^{19}$F dipolar coupling suggests that these protons resonating at 4.5 ppm have a $^1$H-$^{19}$F distance beyond 1 or 2 nm; in our case, they are probably outside the water channels and on the surface of the membrane. The presence of an external surface layer of silica has been observed by optical and electron microscopy studies for Nafion-silica composites with high silica concentrations [16]. In fuel cell applications, the surface silica layer may inhibit proton diffusion and reduce the contact area between PEM and electrodes. Therefore, it is better to make a Nafion-silica composite with relatively low silica concentrations or to remove the silica on the surface if possible. For our NafSil sample, the total amount of surface silica is ~ 10%, which does not affect our previous analysis significantly.
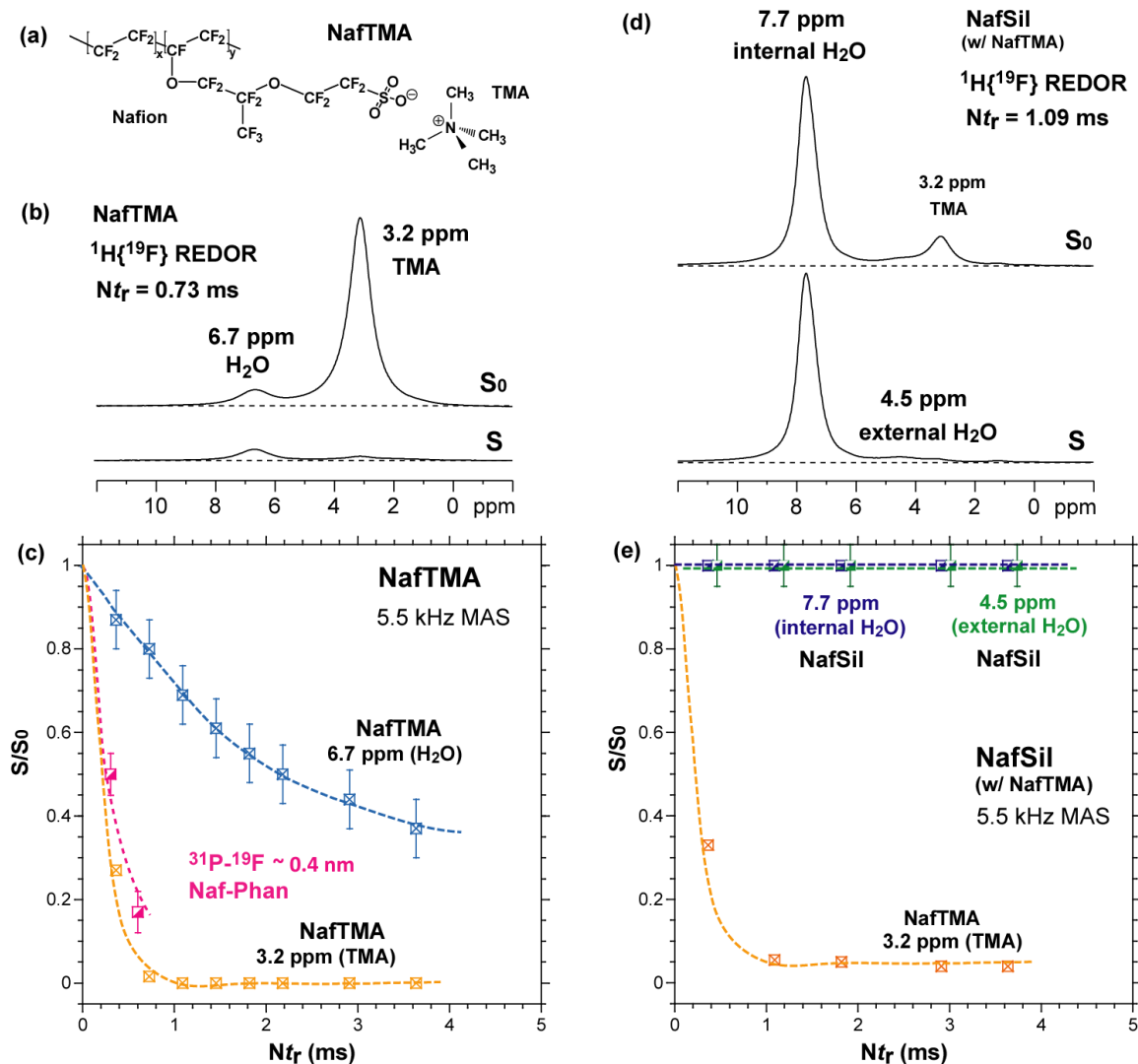
**Figure 6.8.** (a) Structure of NafTMA. (b) $^1$H{$^{19}$F} REDOR $S_0$ and S spectra of NafTMA at total recoupling time (N$t_r$) of 0.73 ms. c) $^1$H{$^{19}$F} REDOR dephasing curve for NafTMA. (d) $^1$H{$^{19}$F} REDOR $S_0$ and S spectra of NafSil (with a small amount of NafTMA) at total recoupling time (N$t_r$) of 1.09 ms. (e) $^1$H{$^{19}$F} REDOR dephasing for Naf-Sil. The $^{31}$P{$^{19}$F} REDOR data of NafPhan were scaled according to the gyromagnetic ratio of $^{31}$P and $^1$H; other dashed lines are guides to the eye.

*$^1H$-$^{29}Si$ HetCor.* The Si-OH groups at the surface of the silica particles can be probed directly through 2D correlation NMR techniques, i.e. $^1H$-$^{29}Si$ heteronuclear correlation (HetCor) NMR, which correlate signals of $^1H$ and $^{29}Si$ spins in spatial proximity. Figure 6.9 shows the $^1H$ cross sections of the surface $Q_3$ silicon sites extracted from 2D $^1H$-$^{29}Si$ HetCor spectra. For pure silica gel, the $^1H$ resonance at 5 ppm, which coincides with the main peak in $^1H$ NMR, is assigned to the Si-OH protons that undergo fast exchange with water. On the left shoulder of the 5-ppm peak, there is a broad $^1H$ resonance, which is assigned to the Si-OH protons that are held by strong hydrogen bonds and are therefore less mobile, namely rigid Si-OH. For the NafSil sample, these two $^1H$ peaks are still present. Based on the previous analysis and the comparison with silica gel, they are most likely to be assigned to the Si-OH protons of the external silica on the membrane surface. The majority of Si-OH protons of the internal silica particles are observed at the proton resonance of 7.5 ppm, which coincides with the major peak in $^1H$ NMR. The apparently increased population of the external Si-OH protons is due to their better cross polarization efficiency. In $^1H$-$^{29}Si$ HetCor, the magnetization is transferred from $^1H$ to $^{29}Si$ by cross polarization, which selectivity enhances the $^{29}Si$ signals with stronger $^1H$-$^{29}Si$ dipolar coupling. Therefore, the $^1H$-$^{29}Si$ HetCor implies a reduced $^1H$-$^{29}Si$ dipolar coupling for the Si-OH groups of internal silica. This is confirmed in the $^{29}Si\{^1H\}$ REDOR curves shown below.
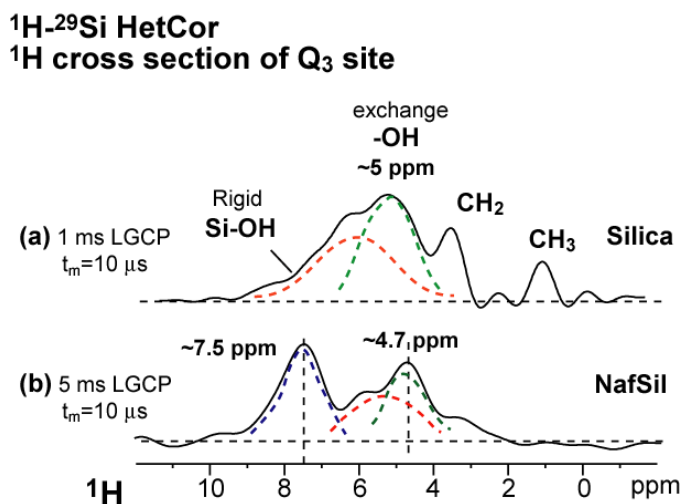
**Figure 6.9.** $^1$H cross section for Q$_3$ sites in $^1$H-$^{29}$Si heteronuclear correlation (HetCor) NMR of (a) pure silica gel and (b) NafSil. The experiments were performed at MAS = 6.5 kHz. The duration of LGCP and the length of mixing time (t$_m$) are labeled to each spectrum. The dashed lines are guides to the eye.

*$^{29}$Si{$^1$H} REDOR.* $^{29}$Si{$^1$H} REDOR experiments with $^{29}$Si magnetization generated from either direct polarization or cross polarization were performed (Figure 6.10). The direct polarization quantitatively selects all $^{29}$Si spins according to their real population, while cross polarization emphasizes those with stronger $^1$H-$^{29}$Si dipolar coupling. Comparing the dephasing rate of DP REDOR curves of surface Q$_3$ sites in silica gel and in NafSil, it is clear that most of Si-OH groups NafSil have much weaker dipolar interaction than those of silica gel. The CP REDOR curves suggest that there are some Si-OH with stronger dipolar coupling in both silica gel and NafSil. However, it must be taken into account that many of the Si-OH with strong $^1$H-$^{29}$Si coupling are from the external silica grown outside the membrane. The dipolar interaction for Si-OH groups of internal silica is indeed weak, which is a result of the increased mobility of Si-OH protons. As for PEM in fuel cells, the proton mobility on the silica surface is favorable for proton transport. This finding may explain the preserved proton conductivity of Nafion-inorganic composites at low hydration levels, since these surface OH groups provide a continuous pathway for proton hopping.
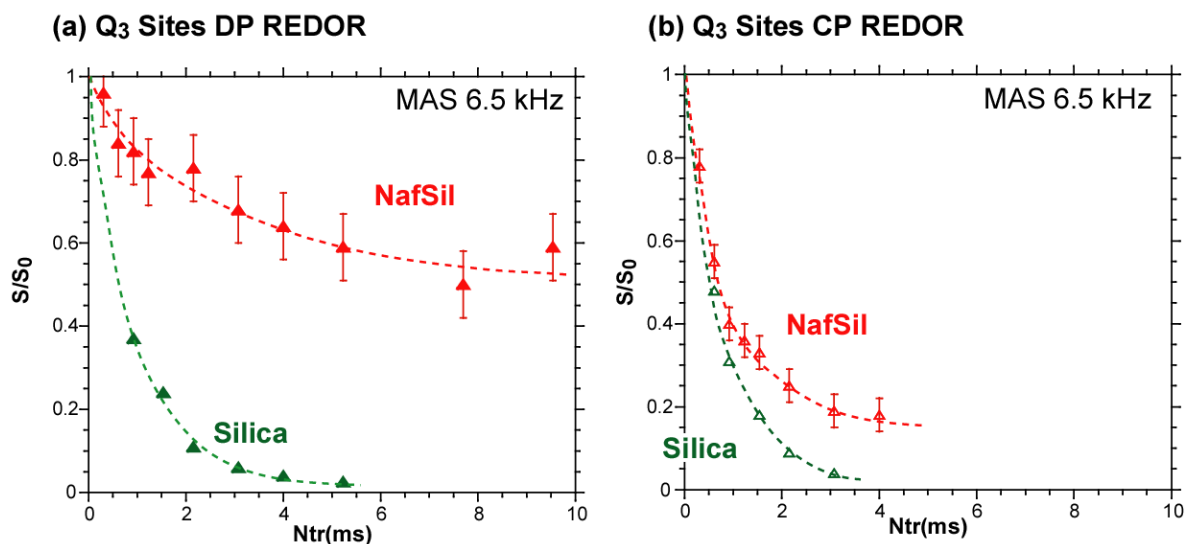
**Figure 6.10.** $^{29}$Si{$^{1}$H} REDOR $S/S_0$ curves of Naf-Sil B and pure silica samples with (a) direct polarization and with (b) cross polarization. REDOR experiments were performed at MAS = 6.5 kHz. The dashed lines are the guides to the eye.

**Conclusions**

Silica and zirconium phosphate grown in the channels of Nafion have been studied by solid-state NMR, XRD, and TGA. Under typical situations with an inorganic volume fraction of around 15%, amorphous silica and disordered ZrP nanoparticles are formed. They are surrounded by a ~ 0.8-nm thick water layer according to the internuclear distances estimated from X{$^{19}$F} REDOR experiments and the high side-group mobility seen in $^{19}$F NMR. The significantly different REDOR dephasing of surface and interior Si sites indicates that the silica particles in Nafion channels have a cylindrical shape, with a cross-section diameter of ~ 2.8 nm derived from the S/V ratio of silica obtained by $^{29}$Si NMR. Based on $^{31}$P NMR, REDOR, and volume fraction of ZrP, an elliptical-cylinder shape with two disordered ZrP layers was proposed for ZrP in Nafion. The silica grown in Nafion has fewer unreacted

ethoxyl groups than silica gel as seen in $^1$H and $^{13}$C NMR. Most of the Si-OH protons of silica in Nafion have increased mobility and exchange with water in Nafion channels as shown by $^1$H-$^{29}$Si HetCor and $^{29}$Si{$^1$H} REDOR NMR. Silica grown on the membrane surface was also detected and confirmed by $^1$H{$^{19}$F} REDOR. The dominance of Si-OH and the increased surface proton mobility on silica grown in Nafion may explain the proton conductivity at low hydration levels.

**References**

(1)    Devanathan, R. *Energy Environ. Sci.* **2008**, *1*, 101-119.

(2)    Mauritz, K. A.; Moore, R. B. *Chem. Rev.* **2004**, *104*, 4535-4585.

(3)    Schmidt-Rohr, K.; Chen, Q. *Nat. Mater.* **2008**, *7*, 75-83.

(4)    Chen, Q.; Schmidt-Rohr, K. *Macromolecules* **2004**, *37*, 5995-6003.

(5)    Chen, Q.; Schmidt-Rohr, K. *Macromol. Chem. Phys.* **2007**, *208*, 2189-2203.

(6)    Yang, C.; Costamagna, P.; Srinivasan, S.; Benziger, J.; Bocarsly, A. B. *J. Power Sources* **2001**, *103*, 1-9.

(7)    Adjemian, K. T.; Lee, S. J.; Srinivasan, S.; Benziger, J.; Bocarsly, A. B. *J. Electrochem. Soc.* **2002**, *149*, A256-a261.

(8)    Casciola, M.; Capitani, D.; Comite, A.; Donnadio, A.; Frittella, V.; Pica, M.; Sganappa, M.; Varzi, A. *Fuel Cells* **2008**, *8*, 217-224.

(9)    Young, S. K.; Jarrett, W. L.; Mauritz, K. A. *Polymer* **2002**, *43*, 2311-2320.

(10)   Deng, Q.; Cable, K. M.; Moore, R. B.; Mauritz, K. A. *J. Polym. Sci., Part B: Polym. Phys.* **1996**, *34*, 1917-1923.

(11) Truffier-Boutry, D.; De Geyer, A.; Guetaz, L.; Diat, O.; Gebel, G. *Macromolecules* **2007**, *40*, 8259-8264.

(12) Rodgers, M. P.; Shi, Z.; Holdcroft, S. *Fuel Cells* **2009**, *9*, 534-546.

(13) Ye, G.; Hayden, C. A.; Goward, G. R. *Macromolecules* **2007**, *40*, 1529-1537.

(14) Nicotera, I.; Zhang, T.; Bocarsly, A.; Greenbaum, S. *J. Electrochem. Soc.* **2007**, *154*, B466-B473.

(15) Yang, C.; Srinivasan, S.; Bocarsly, A. B.; Tulyani, S.; Benziger, J. B. *J. Membr. Sci.* **2004**, *237*, 145-161.

(16) Mauritz, K. A.; Stefanithis, I. D.; Davis, S. V.; Scheetz, R. W.; Pope, R. K.; Wilkes, G. L.; Huang, H. H. *J. Appl. Polym. Sci.* **1995**, *55*, 181-190.

(17) Bennett, A. E.; Rienstra, C. M.; Auger, M.; Lakshmi, K. V.; Griffin, R. G. *J. Chem. Phys.* **1995**, *103*, 6951-6958.

(18) Gullion, T.; Schaefer, J. *J. Magn. Reson.* **1989**, *81*, 196-200.

(19) Sinha, N.; Schmidt-Rohr, K.; Hong, M. *J. Magn. Reson.* **2004**, *168*, 358-365.

(20) Bielecki, A.; Burum, D. P.; Rice, D. M.; Karasz, F. E. *Macromolecules* **1991**, *24*, 4820-4822.

(21) vanRossum, B. J.; Forster, H.; deGroot, H. J. M. *J. Magn. Reson.* **1997**, *124*, 516-519.

(22) Hou, S. S.; Beyer, F. L.; Schmidt-Rohr, K. *Solid State Nucl. Magn. Reson.* **2002**, *22*, 110-127.

(23) Trebosc, J.; Wiench, J. W.; Huh, S.; Lin, V. S. Y.; Pruski, M. *J. Am. Chem. Soc.* **2005**, *127*, 3057-3068.

(24) Hench, L. L.; West, J. K. *Chem. Rev.* **1990**, *90*, 33-72.

(25) Devreux, F.; Boilot, J. P.; Chaput, F.; Lecomte, A. *Phys. Rev. A: At. Mol. Opt. Phys.* **1990**, *41*, 6901-6909.

(26) Zhuravlev, L. T. *Colloids Surf., A* **2000**, *173*, 1-38.

(27)    Schmidt-Rohr, K.; Spiess, H. W. *Multidimensional Solid-state NMR and Polymers* Academic Press Limited **1994**.

(28)    Kong, X.; Wadhwa, K.; Verkade, J. G.; Schmidt-Rohr, K. *Macromolecules* **2009**, *42*, 1659-1664.

# Chapter 7

## Characterizations of Zirconium Phosphate and Nafion Zirconium Phosphate Composite by Solid State Nuclear Magnetic Resonance

Xueqian Kong and Klaus Schmidt-Rohr

To be submitted to *Chem. Mat.*

**Abstract**

Nafion zirconium phosphate composites and neat zirconium phosphate (ZrP) were studied by solid state NMR. ZrP made from $ZrOCl_2$ and $H_3PO_4$ has a hydrated $\alpha$-type structure, as supported by X-ray diffraction and a -18.8 ppm resonance at ^{31}P NMR. The structure converted primarily into anhydrous $\alpha$-ZrP after drying at 150°C; other structural changes, e.g. formation of pyrophosphate with ^{31}P resonance at -33.6 ppm were also found. In the fresh sample of ZrP formed in Nafion, a component similar to $\alpha$-ZrP was detected; but other major $(HO)P(OZr)_3$ groups with a ^{31}P peak resonating at -22.2 ppm are also present, and participate in fast proton exchange as suggested by their weak [1]H-^{31}P dipolar coupling. The $\alpha$-ZrP formed in the fresh sample is metastable, converting into the phosphate species resonating at -22.2 ppm after a period of drying. The main ^{31}P peak at -22.2 ppm in the composite has a relatively short $T_1$ relaxation time and weak [1]H-^{31}P dipolar coupling, indicating that the protons on the POH sites is involved in fast proton exchange between POH and $H_2O$.

**Introduction**

Zirconium phosphates, with a common layered crystalline structure of α-type, have interesting ion exchange and catalytic properties [1, 2]. The α-type zirconium phosphate with water of hydration (α-ZrP • $H_2O$) can prepared from the reaction between $Zr(OCl)_2$ and $H_3PO_4$ solutions. As determined by X-ray diffraction, α-ZrP • $H_2O$ has a layered structure made up of $(HO)P(OZr)_3$ groups and a long period of 7.56 Å. [3] When the temperature is increased to ~ 110°C, α-ZrP • $H_2O$ starts to lose water and form anhydrous α-ZrP. [4] At higher temperatures, the phosphate layers begin to condense and form pyrophosphate structures (P-O-P). [4, 5] Between the phase transitions, ZrP may form a complex of different crystalline structures or become amorphous [4], which makes the XRD pattern hard to interpret. In these situations, solid-state NMR is a particularly powerful tool to investigate the structural changes. In the first part of this paper, comprehensive $^1H$ and $^{31}P$ NMR characterizations were performed on some ZrP samples including α-ZrP • $H_2O$.

Recently, zirconium phosphate has been employed to make composite polymer membranes for fuel cell applications, e.g. Nafion ZrP composite, because of its proton conductivity and hygroscopic nature [6, 7]. The ZrP particles in the hydrophilic channels of Nafion help Nafion withstand higher working temperatures (> 100°C) and lower hydration levels [8, 9]. Analytical techniques, such as X-ray diffraction, small-angle X-ray scattering, and NMR [10, 11, 12], have been used to study the structure and proton transport of Nafion ZrP composite. It has been found that though some α-ZrP and its derivatives may be present in the composite, much of the ZrP appears amorphous and its structure and composition is not fully understood [13]. In the second part of this paper, ZrP inside Nafion, including a metastable fresh form and a stable form under dry condition, was characterized by $^{31}P$ NMR and 2D $^1H$-$^{31}P$, $^{31}P$-$^{31}P$ correlation NMR experiments.

**Experimental**

*Preparation of composite membrane.* Nafion 117 membrane was boiled first in 0.5 M $H_2SO_4$ for 2 hrs and then in deionized $H_2O$. It was then dried in vacuum at room temperature and kept in a desiccator for weeks. Pre-treated Nafion was later swelled in Ethanol/Water (50:50 in volume) at $80^oC$ for 3 hrs. Then Nafion was immersed in 1M $ZrOCl_2$ solution at $80^oC$ for 2 hrs, followed by immersion in 1M $H_3PO_4$ at $80^oC$ for 17 hrs. After that, it was boiled in deionized $H_2O$ for 4 hrs to remove excess acid and solvent. The composite membrane was dried in vacuum at $105^oC$ for 21 hrs. The original sample was immediately packed in a NMR rotor, "fresh NafZrP", and the rest was kept in a desiccator for about six months, "dry NafZrP".

*Preparation of pure zirconium phosphate.* 0.3 M $ZrOCl_2$ solution was mixed with 1 M $H_3PO_4$ solution at $80^oC$ for 24 hrs, which gave white ZrP precipitations. Then, the precipitations were washed with 2% $H_3PO_4$ and filtered. After that, it was dried in vacuum at $105^oC$ for 24 hrs. The fresh sample was immediately packed in a NMR rotor, "fresh ZrP", and the rest was later heated at $150^oC$, "heated ZrP".

Rehydrated samples were made by placing the dry samples in a chamber at 100% humidity for several days.

**Table 7.1.** List of samples

| Pure ZrP | Sample description | NafZrP | Sample description |
|---|---|---|---|
| fresh ZrP | Crystalline α-ZrP | fresh NafZrP | Fresh sample tested soon after preparation |
| heated ZrP | Heated ZrP at $150^oC$ | dry NafZrP | Dried in desiccator for 6 months |

*NMR parameters.* NMR experiments were performed on a Bruker DSX-400 spectrometer at a resonance frequency of 400 MHz for ^{1}H, 376 MHz for ^{19}F, 162 MHz for ^{31}P, using double-resonance or triple-resonance magic angle spinning (MAS) probes. [19]F experiments were performed in 2.5-mm rotors at 30 kHz. [1]H single-pulse excitation experiments with background suppression [14] were performed in 4-mm rotors at 6.5 kHz. [31]P experiments were performed in 4-mm rotors at 6.5 kHz or 8 kHz with variable recycle delays. Contact times of 1 ms were used for ^{31}P cross polarization (CP) experiments from [1]H. Two-pulse phase-modulation (TPPM) [15] was used for [1]H-^{31}P heteronuclear dipolar decoupling. All experiments were carried out at ambient temperature.

[1]H recoupled dipolar dephasing before ^{31}P detection after direct polarization was used to characterize the [1]H-^{31}P dipolar coupling strength of spectrally resolved ^{31}P sites. It utilizes rotation-synchronized [1]H 180° pulses to recouple ^{1}H dipolar interaction with ^{31}P during the ^{31}P echo sequence. Total recoupling times of two rotor periods (2 $t_r$) were used.

[1]H-[31]P HetCor and WISE. Two-dimensional (2D) [1]H-^{31}P heteronuclear correlation (HetCor) [16] and wide-line separation (WISE) NMR experiments [17] were performed at $\upsilon_r$ = 6250 Hz. In [1]H-[31]P HetCor experiments, frequency-switched Lee-Goldburg (FSLG) homonuclear decoupling [18] was applied during the evolution period $t_1$; while in [1]H-^{31}P WISE experiments, no decoupling was employed during $t_1$ evolution so that magnetizations from strongly coupled protons were suppressed. Cross polarization contact times of 1 ms and mixing times of 50 μs were used.

[31]P-[31]P 2D exchange. [31]P-[31]P 2D exchange experiments were performed at 6250-Hz MAS. [31]P magnetization was generated through direct polarization with 1 s recycle delay. The spin diffusion mixing time was 1 s.

*Thermogravimetric analysis measurement.* A TA Instruments[®] Q50 thermogravimetric analyzer (TGA) was used to obtain the thermograph of the composite membrane. The sample was heated from ambient to 630$^o$C at a rate of 10$^o$/min under constant air flow.

*X-ray diffraction.* Powder X-ray diffraction measurements were performed on a Scintag XDS 2000 diffractometer using a quartz substrate. The X-ray source of Cu Kα was used with a wavelength of 1.5418 Å.

**Results and Discussion**

***Pure zirconium phosphate***

*X-ray diffraction.* For fresh ZrP, the XRD pattern is characteristic of an α-crystalline morphology[3]. After heating the sample to 150$^o$C, diffraction peaks of anhydrous α-ZrP at 2θ = 12$^o$, 20$^o$, 25$^o$, 34$^o$ are expected[4]. However, many additional signals are detected. Some peaks could be assigned to zirconium pyrophosphate α-$ZrP_2O_7$ [19], and the existence of pyrophosphate groups will be proven in $^{31}$P NMR. Additional minor diffraction peaks between 20$^o$ to 30$^o$ are not assigned. These unknown peaks do not match typical crystalline structures (β, γ, τ, and ρ) of ZrP in the database of the International Centre for Diffraction Data[®].
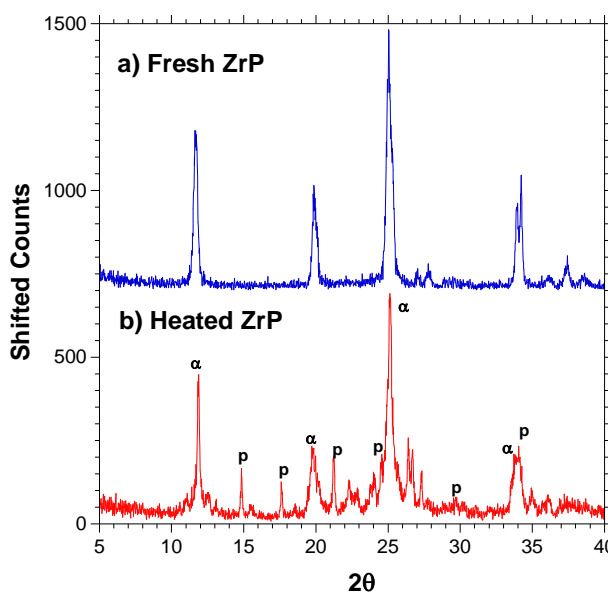
**Figure 7.1.** X-ray diffraction pattern of a) fresh ZrP, and b) heated ZrP. In b), The diffraction peaks assigned to anhydrous α-ZrP are labeled with "α"; and those assigned to α-Zr(P$_2$O$_7$) are labeled with "p".

*$^{31}$P and $^1$H NMR.* In the directly polarized $^{31}$P spectra (Figure 7.2c), the fresh ZrP has two $^{31}$P resonances at 0 ppm and -18.8 ppm, respectively. The -18.8 ppm peak is the characteristic resonance of HOP(OZr)$_3$ in crystalline α-ZrP with water of crystallization [20]. The peak at 0 ppm is from residual H$_3$PO$_4$. Spectra after recoupled $^1$H-$^{31}$P dipolar dephasing give indications of the coupling strength of $^{31}$P sites to their surrounding protons. Those $^{31}$P signals with a relatively strong $^1$H-$^{31}$P dipolar interaction will be dephased in the recoupled spectra, as observed for fresh ZrP. The observed $^1$H-$^{31}$P coupling of HOP(OZr)$_3$ sites in fresh ZrP suggest a relatively slow proton-exchange process between these POH sites and mobile H$_2$O. The $^1$H-$^{31}$P coupling of POH groups for residual H$_3$PO$_4$ is too weak to be observed, which suggests fast dynamics. The downfield $^1$H resonance at 9.7 ppm (Figure 7.2a) mostly comes from the protons of residual H$_3$PO$_4$. The $^1$H resonances of HOP(OZr)$_3$ and water of crystallization are not clearly seen in $^1$H spectrum due to their lower intensity. However, these $^1$H resonances will become observable in the $^1$H-$^{31}$P 2D correlation NMR (Figure 7.3a).

After the original ZrP was dried at $150^{\circ}$C, the main $^{31}$P peak for HOP(OZr)$_3$ shifted to -21.3 ppm, which is the known $^{31}$P resonance for anhydrous $\alpha$-ZrP. It suggests a transition between $110^{\circ}$C and $150^{\circ}$C at which Zr(HPO$_4$)$_2$ H$_2$O converts into anhydrous Zr(HPO$_4$)$_2$. Pyrophosphate species (P-O-P) formed by condensation of two phosphate layers were detected at a $^{31}$P resonance position of -33.6 ppm. Tentative assignments of minor $^{31}$P resonances are listed in Table 7.2. The $^1$H resonances at 10.1, 7.3 and 0.7 ppm of heated ZrP should be assigned to the protons of residual H$_3$PO$_4$, of the HOP(OZr)$_3$ groups on ZrP, and of isolated POH groups, respectively. This will be shown more clearly in $^1$H-$^{31}$P 2D correlation experiments.
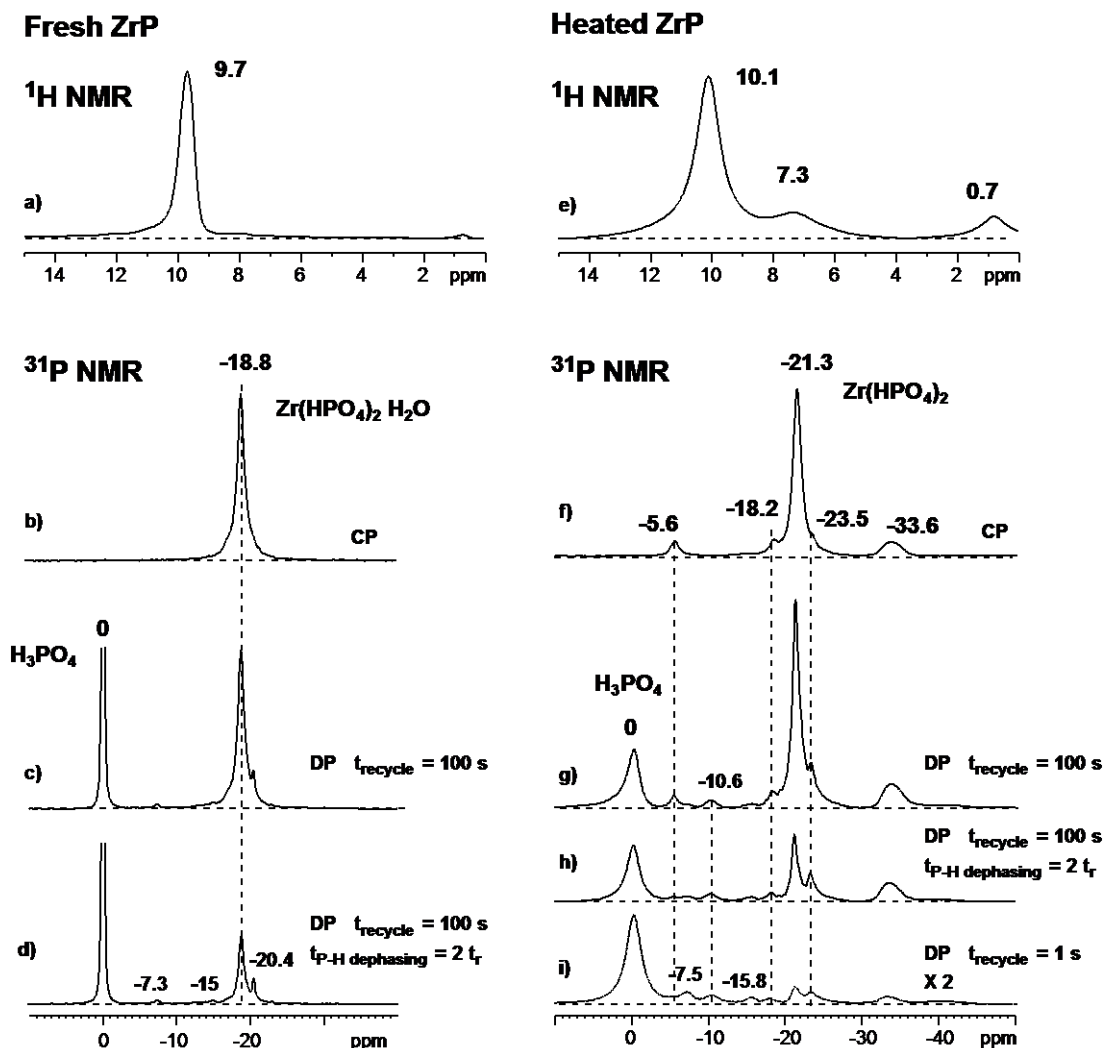
**Figure 7.2.** a) $^{1}$H spectra of a) fresh ZrP and e) heated ZrP. $^{31}$P CP spectra of b) fresh ZrP and f) heated ZrP with 1-ms contact time. $^{31}$P DP spectra of c) fresh ZrP and g) heated ZrP with 100-s recycle delay; $^{31}$P DP spectra of d) fresh ZrP and h) heated ZrP after $^{1}$H-$^{31}$P dipolar dephasing for $2t_r$. $^{31}$P DP spectrum of i) heated ZrP with 1-s recycle delay and its intensity was doubled for clarity. Spinning frequency = 8 kHz.

*$^{1}$H-$^{31}$P WISE and HetCor.* $^{1}$H-$^{31}$P wide-line separation (WISE) experiments can correlate signals of $^{1}$H and $^{31}$P spins that are coupled by significant dipolar interaction. The spectrum of fresh ZrP (Figure 7.3a) shows that the $^{31}$P site of α-Zr(HPO$_4$)$_2$ • H$_2$O at -18.8 ppm correlates to three different $^{1}$H spins. The $^{1}$H peaks at 8.8 ppm and 3.8 ppm are assigned to

the protons on POH groups of $\alpha$-ZrP and water of crystallization, respectively. The $^1$H signal at 9.7 ppm is from residual $H_3PO_4$. The correlation between $^{31}$P sites in $\alpha$-ZrP and $^1$H in $H_3PO_4$ suggests that the residual $H_3PO_4$ is in close contact with ZrP, probably between the ZrP layers.

The WISE spectrum of heated ZrP (Figure 7.3b) shows two major correlation peaks. One at -21.3 ppm of $^{31}$P is assigned to POH groups in anhydrous $\alpha$-ZrP, while the other at -33.8 ppm of $^{31}$P is assigned to pyrophosphates that have isolated POH attached. Similar to $^1$H-$^{31}$P WISE, $^1$H-$^{31}$P HetCor can correlate dipolar coupled proton and phosphorus spins. $^1$H-$^{31}$P HetCor may achieve better resolution with $^1$H-$^1$H homonuclear decoupling during the $t_1$ evolution period. On the other hand, the ppm values of the peaks are less certain, due to a spectral scaling factor. Besides the main cross peak between the $^{31}$P resonance at -21.3 ppm and the $^1$H resonance at 7.3 ppm, some residual $\alpha$-ZrP can be observed with a $^{31}$P resonance at -18.8 ppm and a $^1$H resonance at 8.5 ppm. The cross peak with the $^{31}$P resonance at -5.6 ppm and the $^1$H resonance at 9.3 ppm is assigned to $(HO)_2P(OZr)_2$. Isolated POH groups with a $^1$H resonance at 0.7 ppm are associated with the $^{31}$P peaks of $(HO)P(OZr)_3$ at -24.5 ppm and of $(HO)_2P(OZr)_3$ at -7.5 ppm, and the $^1$H peak is also coupled to the $^{31}$P peak of pyrophosphate (P-O-P) groups at -33.6 ppm. Combined with the correlation peaks observed in $^{31}$P 2D exchange NMR, these $^{31}$P resonances should be assigned to the phosphorus in partially condensed ZrP layers, where isolated POH with $^{31}$P resonances at -7.5 ppm and -24.5 ppm are present close to condensed pyrophosphate P-O-P. The $^{31}$P resonance at -15.8 ppm correlates to $^1$H resonances at both 0.7 ppm and 7.3 ppm, it could be assigned to $(HO)_2P(OZr)_2$ groups that are next to those isolated POH sites resonating at 24.5 ppm, though the cross peaks between them are not detected in $^{31}$P 2D exchange NMR (Figure 7.4) possibly due to the low intensity.
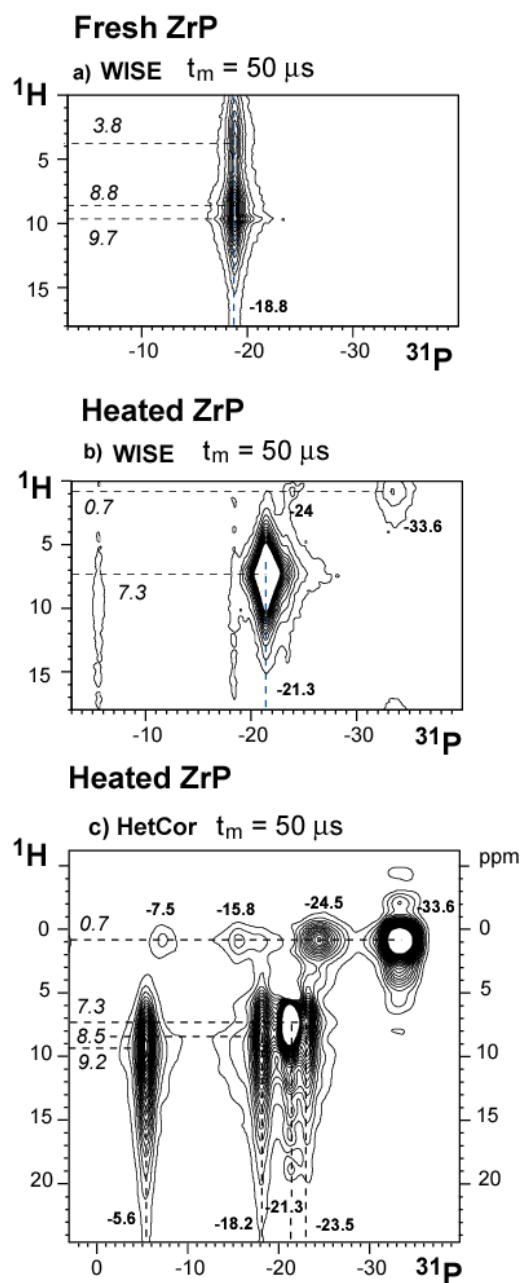
**Figure 7.3.** $^{1}$H-$^{31}$P WISE of a) fresh ZrP and b) heated ZrP with a mixing time of 50 μs. c) $^{1}$H-$^{31}$P HetCor of heated ZrP with a mixing time of 50 μs. $^{1}$H chemical shifts are labeled in italics, and $^{31}$P chemical shifts are label in bold.

*$^{31}$P 2D Exchange NMR.* In order to identify different local environments in the heated ZrP sample, $^{31}$P 2D exchange experiments were performed with direct polarization. The cross

peaks indicate spin or chemical exchange between $^{31}$P sites that are spatially close. In the $^{31}$P 2D exchange spectrum with direct polarization, five sets of local environments can be seen from the cross peaks: the $^{31}$P resonances at -18.2, -5.6, and -23.5 ppm, which is remaining α-Zr(HPO$_4$)$_2$ • H$_2$O and its derivatives; the $^{31}$P resonances at -33.6, -7.5, and -24.5 ppm, which are condensed pyrophosphates and isolated POHs in the partially layers; the $^{31}$P resonance at -21.3 ppm, the anhydrous α-ZrP; $^{31}$P resonance at -15.8 ppm of (HO)$_2$P(OZr)$_2$; and $^{31}$P resonance at -17 ppm whose origin is not clear. The tentative assignments of $^{31}$P peaks in the heated ZrP sample are listed in Table 7.2.
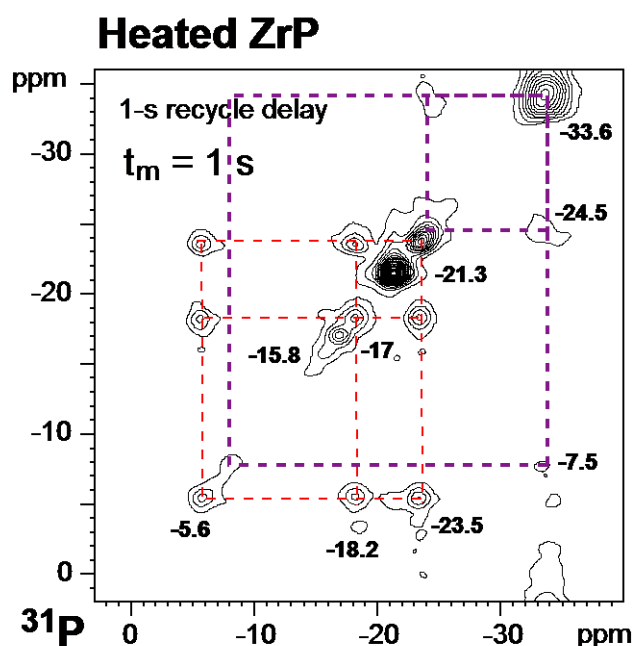


**Figure 7.4.** $^{31}$P directly polarized 2D exchange of heated ZrP with 1-s recycle delay and 1-s mixing time. MAS spinning frequency = 6250 Hz.

**Table 7.2.** Chemical shifts and compositions of local structures in the heated ZrP.

| $\delta\,(^{31}P)$ | $\delta\,(^{1}H)$ | Fraction | Assignments and comments | Possible structure |
|---|---|---|---|---|
| **-21.3** | *7.3* | 44% | $(HO)P(OZr)_3$; anhydrous $\alpha$-ZrP | Anhydrous $\alpha$- $Zr(HPO_4)_2$ |
| **-18.2** | *8.8* | 11% | $(HO)P(OZr)_3$; $\alpha$-ZrP | $\alpha$-$Zr(HPO_4)_2 \cdot H_2O$ and |
| **-23.5** | *7.3* | | $(HO)P(OZr)_3$ | derivatives |
| **-5.6** | *9.2* | | $(HO)_2P(OZr)_2$ | |
| **-33.6** | *(0.7)* | 18% | $(OZr)_3P-O-P(OZr)_3$ pyrophosphate | Partially condensed ZrP |
| **-24.5** | *0.7* | | Isolated $(HO)P(OZr)_3$ | layers |
| **-7.5** | *0.7* | | Isolated $(HO)_2P(OZr)_2$ | |
| **0** | *10.1* | 24% | Residual $H_3PO_4$ | Residual phosphoric acid |
| **-15.8** | *0.7, 7.3* | 1% | $(HO)_2P(OZr)_2$ | Next to isolated POH |
| **-10.6** | *N/A* | 2% | ? $(HO)_2P(OZr)_2$ | Unknown |
| **-17** | *N/A* | < 1% | ? $(HO)P(OZr)_3$ | Unknown |

*Nafion ZrP Composites*

*Thermogravimetric analysis.* A sample NafZrP was tested by thermogravimetric analysis to measure the ZrP uptake of the composite membrane. The sample was heated from $30^oC$ to $630^oC$ under a constant flow of air. From room temperature to $\sim 300\ ^oC$, the composite lost absorbed water and phosphoric acid. Then the Nafion membrane started to decompose. At around $500\ ^oC$, the membrane had decomposed completely; no membrane residue remains, since oxygen in the air flow oxidizes all carbon species. The $\sim 18\ \%$ residual mass (20% of dry mass) comes from condensed ZrP. The molar ratio (Zr : P : $-SO_3^-$) is 1 : 2 : 1.3.
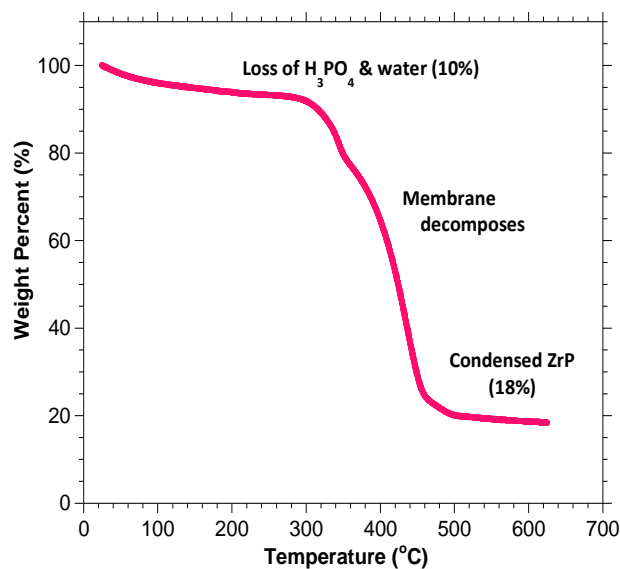
**Figure 7.5.** TGA measurement of NafZrP

*X-ray diffraction.* The X-ray diffraction of a NafZrP sample shows that most of the ZrP inside Nafion is disordered. Also, the diffraction peak which indicates the packing of Nafion backbone is much broader in NafZrP composite than in pure Nafion. The polymer crystallinity in NafZrP composite is poorer than Nafion itself, which suggests that the ZrP strongly interacts with Nafion matrix.
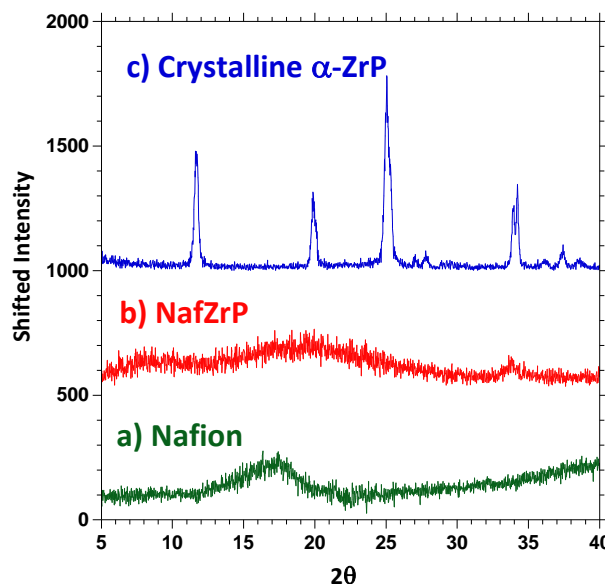
**Figure 7.6.** X-ray diffraction pattern of a) Nafion b) NafZrP and c) $\alpha$-ZrP.

*$^{31}$P and $^{1}$H NMR.* $^{31}$P NMR experiments were performed on fresh NafZrP and dry NafZrP, a sample dried in a desiccator for more than six months. Compared to pure ZrP, no $^{31}$P peak at 0 ppm is seen, which suggests that $H_3PO_4$ has been removed completely from the composite membrane. The $^{1}$H resonance at around 7 ppm should mostly come from $H_2O$ in the membrane. In both NafZrP samples, $^{31}$P spectra with cross polarization are dramatically different from those with direct polarization, which suggests a big variation of $^{1}$H-$^{31}$P dipolar coupling strength for these $^{31}$P sites. The -17.6, -19.3 and -21.3 ppm peaks in fresh NafZrP have relatively strong $^{1}$H-$^{31}$P dipolar couplings as they dominate in the CP spectrum and can be dephased by $^{1}$H recoupling in the DP spectrum. The other major $^{31}$P peak at -22.2 ppm, which accounts for 40% of total $^{31}$P species, has a weak $^{1}$H-$^{31}$P dipolar coupling, as do the $^{31}$P peaks at -6.7 and -14.5 ppm. The reduced $^{1}$H-$^{31}$P dipolar coupling is due to the exchange of POH protons with those in $H_2O$, which is confirmed by their reduced $^{31}$P $T_1$ relaxation times compared to fresh ZrP. Here, the $T_1$ relaxation time is related to the fluctuation of local magnetic field; a shorter $T_1$ implied a more dynamic local environment. The $^{31}$P resonance at

-28.2 ppm with a relatively long $T_1$ is a characteristic peak for non-protonated $^{31}P$ sites in P(OZr)$_4$.

In the dry NafZrP sample, the structure of ZrP has changed significantly. The $^{31}P$ resonance at -22.2 ppm, whose fraction has increased to 80%, dominates the spectrum and it should account for the major disordered ZrP in Nafion as suggested by XRD. Its $^1$H-$^{31}$P dipolar coupling has been increased after drying. The peaks at -17.6, -19.3 and -21.3 ppm disappear and a new $^{31}P$ resonance at -20.4 ppm shows a strong $^1$H-$^{31}$P dipolar coupling. The $^{31}P$ peaks at -6.7, -14.5 and -28.2 ppm remain but the $^{31}P$ peak at -14.6 ppm also show an increase of $^1$H-$^{31}$P dipolar coupling as seen in $^1$H recoupled $^{31}P$ spectra. The recoupled spectrum (Figure 7.7h) and $T_1$ relaxation times (Table 7.3) suggest that the $^1$H-$^{31}$P dipolar coupling strength of the $^{31}P$ resonances at -22.2, -14.5, and -6.7 ppm is still weak as that in fresh NafZrP. However, we notice that about half of the HOP(OZr)$_3$ sites resonating at -22.2 ppm in the dry NafZrP sample do have observable $^1$H-$^{31}$P coupling shown as the reduced intensity of 50% in the recoupled spectrum (Figure 7.7h). It may imply that half of these HOP(OZr)$_3$ sites can access $H_2O$, while the rest cannot. The tentative assignments of the $^{31}P$ sites are also listed in the Table 7.4.
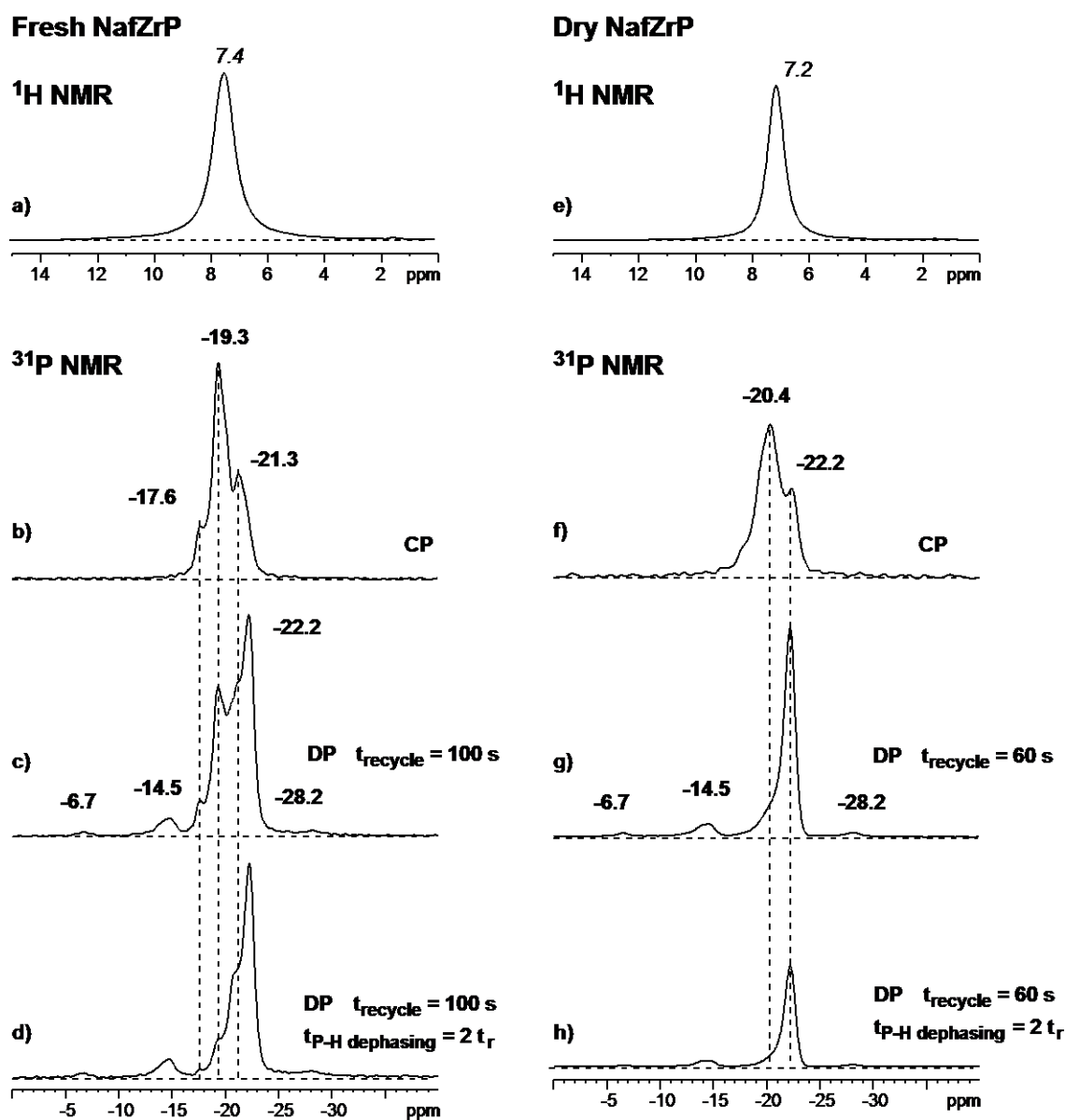
**Figure 7.7.** a) $^1$H spectra of a) fresh NafZrP and e) dry NafZrP. $^{31}$P CP spectra of b) fresh NafZrP and f) dry NafZrP with 1-ms contact time. $^{31}$P DP spectra of c) fresh NafZrP and g) dry NafZrP with 100-s recycle delay; $^{31}$P DP spectra of d) fresh NafZrP and h) dry NafZrP after $^1$H-$^{31}$P dipolar dephasing for $2t_r$. MAS spinning frequency = 6.5 kHz.

**Table 7.3.** T$_1$ relaxation time and assignment of $^{31}$P sites in pure ZrP and NafZrP composites.

| δ ($^{31}$P) | -6.7 ppm | -14.5 ppm | -19.3 ppm | -22.2 ppm | -28.2 ppm |
|---|---|---|---|---|---|
| fresh ZrP | - | - | 19.2 s | - | - |
| fresh NafZrP | 0.8 s | 3.1 s | 12.3 s | 8.3 s | 41.8 s |
| dry NafZrP | 0.8 s | 2.2 s | - | 5.9 s | 35.6 s |
| $^{31}$P sites | (HO)$_2$P(OZr)$_2$ | (HO)$_2$P(OZr)$_2$ | HOP(OZr)$_3$ | HOP(OZr)$_3$ | P(OZr)$_4$ |

*$^1$H-$^{31}$P HetCor and WISE.* The correlations of $^{31}$P sites and $^1$H sites in the fresh NafZrP sample were studied by $^1$H-$^{31}$P HetCor and WISE. One should note that HetCor and WISE can only observe $^{31}$P sites with relatively strong $^1$H-$^{31}$P dipolar coupling because cross polarization is used in these pulse sequences. The $^{31}$P peaks at -17.6 and -19.3 ppm in fresh NafZrP both correlate to $^1$H peaks at 3.8 ppm, which should be assigned to water of crystallization as in pure α-ZrP. The $^{31}$P peak at -21.3 ppm should be assigned to $^{31}$P in anhydrous α-ZrP. These assignments were confirmed by $^1$H-$^{31}$P WISE and $^1$H CSA-filtered WISE experiments. In $^1$H-$^{31}$P WISE spectrum, the $^{31}$P peak of residual α-ZrP at -19.3 ppm correlates to a $^1$H peak of POH at 8.5 ppm, a $^1$H peak of water of crystallization at 3.8 ppm, and a $^1$H peak of membrane water at 7.4 ppm. The membrane water has large motional freedom, so it has a smaller CSA and dominates in the $^1$H CSA-filtered WISE spectrum. In the $^1$H-$^{31}$P WISE spectrum of the dry NafZrP sample, the $^{31}$P peak at -20.4 ppm correlates to a $^1$H resonance with large CSA. This cross peak could be assigned to a HOP(OZr)$_3$ site that is in a relatively dry environment with little contact to membrane water. The dominant $^{31}$P peak at -22.2 ppm is associated with the $^1$H peak of membrane water at 7.0 ppm.
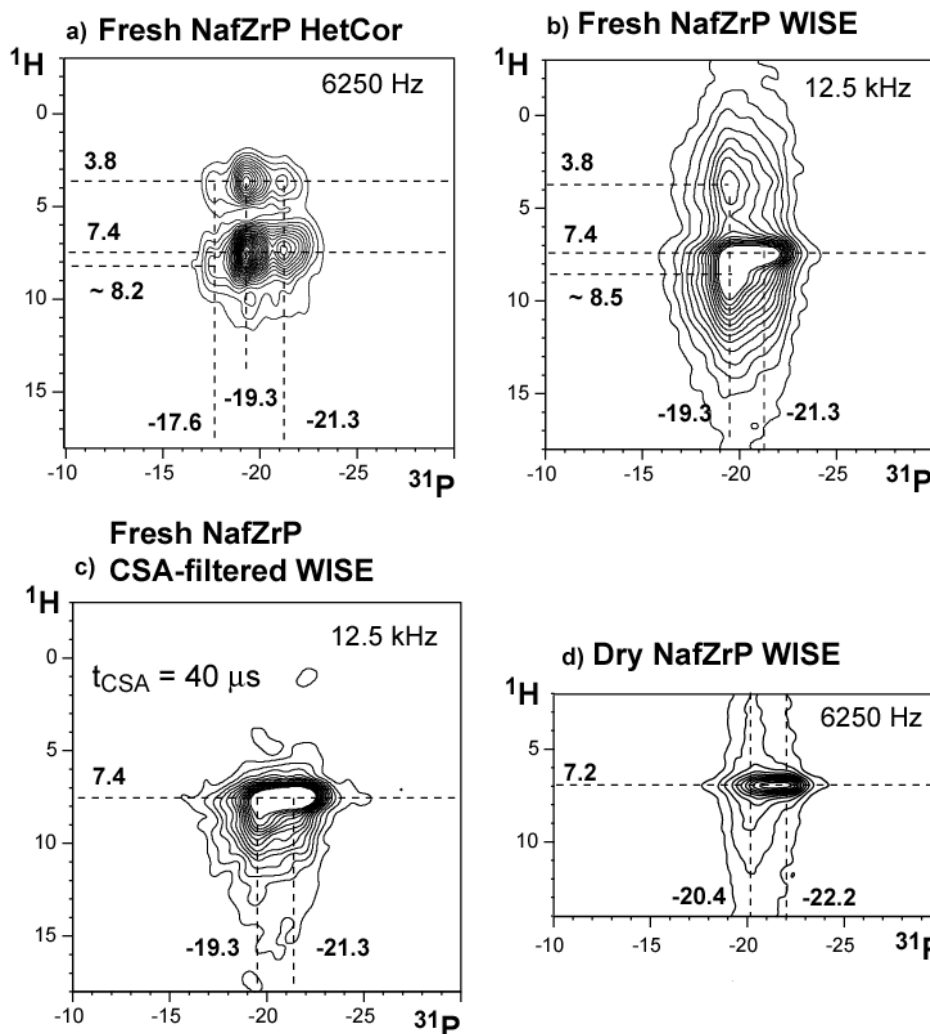
**Figure 7.8.** a) $^1$H-$^{31}$P HetCor spectrum of fresh NafZrP. b) $^1$H-$^{31}$P WISE and c) $^1$H CSA-filtered WISE spectra of fresh NafZrP. d) $^1$H-$^{31}$P WISE spectrum of dry NafZrP. The spin diffusion mixing times are 50 µs and the MAS spinning frequencies are either 6250 Hz or 12.5 kHz.

*$^{31}$P 2D exchange NMR.* $^{31}$P exchange spectra of fresh NafZrP and dry NafZrP were acquired with direct polarization (DP exchange) and 1-s mixing time. A $^{31}$P exchange experiment after cross polarization was also performed on the fresh NafZrP sample to study the proximity of $^{31}$P sites with strong $^1$H-$^{31}$P dipolar coupling. The recycle delays were set at 1 s in order to enhance the signals of the less abundant $^{31}$P species with short $T_1$ relaxation times.
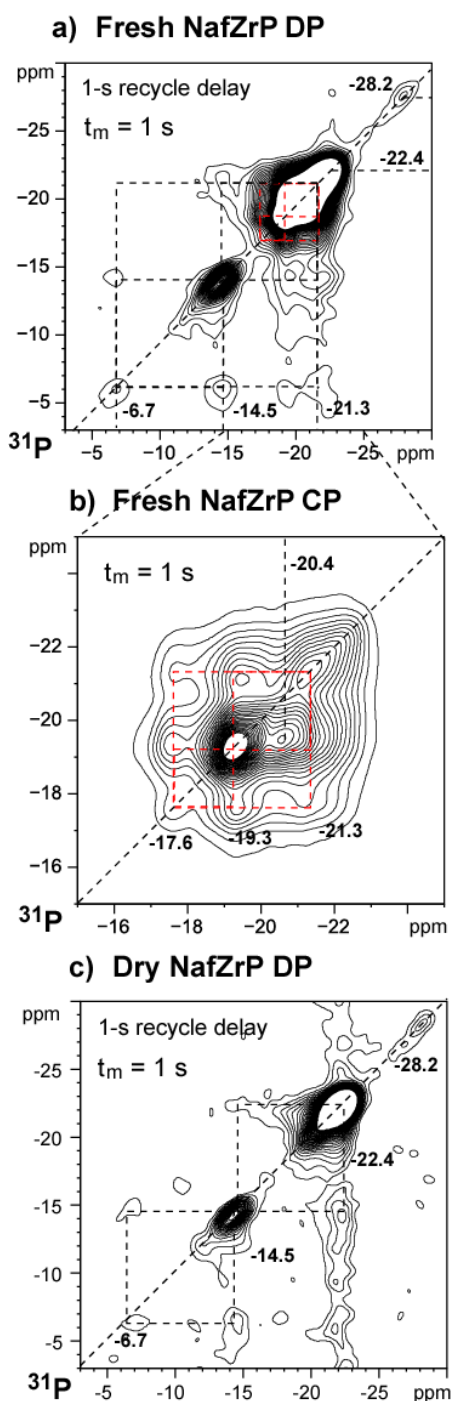
**Figure 7.9.** $^{31}$P exchange spectra of fresh NafZrP a) with direct polarization and 1-s recycle delay, b) with cross polarization, and c) dry NafZrP with direct polarization and 1-s recycle delay. The spin diffusion mixing times were 1 s. MAS spinning frequency = 6250 Hz.

In the fresh NafZrP sample, we see four distinct environments based on the cross peaks: the $^{31}$P resonances at -6.7 ppm, -14.5 ppm of $(HO)_2P(OZr)_2$ and -21.3 ppm of anhydrous $\alpha$-ZrP; the $^{31}$P resonances at -17.6, -19.3, and -21.3 ppm of $\alpha$-ZrP; $^{31}$P resonances at -22.4 ppm of $(HO)P(OZr)_3$ in disordered ZrP; and $^{31}$P resonances at -28.2 ppm of $P(OZr)_4$. The former two environments are bridged with the $^{31}$P site resonating at -21.3 ppm. A minor fraction of $^{31}$P resonance at -20.4 ppm was also detected in the fresh ZrP sample.

In the dry NafZrP sample, the dominant $^{31}$P resonance at -22.4 ppm of $(HO)P(OZr)_3$ is in contact with $^{31}$P resonances at -14.5 ppm and -6.7 ppm of $(HO)_2P(OZr)_2$, while the $^{31}$P resonance at -28.2 ppm is still isolated. The local environments and tentative assignments of the $^{31}$P sites are listed in the Table 7.4.

**Table 7.4.** $^{31}$P chemical shifts and assignments of $^{31}$P sites in NafZrP composites

| $\delta$ ($^{31}$P) | fresh NafZrP | dry NafZrP | Assignments | Possible structure |
|---|---|---|---|---|
| -22.2 | 39.5% | 79% | $(HO)P(OZr)_3$ w/ fast H-exchange | Disordered ZrP; Transports protons. |
| -17.6 | 52.6% | ~ 0% | $(HO)P(OZr)_3$; $\alpha$-ZrP | $\alpha$-ZrP $\cdot$ $H_2O$ and anhydrous $\alpha$-ZrP |
| -19.3 | | | $(HO)P(OZr)_3$; $\alpha$-ZrP | |
| - 21.3 | | | $(HO)P(OZr)_3$; anhydrous $\alpha$-ZrP | |
| -6.7 | 0.7% | 1.1% | $(HO)_2P(OZr)_2$ w/ fast H-exchange | Less condensed P sites; Transports protons. |
| -14.5 | 5.3% | 6.6% | $(HO)_2P(OZr)_2$ w/ fast H-exchange | |
| -20.4 | < 1% | 11% | $(HO)P(OZr)_3$ w/ slow H-exchange | P sites in dry environments |
| -28.0 | 2.0% | 2.2% | $P(OZr)_4$ | Non-protonated P sites |

Our study has shown that the $\alpha$-ZrP species are not stable in NafZrP composites under dry conditions. 80% of stabilized $^{31}$P species in the dry NafZrP composite, which resonate at -22.4 ppm, have relatively fast proton-exchange dynamics. As supported by $^{19}$F NMR and $^{31}$P{$^{19}$F} REDOR in the to-be-submitted paper [21], these ZrP particles are located at the center of water channels and are surrounded by a water layer with a thickness of around 0.8 nm. The reduced $^{31}$P $T_1$ relaxation times of surface P-OH groups suggest that the protons have increase dynamics, which might explain the proton conductivity of the composite membrane at low hydration levels. [8, 9] (HO)$_2$P(OZr)$_2$ groups have more protons and apparently faster proton-exchange than (HO)P(OZr)$_3$ groups. Increasing the amount of (HO)$_2$P(OZr)$_2$ groups in NafZrP composites could be a possible way to improve the proton conductivity of NafZrP for fuel cell applications.

**Conclusions**

Zirconium phosphates synthesized in and outside Nafion have been characterized in detail by solid state NMR and XRD. Typical $\alpha$-ZrP with water of crystallization was obtained from the standard preparation procedure from ZrOCl$_2$ and H$_3$PO$_4$; but part of the structure transforms to anhydrous $\alpha$-ZrP, and some layers condense into pyrophosphates after drying at 150$^o$C as shown in the changes of the $^{31}$P chemical shifts and the XRD pattern. In the fresh Nafion-zirconium phosphate sample packed immediately after preparation, around 50% of ZrP has structural features similar to those of $\alpha$-ZrP as suggested by $^{31}$P NMR and $^1$H-$^{31}$P HetCor. The rest could be assigned to disordered ZrP with (HO)$_2$P(OZr)$_2$, (HO)P(OZr)$_3$ and P(OZr)$_4$ sites. In the NafZrP sample dried for a certain time after preparation, only disordered ZrP is present with a dominant $^{31}$P peak at -22.2 ppm that corresponds to (HO)P(OZr)$_3$. The reduced $^{31}$P $T_1$ relaxation times of surface POH sites in Nafion channels suggest that these

protons are involved in proton exchange with water, which might explain the proton conductivity of the NafZrP membrane at low hydration levels.

## References

(1)     Alberti, G. *Acc. Chem. Res.* **1978**, *11*, 163-170.

(2)     Clearfield, A. *Chem. Rev.* **1988**, *88*, 125-148.

(3)     Clearfie.A; Smith, S. D. *J. Colloid Interface Sci.* **1968**, *28*, 325-&.

(4)     Clearfield, A.; Stynes, J. A. *J. Inorg. Nucl. Chem.* **1964**, *26*, 117-129.

(5)     Alberti, G.; Casciola, M.; Marmottini, F.; Vivani, R. *J. Porous Mater.* **1999**, *6*, 299-305.

(6)     Jones, D. J.; Roziere, J. *Fuel Cells I* **2008**, *215*, 219-264.

(7)     Hogarth, W. H. J.; da Costa, J. C. D.; Lu, G. Q. *J. Power Sources* **2005**, *142*, 223-237.

(8)     Yang, C.; Srinivasan, S.; Bocarsly, A. B.; Tulyani, S.; Benziger, J. B. *J. Membr. Sci.* **2004**, *237*, 145-161.

(9)     Casciola, M.; Capitani, D.; Comite, A.; Donnadio, A.; Frittella, V.; Pica, M.; Sganappa, M.; Varzi, A. *Fuel Cells* **2008**, *8*, 217-224.

(10)    Alberti, G.; Casciola, M.; Capitani, D.; Donnadio, A.; Narducci, R.; Pica, M.; Sganappa, M. *Electrochim. Acta* **2007**, *52*, 8125-8132.

(11)    Nicotera, I.; Zhang, T.; Bocarsly, A.; Greenbaum, S. *J. Electrochem. Soc.* **2007**, *154*, B466-B473.

(12)    Ye, G.; Hayden, C. A.; Goward, G. R. *Macromolecules* **2007**, *40*, 1529-1537.

(13)    Rodgers, M. P.; Shi, Z.; Holdcroft, S. *Fuel Cells* **2009**, *9*, 534-546.

(14)     Chen, Q.; Hou, S. S.; Schmidt-Rohr, K. *Solid State Nucl. Magn. Reson.* **2004**, *26*, 11-15.

(15)     Bennett, A. E.; Rienstra, C. M.; Auger, M.; Lakshmi, K. V.; Griffin, R. G. *J. Chem. Phys.* **1995**, *103*, 6951-6958.

(16)     Bielecki, A.; Burum, D. P.; Rice, D. M.; Karasz, F. E. *Macromolecules* **1991**, *24*, 4820-4822.

(17)     Schmidt-Rohr, K.; Clauss, J.; Spiess, H. W. *Macromolecules* **1992**, *25*, 3273-3277.

(18)     vanRossum, B. J.; Forster, H.; deGroot, H. J. M. *J. Magn. Reson.* **1997**, *124*, 516-519.

(19)     Costantino, U.; Laginestra, A. *Thermochim. Acta* **1982**, *58*, 179-189.

(20)     Clayden, N. J. *J. Chem. Soc., Dalton Trans.* **1987**, 1877-1881.

(21)     Kong, X.; Schmidt-Rohr, K. *to be submitted to Chem. Mat.* **2010**.

# Chapter 8

# General Conclusions

The nanometer-scale structure of Nafion membrane and Nafion inorganic composites has been studied by solid-state NMR. We have demonstrated that solid-state NMR can serve as a powerful and indispensible tool for the structural elucidation of amorphous materials, and play an important role in the development of fuel cell materials.

The surface-to-volume (S/V) ratio of the polymer-water interface in Nafion obtained from SAXS was analyzed at different hydration levels. The experimental S/V ratio cannot be fitted to a single structure model since the structure of Nafion changes with hydration. In the normal hydration range of a fuel cell, only the newly developed water channel model is consistent with the S/V ratio; while models of dispersed water molecules and connected polymer ribbons account for the data at low and high hydration levels, respectively. The analysis of the S/V ratio provides a useful approach verifying the structural models of Nafion and possibly other ionomers.

The $^2$H quadrupolar splitting and $T_1$, $T_2$ relaxation times were measured for Nafion films hydrated with $D_2O$. It has been found that in drawn Nafion, in which the channels are straight and aligned to the draw direction, the exchange between bound and free $D_2O$ results in a residual quadrupolar splitting of 1-2 kHz and also an orientation-dependent $T_2$ relaxation time. The $T_1$ relaxation time, which is correlated to the hydration level, was used to extract the fraction of bound water. In normal Nafion with coiled channels, the $^2$H quadrupolar splitting of $D_2O$ is ~ 10-fold smaller than that in the corresponding drawn Nafion. This is explained by the motional averaging of the $^2$H coupling frequencies in the NMR timescale

when $D_2O$ diffuses through differently oriented segments of a water channel. The line narrowing and $T_2$ relaxation times were analyzed quantitatively by simulations of diffusion in coiled water channels with different persistence lengths. Based on the simulation, the persistence length of normal Nafion is estimated to be within 30 to 80 nm.

Solid-state NMR was used to characterize the chemical structure and composition of a novel Nafion phosphatranium composite synthesized by K. Wadhwa and J. G. Verkade, which is a potential candidate for anion exchange membrane. The composite membrane was prepared using Nafion-F and phosphatranium chloride under microwave condition. ^{19}F NMR and the [31]P-^{19}F distance measured by [31]P{[19]F} REDOR proved that the phosphatranium cations are attached to Nafion side-groups via a chemical bond through P or N. The two products have a molar ratio of 2:1, and they both have the potential to facilitate the transport of hydroxide ions. Degradation of the phosphatranium cations is not significant in the composite membrane as shown by ^{13}C NMR, which implies a good stability of the composite material.

We characterized the Nafion silica (NafSil) and Nafion zirconium phosphate (NafZrP) composites, which have better fuel cell performance at high temperatures and low hydration levels than normal Nafion. These composites were prepared through the sol-gel process and the ion exchange process, respectively, which grow the inorganic particle in the water channels of Nafion membrane. Under typical conditions with an inorganic volume fraction of around 15%, elongated silica and ZrP nanoparticles are formed at the center of water channels and surrounded by 0.8-nm thick water layers as evidenced by ^{19}F NMR and REDOR experiments. Based on the S/V ratio obtained by ^{29}Si NMR, the cylindrical silica particles in Nafion channels appear to have 2.8-nm-diameter cross section. Based on the

volume fraction of ZrP and $^{31}$P NMR, an elliptical-cylinder shape with two disordered ZrP layers was proposed for ZrP in Nafion.

Zirconium phosphates synthesized in and outside Nafion have been characterized in detail by solid state NMR and XRD. Typical α-ZrP with water of crystallization can be obtained from the standard preparation procedure from $ZrOCl_2$ and $H_3PO_4$; but part of the structure transforms to anhydrous α-ZrP, and some layers condense into pyrophosphates after drying at $150^o$C. In a fresh NafZrP sample packed immediately after preparation, around 50% of ZrP has structural features similar to those of α-ZrP as suggested by $^{31}$P NMR and $^1$H-$^{31}$P HetCor. The rest could be assigned to disordered ZrP with $(HO)_2P(OZr)_2$, $(HO)P(OZr)_3$ and $P(OZr)_4$ sites. In the NafZrP sample dried for a certain time after preparation, only disordered ZrP is present with a dominant $^{31}$P peak at -22.4 ppm that corresponds to $(HO)P(OZr)_3$.